5-31-2021

Electric field induced self-assembly of mesoscale structured materials and smart fluids

Suchandra Das
New Jersey Institute of Technology

ABSTRACT

ELECTRIC FIELD INDUCED SELF-ASSEMBLY OF MESOSCALE STRUCTURED MATERIALS AND SMART FLUIDS

by
Suchandra Das

This dissertation aims to study the forces that drive self-assembly in binary mixtures of particles suspended in liquids and on fluid-liquid interfaces when they are subjected to a uniform electric or magnetic field. Three fluid-particle systems are investigated experimentally and theoretically : (i) Suspensions of dielectric particles in dielectric liquids; (ii) Suspensions of ferromagnetic and diamagnetic particles in ferrofluids; and (iii) Dielectric particles on dielectric fluid-liquid interfaces. The results of these studies are then used to estimate the parameter values needed to assemble materials with desired mesoscale microstructures.

The first fluid-particle system studied is an electrorheological (ER) fluid formed using a mixture of positively and negatively polarizable particles. An important property of ER fluids is that their rheological properties can be modified on demand, within a few milliseconds, by applying an external electric field. Then, after the field is switched off, they go back to their original state. However, if only positively or negatively polarizable particles are used, the distribution of particles will fragment into chains and columns. Experimental results show that if a suitable mixture of positively and negatively polarized particles is used for making the ER fluid, the particle chains come closer, and the volume they occupy decreases. These results agree with the direct numerical simulations (DNS) based on the Maxwell Stress Tensor (MST) and point dipole methods. The application of the electric field results in the formation of a closely packed three-dimensionally connected structure. The influence of varying the electric field intensity, particle size, polarizabilities, and number ratio are characterized in terms of the extent of connected pattern formation which is

obtained numerically and the experimentally measured yield stress. The yield stress for an ER fluid formed using a particle mixture is larger than that for an ER fluid containing only one type of particles and is maximum for a critical volume fraction.

The second problem studied is the magnetorheological fluids (MR) formed using mixtures of micron-sized iron and glass particles in a liquid. The rheological behavior of MR and ER fluids is similar. For example, when an external magnetic field is applied to a MR fluid, the particles are magnetized and rearrange relative to one another, which modifies its rheological properties almost instantly. Also, when only one type of particles is used to prepare MR fluids, i.e., either positively or negatively magnetized particles, the particle distribution becomes fragmented into chains and columns. If a suitable mixture of positively and negatively magnetized particles is used, individual particle chains of one type attract the other type, creating a band with no gaps. This results in the formation of a closely packed connected structure. The MR fluids' yield stress behavior is experimentally investigated, formed by suspending mixtures of ferromagnetic and diamagnetic particles in ferrofluids (FF), which show that the yield stress is maximum when the volume fraction of ferromagnetic particles is around sixty percent. The rheological response of MR fluids depends on parameters such as the particles' concentration, magnetic susceptibilities of the suspending liquid, and the applied magnetic field intensity.

The third problem investigated is that of making UV-cured thin films with embedded monolayers of gold particles on their surfaces. This is achieved by self-assembly of gold nanoparticles on a UV curable liquid's surface by applying an electric field normal to the surface. The substrates are then used for Surface-Enhanced Raman Scattering (SERS) applications. The experimental results show that the substrates' performance depends on the particle concentration and the inter-particle distance. The laboratory-built substrates are found to be more efficient than the commercial SERS substrates.

ELECTRIC FIELD INDUCED SELF-ASSEMBLY OF MESOSCALE STRUCTURED MATERIALS AND SMART FLUIDS

by
Suchandra Das

A Dissertation
Submitted to the Faculty of
New Jersey Institute of Technology
in Partial Fulfillment of the Requirements for the Degree of
Doctor of Philosophy in Mechanical Engineering

Department of Mechanical and Industrial Engineering

May 2021

APPROVAL PAGE

ELECTRIC FIELD INDUCED SELF-ASSEMBLY OF MESOSCALE STRUCTURED MATERIALS AND SMART FLUIDS

Suchandra Das

Dr. Pushpendra Singh, Dissertation Advisor — Date
Professor of Mechanical and Industrial Engineering, NJIT

Dr. Ian S. Fischer, Dissertation Co-Advisor — Date
Professor of Mechanical and Industrial Engineering, NJIT

Dr. Zhiming Ji, Committee Member — Date
Professor of Mechanical and Industrial Engineering, NJIT

Dr. I. Joga Rao, Committee Member — Date
Professor and Chair of Mechanical and Industrial Engineering, NJIT

Dr. Dibakar Datta, Committee Member — Date
Assistant Professor of Mechanical and Industrial Engineering, NJIT

Dr. Denis L. Blackmore, Committee Member — Date
Professor of Mathematical Sciences, NJIT

BIOGRAPHICAL SKETCH

Author: Suchandra Das

Degree: Doctor of Philosophy

Date: May 2021

Undergraduate and Graduate Education:

- Doctor of Philosophy in Mechanical Engineering
  New Jersey Institute of Technology, Newark, NJ, 2021
- Bachelor of Technology in Production Engineering,
  Haldia Institute of Technology, Haldia, WB, India, 2013

Major: Mechanical Engineering

Presentations and Publications:

Das, S., Pillapakkam S., Musunuri N., Dalal B., Gurupatham S.K., Hossain M., Fischer I., and Singh P., 2021, "Directed Self-assembly of Suspensions into Cohesive Hierarchical Patterns," *Nature Communications* (Ready for Submission).

Das, S., Benouaguef I., Fischer I., and Singh P., 2021, "Suspension of Diamagnetic and Ferromagnetic Particles in Ferrofluid," (Manuscript under preparation).

Das, S., Musunuri N., Fischer I., and Singh P., 2021, "Thin Films with Self-Assembled Monolayers Embedded on their Surfaces for Surface Enhanced Raman Spectroscopy Applications," (Manuscript under preparation).

Das, S., 2020, "Directed Self-assembly of Dielectrically Polydisperse Nanoparticle Suspensions into Cohesive Hierarchical Patterns," *73rd Annual Meeting of the APS Division of Fluid Dynamics*, Chicago, IL, November 20-24.

Das, S., 2019, "Electric Field-induced Self-Assembly of Monolayers of Gold Nanoparticles for SERS Applications," *12th Northeast Complex Fluids and Soft Matter Workshop*, Bronx, NY, January 17.

Das, S., 2019, "Electric Field Driven Hierarchical Self-assembly of Electrorheological Suspensions," *ASME-JSME-KSME Joint Fluids Engineering Conference*, San Francisco, CA, July 28-August 1.

Das, S., 2019, "Experimental Studies of Electrorheological Fluids," *12th Northeast Complex Fluids and Soft Matter Workshop*, Newark, NJ, May 23-24.

Das, S., 2018, "Experimental Study of Electrorheological Fluids," *71st Annual Meeting of the APS Division of Fluid Dynamics*, Atlanta, GA, November 18-20.

Das, S., 2018, "Numerical and Experimental Study of Electrorheological Fluids," *ASME 2018 Fluids Engineering Division Summer Meeting*, Montreal, Canada, July 15-19.

Das, S., 2017, "Electric Field Induced Self-assembly of Monolayers of Gold Nanoparticles for Surface Enhanced Raman Scattering Applications," *70th Annual Meeting of the APS Division of Fluid Dynamics*, Denver, CO, November 19-21.

Dedicated to my family and friends.

ACKNOWLEDGMENT

I sincerely express my gratitude and appreciation to my Dissertation Advisor, Dr. Pushpendra Singh for his help and support. His encouragement and guidance at every step of my research studies at NJIT were conducive to the successful completion of my dissertation. I was able to leverage my understanding of fluid mechanics to start with, from his extensive width of expertise in this field. He instilled a sense of confidence in me to conduct my laboratory experiments, conferred faith in my abilities for taking independent decisions related to my research and inspired me to be diligent. Leading by example, he motivated me to embrace my strength, prevail in the most difficult situations and become the best in everything I did. He is a person who is understanding, amicable and at the same time bears a huge sense of ethical responsibility. For the first two years of my PhD program, he would stress the importance of coursework and allowed me to prioritize them. I remember, when I participated at scientific conferences, he would devote his valuable time in editing the presentations beforehand and ensured I practiced enough which improved my communication skills a great deal. As a result, I was comfortable in delivering my research presentation in front of a wider audiences at the actual conference. I sincerely thank him for his invaluable mentorship.

I want to thank my Co-Advisor, Dr. Ian S. Fischer for his guidance, expertise and for providing unique perspectives to solve the problems whenever I was stuck with my research work. His knowledge and technical depth allowed me to marshal my skills and improve by digging deeper within myself.

I would like to express my gratitude to each one of my committee members- Dr. I. Joga Rao, Dr. Zhiming Ji, Dr. Dibakar Datta and Dr. Denis Blackmore for their immense support throughout my PhD journey. I have thoroughly enjoyed taking courses by the Professors which made me confident, aware, and independent.

The Continuum Mechanics course by Dr. Rao was both challenging and exciting. The course was my first attempt of visualizing science right in front of my eyes which made the correlation between scientific equations and real-world applications easier. I am forever grateful to Dr. Ji for being a support system since even before I came to this country, for his generosity and for being the academic advisor who is willing to help his students in any way possible. His Modern Control course was instrumental in building up my core for further studies too. I want to thank Dr. Datta for encouraging me to complete my degree, for providing valuable suggestions and advice regarding my research and sharing job search strategies. I appreciate the time and effort Dr. Blackmore has spent in providing remarks about my dissertation and thank him for being compassionate.

I would like to take this opportunity to thank my research team colleagues- Islam Benouaguef, Dr. Naga Musunuri, Dr. Edison Amah, Dr. Shriram Pillapakkam for their support and coordination right from the beginning and their contribution in the research work of our team.

I am grateful to NJIT for accepting me as a doctoral student in the PhD program of Mechanical Engineering which opened numerous doors for my future endeavors. I acknowledge the Department of Mechanical Engineering for providing an opportunity to serve as a Teaching Assistant. This enriching experience allowed me to acquire skills outside of the classroom and learn practical operations of mechanical systems in detail. In addition, I would like to acknowledge the industrious graduate organizations on campus specially GSA for providing travel awards without which presenting my research work at technical conferences would not have been possible. The contribution of Ms. Clarisa Gonzalez from Graduate Studies Office on PhD club activities as advisor, conducting Thesis and Dissertation workshops and Dissertation reviews could not stressed enough and I want to thank her from the bottom of my heart. I want to extend my thanks to the organizations on-campus- PhD Club and Graduate Society

of Women Engineers with which I had the pleasure of associating myself with, for allowing me to get my voice heard as a woman engineer with great fortitude, find a foot on the ground, become self-sufficient and be a part of the broader campus community without hesitation.

I would like to gratefully acknowledge the financial support of National Science Foundation for my research work (Award # CBET-1067004 and CBET-1236035).

I owe the successful completion of my dissertation, which goes without saying, to my family- my parents and my older brother. I am blessed to have supportive parents who are willing to put forth my wishes ahead of their own - my darling mom, Mrs. Gouri Das, who has unflinching faith in me and my dad, Mr. Shyamal Kumar Das, who inspires me to be resilient. I am immensely thankful to them for raising me, for giving me good values, for their moral support and for all the sacrifices they made throughout the years. I cannot stress enough the positive influence my brother, Mr. Subhashis Das, continues to make on my life- he is my biggest critique; also, a person who has immense belief in my potential and motivates me to keep striving for success. He has always been my role model and I tried to master the art of excellence watching him excel in academics. He is the one person I turn to, in times of my hardships, only to know that a solution always exists. The idea and strength of transforming my vision into a reality was ingrained in me by him. I want to express my gratefulness for having an older brother to guide me at every step of my life and acknowledge his contribution in always keeping the motivation level up. He serves as a boundless source of inspiration to me to achieve anything and always assures there is light at the end of the tunnel. I am forever grateful to them for their unconditional love, for having confidence in my abilities and for always being there for me. I want to thank my sister-in-law, Mrs. Rima Das, for her being a wonderful person, for her support, and adding to the candid conversations. In addition, I would not let go of the opportunity to express my gratitude and thank

my darling grandmom, Mrs. Shyamali Mandal for being my hero, for believing in me right from the very beginning, all my relatives including my uncles, aunts, cousin sisters, brothers for being the lovely persons as they are and for contributing to my personal development.

Last but not the least, I would like to extend my thanks and express gratitude to my friends for bestowing their faith in me, understanding me, for being congruent with my thoughts, guiding me to make the right decisions, cheering me up in uncertain circumstances, help build up a can-do attitude and always sticking with me through thick and thin. I would like to make some special mentions- Nabina, Aditi, Sharmista, Antara, Dibyangana, Sneha, Avinash, Navya, Vidya, Asha, Santosh, Nidhi, Sam and Aayush. Thank you, God (the reasons are beyond the scope of this acknowledgement section)!

TABLE OF CONTENTS

TABLE OF CONTENTS
(Continued)

Chapter **Page**

LIST OF TABLES

LIST OF FIGURES

Figure **Page**

LIST OF FIGURES
(Continued)

Figure **Page**

LIST OF FIGURES
(Continued)

Figure **Page**

LIST OF FIGURES
(Continued)

Figure **Page**

LIST OF FIGURES
(Continued)

Figure **Page**

LIST OF FIGURES
(Continued)

Figure **Page**

LIST OF FIGURES
(Continued)

Figure **Page**

LIST OF FIGURES
(Continued)

Figure **Page**

LIST OF FIGURES
(Continued)

Figure **Page**

LIST OF FIGURES
(Continued)

Figure **Page**

LIST OF FIGURES
(Continued)

Figure **Page**

CHAPTER 1

INTRODUCTION

1.1 Introduction

This dissertation aims to model the inter-particle forces that drive the self-assembly in binary mixtures of micron to nano-sized particles in suspensions and on a fluid-liquid interface when they are subjected to an external electric or magnetic field. The force models would improve our ability to design the desired microstructural arrangement and thus help in developing efficient bottom-up approaches to manufacture macroscale structures from mesoscale particles. Three problems were investigated to model the interaction amongst particles and manipulate particles' self-assembly process using electric and magnetic fields.

When an external electric or magnetic field is applied to a mixture of positively and negatively polarizable or magnetizable particles in our laboratory-built fluid-particle suspensions, a closely packed structure was formed due to which the rheological behavior was modified e.g., the viscosity was increased. Therefore, the yield stress increased. The increase in the yield stress occurs due to the formation of a well-connected structure without gaps in between particle chains and is higher compared to the traditional fluid-particle suspensions studied in literature. The behavior of the prepared suspensions and a comparison with the already existing suspensions are discussed under sub-sections 1.1.1-1.1.2.

When an external electric field was applied in a normal direction to a fluid-liquid interface, gold nanoparticles trapped at the interface self-assembled to form monolayers. The electric field-induced particle monolayers do not have shortcomings in comparison to the capillary-induced particle monolayers; there are no voids, there is long-range order, hierarchical arrangement is possible and the

interparticle spacing can be adjusted by varying the electric field intensity. In our experiments, 600 nm gold particles were used for forming monolayers to obtain different particle arrangements on thin films. The films embedded with gold particle monolayers were used to prepare substrates for Surface Enhanced Ramana Scattering (SERS) applications. The experimental results show that the performance of our laboratory-built substrates containing varying concentrations of gold nanoparticles was better, indicating a stronger SERS effect than a commercial SERS substrate and the substrates studied in the past. Our substrates are 6.75 times more efficient per gold particle compared to the commercial substrates. It is also found that 46% of the substrates' surface area was covered with gold particles which is another reason for the observed enhancement.This is discussed in detail under sub-section 1.1.3.

1.1.1 Electrorheological Fluids

The first problem investigated is to form an improved electrorheological fluid using a mixture of positively and negatively polarizable particles. ER fluids have various applications because their rheological properties can be modified almost instantaneously (within a few milliseconds) by applying an electric field. The magnitude of the change in properties depends on the electric field's intensity, and the properties go back to their original values when the field is switched off; hence they are called smart fluids. This tunable and quick rheological response on demand makes them highly desirable in various industrial applications, e.g., valves, clutches, and damping devices. When an electric field is applied, particles become polarized and aligned along the electric field direction due to dipole-dipole interaction. This results in the formation of chain-like structures that increase the ER suspension's viscosity. This behavior is shown in Figure 1.1.

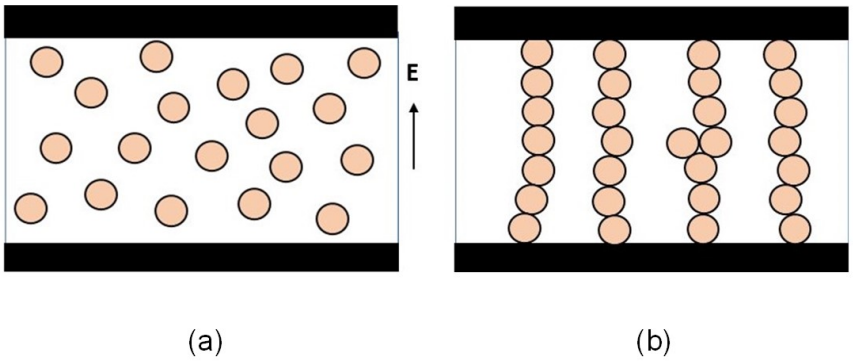

Figure 1.1 ER fluid suspension containing a mixture of dielectric particles (beige spherical spheres) suspended in a dielectric liquid in a device with top (positive) and bottom (negative) electrodes when an electric field is applied in a vertical direction. (a) Initial random distribution of particles before the electric field was applied (b) Particles aligned and form chain-like structures upon application of an electric field.

The above approach can also be employed to self-assemble materials with mesoscale patterns from a suspension of microparticles (nano- to micron-sized particles). The existing bottom-up manufacturing capabilities are limited because of the absence of inter-particle forces between electrically neutral and nonmagnetic particles that can cause them to self-assemble. At atomic and molecular scales, self-assembly is driven by electrostatic charges, which occur spontaneously. However, the importance of Coulomb forces decreases with increasing particle size—and so an alternate mechanism is needed to make microparticles self-assemble. Advances in particle syntheses, microscopy, and parallel computing have allowed us to explore alternate interaction mechanisms among microparticles, which can be exploited to guide their self-assembly into macroscopic structures.

In recent years, several mechanisms that give rise to inter-particle forces which drive the self-assembly process have been considered, such as capillarity, anisotropy in shape [1, 2, 3], steric [4] and entropic effects [5], and dipolar and magnetic interactions [6, 7, 8, 9, 10, 11, 12, 13, 14, 15, 16, 17, 18, 19, 20, 21, 22, 23, 24, 25, 26]. This area of research has attracted enormous interest because the ability to manipulate the force between micron and nano-sized particles can be exploited to achieve our goal of

the bottom-up fabrication of materials with organized structures and patterns using larger microparticles [7, 10, 12]. It would also be helpful in other applications such as for creating smart materials whose properties can be tuned, on-demand, by an external stimulus [17, 19].

Inter-particle forces that arise due to the application of an external electric field [12] have also been considered for self-assembly. In fact, they are routinely used in electrorheology [6, 8, 9, 11, 13, 15], where the goal is not self-assembly but rather to obtain changes in rheological properties (suspension viscosity) by modifying microstructure. Specifically, in response to the applied electric field, the particles of electrorheological (ER) suspensions polarize, and their dipole moments align with the field direction, which causes the particles to form chains and columns to resist shear.

The problem in applying the electric field technique to direct self-assembly in ER fluid mixtures containing only one type of particles is that the dipole-dipole force is attractive only when the line joining the particle centers is aligned predominantly along the field direction. When the line joining the particle centers is perpendicular to the applied field's direction, the force is repulsive, which causes the particle distribution to fragment into chains and columns [12], as shown in Figures 1.2 and 1.3. This chain/column formation was first reported by Winslow [20]. A recurring observation in many subsequent studies has been that particles do not pack closely in planes normal to the field. Specifically, although particles organize in chains and columns, there are particle-free regions in between them. This technique, therefore, does not meet the key requirement of a bottom-up fabrication technique as it cannot bring the particles together in both the field direction and the perpendicular plane.

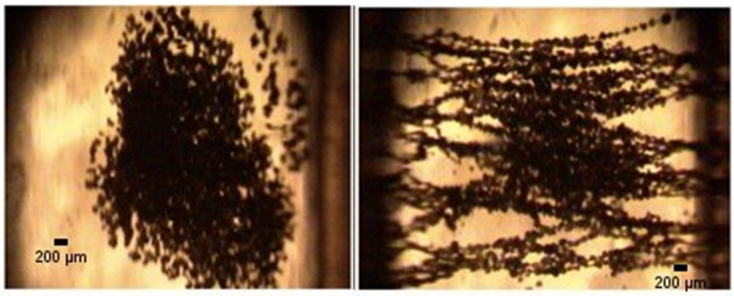

Figure 1.2 Fragmentation in ER Fluid; (a) Top view of the arbitrary initial configuration of an ER fluid (b) The application of an electric field caused the particles to form chains and columns. The chains and columns moved away from each other creating particle-free regions.

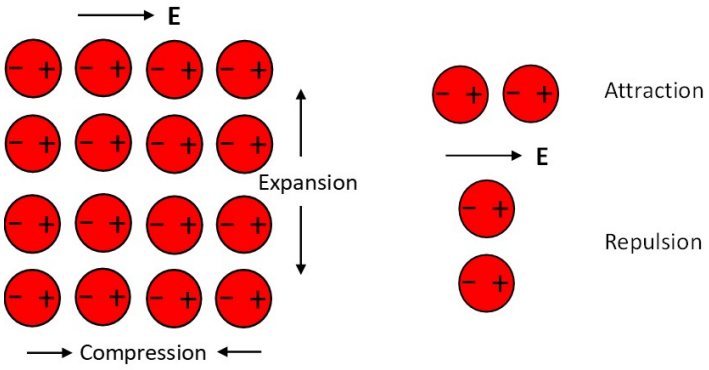

Figure 1.3 Fragmentation in a periodic ER Fluid. (a) The dipoles for positively polarized particles are created in the direction of the electric field when the applied field is horizontal (b) Attraction and repulsion between particles in the parallel and perpendicular direction to the field, respectively.

Our goal is to form an electrorheological fluid consisting of both positively and negatively polarized particles so that they self-assemble to create a fully connected structure without the occurrence of particle chain fragmentation when an electric field is applied. The adopted approach is discussed in detail in Chapter 1.

1.1.2 Magnetorheological Fluids

The second problem studied in this dissertation is that of forming a magnetorheological fluid (MR) that contains a mixture of positively magnetized micron-sized iron particles and negatively magnetized glass particles in a ferrofluid. MR Fluids have diverse applications in the engineering field and in medical, biological, and technological domains due to their properties of retention in a magnetic field, heat transfer, capability of reducing friction, and modified physical properties when a magnetic field is applied. The applications have resulted in the development of state-of-the-art mechanical devices and opened new research areas. Technological applications include sealing [27], heat dissipation, and damping [28]. Biomedical areas can benefit from MR fluid properties in magnetic drug targeting consisting of carrying medications to exact locations within the body [29], magnetic separation of cells, and as a contrasting agent for Magnetic Resonance Imaging [30]. When a magnetic field is applied to an MR fluid, suspending particles acquire a magnetic moment and align along the magnetic field direction. This causes the particles to rearrange relative to one another, resulting in the formation of chain- and column-like structures, which modify their rheological properties. Particle chain formation in a magnetic field occurs due to magnetic dipole-dipole interaction.

Recent studies show that bidisperse MR fluids present an enhanced viscosity with increasing particle concentration, and particles show repulsion at closer distances [31, 32, 33]. Diamagnetic (DM) particles suspended in a ferrofluid, which are used for forming Inverse Magnetorheological Fluid, shows clusters of ferromagnetic

(FM) particles around a single particle chain of DM particles and shows particles' fragmentation into chains and columns. The fact that these field-induced columns do not combine to form a connected cluster, including when a surface pattern is used to guide their assembly [23], indicates that the forces among them are not attractive.

Again, as for an electric field, the problem in using a magnetic field to direct self-assembly in the MR fluid mixtures containing only one type of particles is that the magnetic dipole-dipole interaction force is attractive only when the line joining the particle centers is aligned predominantly along the field direction. When the line joining the particle centers is perpendicular to the applied field's direction, the force is repulsive, which causes the particle distribution to fragment into chains and columns, as shown in Figure 1.4.

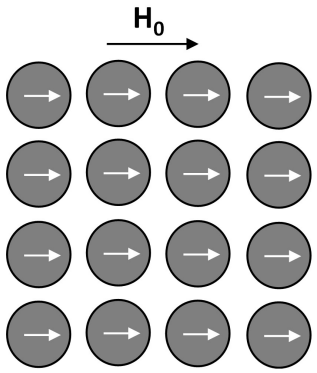

Figure 1.4 A sketch showing the behavior of an MR suspension consisting of ferromagnetic particles in a periodic arrangement under the application of a magnetic field. Ferromagnetic particles (dark gray spheres) acquire magnetic moments which are aligned with the magnetic field. Particles attract each other when they aligned parallel to the field direction and repel, when aligned in perpendicular direction.

Our aim is to investigate the microstructural and the yield stress changes in MR fluids formed by suspending mixtures of ferromagnetic and diamagnetic particles in a ferrofluid with varying particle concentrations so that the distribution does not get fragmented into chains and columns. The adopted approach is discussed in detail in Chapter 2.

1.1.3 Particle Embedded Films

The third problem investigated in this dissertation is that of making UV-cured thin films with embedded monolayers of gold particles on their surfaces. This is achieved by self-assembly of gold nanoparticles on a UV curable liquid's surface by applying an electric field normal to the surface. The substrates are then used for Surface-Enhanced Raman (SERS) applications.

The phenomenon of self-assembly of particles at fluid-liquid interfaces can be understood by the simple example of clustering of breakfast cereal flakes on the surface of milk. When particles are sprinkled on a liquid surface, lateral capillary forces arise, causing the particles to cluster together. In recent years, clustering of particles in fluid-liquid interfaces has drawn much attention because the particles' self-assembly process can be utilized to form microstructures. This fabrication method of forming microstructural monolayers possesses the capability to form clusters of hierarchical patterns which have a range of applications, e.g., pollination in hydrophilous plants [34], clustering of insect eggs [35, 36], dispersion of proteins [37], and separation of ink and toner particles [38]. In addition, applications of thin films with embedded patterns of particles using self-assembly techniques [39] are widespread in industry, e.g., they are utilized for making photomasks, porous membranes with precise pore size which can be used for drug delivery, and substrates for SERS. SERS applications include cell and tissue-based analysis in life sciences, quality control and counterfeit detection in the pharmaceutical industry, security (detection of explosives), forensics, food safety, and biomolecular identification [40].

However, capillary-induced monolayers formed this way have defects, lack long-range order, their lattice spacing is not adjustable, and the formation of hierarchical structures is not possible, as shown in Figure 1.5. Moreover, lateral capillary forces are too small to move small micron and nano-sized particles to form self-assembled patterns.

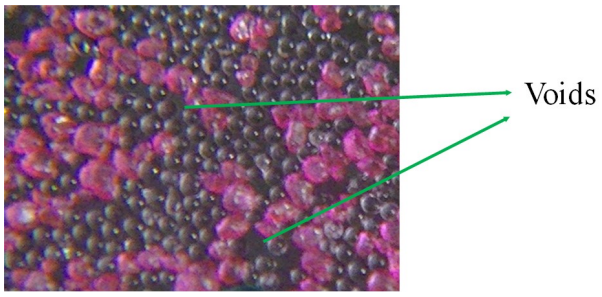

Figure 1.5 Top view of a monolayer of a mixture of plastic and glass beads clustered on a liquid surface. Monolayers by capillary assembled by capillary forces show voids, the lattice lacks order, and the lattice spacing cannot be adjusted.

We present a technique of formation of monolayers that overcomes the aforementioned shortcomings. In our technique, an electric field is applied normal to the interface that drives the self-assembly process of particles to form monolayers. The monolayers formed using this technique have improved properties such as adjustable lattice spacing, defect-free, and long-range order. They are then embedded on thin films which are used as substrates for Surface-Enhanced Raman Scattering (SERS) technique.

A similar procedure was followed for forming thin films with embedded electric field-induced self-assembled monolayers of gold nanoparticles. Figure 1.6 shows the thin films embedded with particles having different arrangements with adjustable lattice spacing. Our method produces uniform surface patterns of metallic particles, which is rapid and cost-effective. The experimental results show that the substrates' performance depends on the particle concentration and the inter-particle distance. We found that the laboratory-built substrates to be more efficient than the commercial SERS substrates.

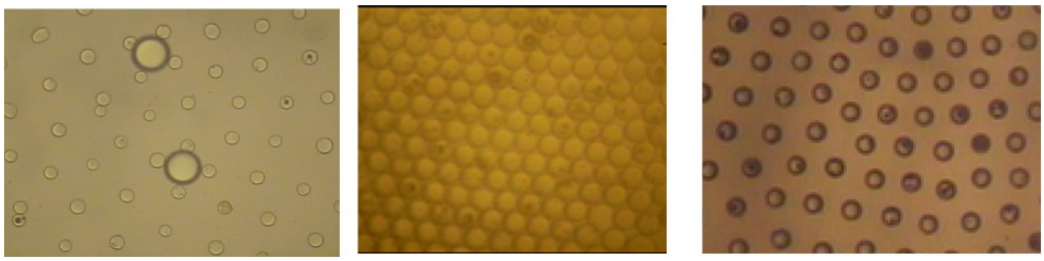

Figure 1.6 Thin films embedded with micron- and nano-sized particles. Monolayers formed by self-assembly under the application of electric field enable us to get different types of particle arrangements with adjustable lattice spacing.

1.2 Background: Self-Assembly and Governing Equations

1.2.1 Electric Field-Induced Forces

In an electric field, dielectric particles suspended in a dielectric liquid interact with each other by dipole-dipole forces to form clusters of patterns. The dipole-dipole interaction can be understood by point-dipole (PD) approximation of the forces acting on particles when a uniform electric field is applied (Figure 1.7). According to this approximation, the interaction force on a spherical particle i due to another particle j is given by the following equation [13, 41]:

$$F_D(r,\theta) = 12\pi\varepsilon_0\varepsilon_c\beta_i\beta_j E_0^2\frac{(a_i a_j)^3}{r^4}((3\cos^2\theta - 1)e_r + \sin 2\theta e_\theta) \tag{1.1}$$

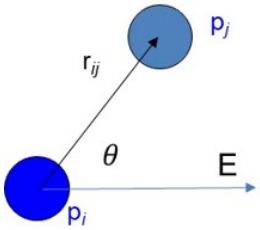

Figure 1.7 Point-dipole (PD) approximation. The angle θ between the electric field direction and e_r for two particles i and j under the application of an electric field.

Here, $e_r = \frac{r_j - r_i}{|r_j - r_i|}$ is the unit vector along the line joining the centers of the spheres, e_θ is a unit vector normal to e_r in the plane containing the electric field

direction, and θ is the angle between the electric field direction and e_r. Here $r = |r_j - r_i|$ is the distance between the particles, E_0 is the electric field intensity, $\varepsilon_0 = 8.8542 \times 10^{-12}$ F/m is the permittivity of free space, a_i and a_j are the radii of the two particles and $\beta_i(\omega) = Re(\frac{\varepsilon_\pi^* - \varepsilon_c^*}{\varepsilon_\pi^* + 2\varepsilon_c^*})$ is the Clausius-Mossotti (CM) factor of the i^{th} particle. Here ε_{pi}^* and ε_c^* are the frequency-dependent complex permittivities of the i^{th} particle and the suspending liquid, respectively. The complex permittivity is $\varepsilon^* = \varepsilon - \frac{j\sigma}{\omega}$, where ε is the permittivity, σ is the conductivity, ω is the frequency of the applied ac field and $j = \sqrt{-1}$. Chain formation in the presence of an electric field can be understood by Figure 1.8. Particles attract each other when they are aligned parallel to the electric field direction, as shown in Figure 1.8(a). However, they repel when aligned perpendicular to the electric field direction, as shown in Figure 1.8(b).

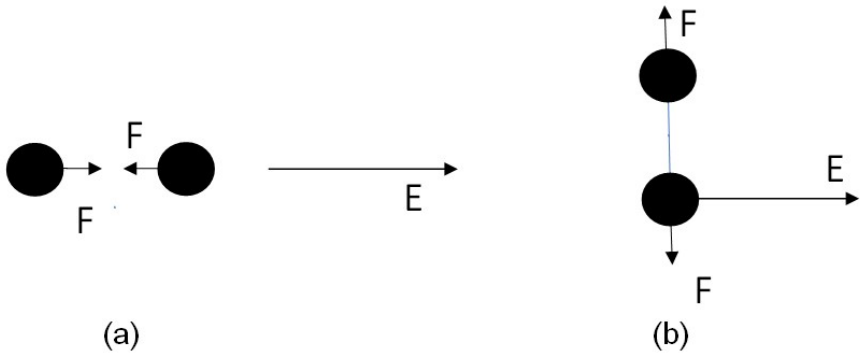

Figure 1.8 Dipole-dipole interaction between two particles. (a) Particles attract when $\theta = 0°$. (b) Particles repel when $\theta = 90°$.

The point-dipole approximation accuracy decreases when the distance between particles is small since the model assumes the particle distance to be much larger than their radii. The direct numerical simulations method based on the Maxwell stress tensor (MST) approach is adopted to improve accuracy. As per the MST model, the Maxwell stress tensor is obtained by Equation (1.2). The electric force acting on a particle is then obtained by integrating MST on the particle surface as given by Equation (1.3).

$$\boldsymbol{\sigma}_M = \epsilon \mathbf{E}\mathbf{E} - \frac{1}{2}\epsilon(\mathbf{E}.\mathbf{E})\mathbf{I} \tag{1.2}$$

$$\mathbf{F}_E = \int_{\partial \mathbf{P}_i} \boldsymbol{\sigma}_M.\mathbf{n}\, ds \tag{1.3}$$

1.2.2 Magnetic Field-Induced Forces

When particles with magnetic properties are suspended in a suitable carrier liquid, they interact to form clusters because of magnetic dipole-dipole forces which occur when a magnetic field is applied. In an MR fluid containing a mixture of diamagnetic and ferromagnetic particles, alternating bands of chains of both types of particles are formed [11]. In the point dipole limit, the magnetic moment acquired by a particle of relative permeability μ_P in an external magnetic field $\mathbf{H_0}$ is given by:

$$\mathbf{m} = 3\mu_f \beta_p V \mathbf{H_0} \tag{1.4}$$

where V is the particle volume, μ_f represents the relative magnetic permeability of the carrier medium and $\beta_P = \frac{\mu_P - \mu_f}{\mu_P + 2\mu_f}$ represents the Clausius-Mossotti factor or the magnetic contrast factor42. For diamagnetic particles, $\mu_P = 1$, which makes their $\beta < 0$. However, $\beta \to 1$ for ferromagnetic particles as $\mu_P >> 1$. $\mu_f > 1$ for ferrofluids and can be varied by varying the fluid concentration. Therefore, the diamagnetic particles have their magnetic moments opposite to the direction of the magnetic field, and the ferromagnetic particles acquire magnetic moments in the direction of the field. The dipole-dipole interaction force acting on a particle i due to another particle j is given by [42]:

$$\mathbf{F}_{ij} = \frac{\mu_0}{4\pi\mu_f}\left\{3\frac{\mathbf{m}_i\mathbf{m}_j}{r^5}\mathbf{r} + \frac{3}{r^5}[(\mathbf{m}_i.\mathbf{r})\mathbf{m}_j + (\mathbf{m}_j.\mathbf{r})\mathbf{m}_i] - \frac{15}{r^7}(\mathbf{m}_i.\mathbf{r})(\mathbf{m}_j.\mathbf{r})\mathbf{r}\right\} \tag{1.5}$$

Here, $\mathbf{m}_i$ and $\mathbf{m}_j$ are the magnetic moments of particles i and j, respectively, μ_0 is the magnetic permeability of vacuum, and $\mathbf{r}$ is a vector connecting the center of two adjacent particles. When the line joining the particle centers is parallel to the magnetic field direction, the interaction force is attractive and becomes repulsive when it is perpendicular to the field as shown in Figure 1.9.

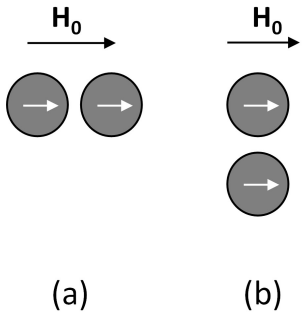

Figure 1.9 MR fluid behavior consisting of ferromagnetic particles under the application of a magnetic field. (a). The net force between two particles is attractive when the line joining the particle centers is parallel to the applied magnetic field. (b) The net force is repulsive when the line joining the particle centers is perpendicular to the field direction.

1.2.3 Particles at Fluid-Liquid Interfaces

This section describes the self-assembly process of particles at fluid-liquid interfaces. A particle can float on a fluid-liquid interface because the deformation of the interface (shown in Figure 1.10) gives rise to a capillary force in the direction normal to the interface such that it can balance the particle's buoyant weight. However, for small particles with a size less than ∼10 microns, only a small deformation of the interface is sufficient for the capillary force's vertical component to balance the particle's buoyant weight [43]. This results in a very small lateral capillary force which is not large enough to move the particles.

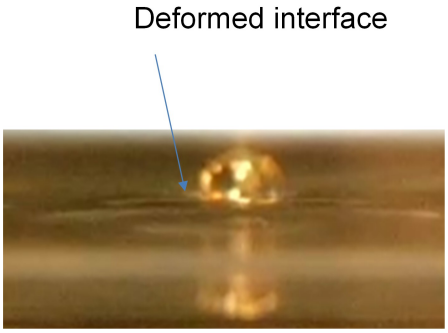

Figure 1.10 Deformed interface.

The deformation of the interface gives rise to lateral capillary forces as well, which causes two neighboring floating particles to form clusters. When two hydrophobic spheres are close to each other, the deformed interface around the spheres is not symmetric because the interface height between the spheres is lowered by the capillary force, as shown in Figure 1.11. The lateral component of the interfacial tension is attractive, which makes the spheres cluster. The same is true for two hydrophilic spheres [44].

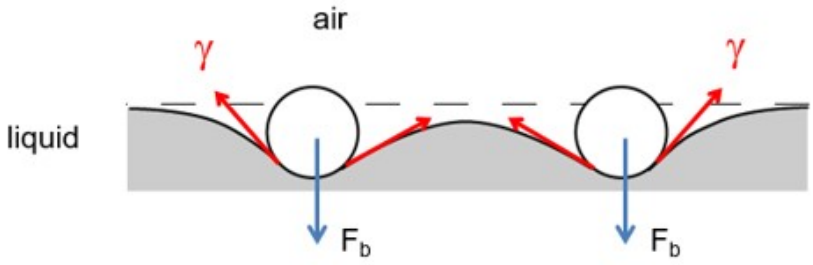

Figure 1.11 Two particles floating on a liquid surface attract each other because of lateral capillary forces.

The contact angle at the line of contact of three phases- solid, liquid, and gas plays a crucial role in determining the vertical force component because of which a heavier particle is able to float, as shown in Figure 1.12. The contact angle is given by Young-Dupré equation:

$$\gamma \cos \alpha = \gamma_{PG} - \gamma_{PL} \tag{1.6}$$

Here, γ is the surface tension of the liquid, α is the contact angle, and γ_{PG} and γ_{PL} are the interfacial energies between solid and gas, and solid and liquid, respectively.

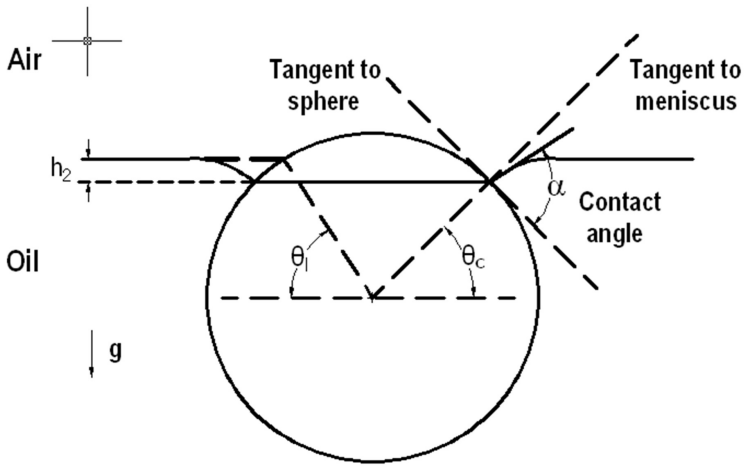

Figure 1.12 Schematic of a heavier than liquid hydrophilic (wetting) sphere of radius a hanging on the contact line at θ_c. The point of extension of the flat meniscus on the sphere determines the angle θ_1, and h_2 is defined as $h_2 = R(\cos\theta_c - \cos\theta_1)$. The angle α is fixed by the Young Dupré law and θ_c by the force balance.

The vertical component of the capillary force is given by:

$$F_c = -2\pi R\gamma \sin\theta_c \sin(\theta_c + \alpha) \tag{1.7}$$

Here, R is the particle radius, γ is the surface tension coefficient, θ_c is the filling angle, and α is the contact angle. F_c depends on all these parameters. The above equation is true for hydrophobic and hydrophilic cases, i.e., for all contact angle values. The buoyant weight of a particle is given by:

$$F_b = -g\rho_L R^3 f_b(\frac{\rho_a}{\rho_L}, \frac{\rho_p}{\rho_L}, \theta_c, \frac{h_2}{R}) \tag{1.8}$$

Here, g is the acceleration due to gravity, ρ_P is the particle density, ρ_a is the density of the upper fluid, ρ_L is the density of the lower fluid, and f_b is a dimensionless function of $\frac{\rho_a}{\rho_L}, \frac{\rho_p}{\rho_L}, \theta_c$ and $\frac{h_2}{a}$. For a small particle having radius R, the buoyant weight becomes negligible as it scales as R^3. This means a small interfacial deformation is required for the vertical capillary force, which scales as R, to balance the buoyant weight.

In our technique, the application of an electric field normal to the fluid-liquid interface gives rise to lateral dipole-dipole forces, which can be attractive or repulsive depending on the particle polarizabilities. These forces can be adjusted by selecting suitable liquids. When two particles are of the same type having the same sense of polarizabilities, i.e., both positive or negative, they repel. However, particles attract each other when they are of different types and have the opposite polarizabilities, i.e., one positive and one negative. The clustering of particles can be manipulated by varying the electric field intensity. The electric field gives rise to a vertical electric force that enhances the buoyant weight, and therefore, the lateral capillary force between the particles is greater. Consequently, particles come together to form clusters.

Lateral forces on particles. When an electric field is applied normal to a fluid-liquid interface, the total lateral force F_l between two particles, i and j adsorbed at the interface, is given by:

$$F_l = -\frac{w_i w_j}{2\pi\gamma}\frac{1}{r} + \frac{3p_i p_j}{4\pi\varepsilon_0\varepsilon_L}\frac{1}{r^4} \tag{1.9}$$

Here, w_i is the vertical force acting on the i^{th} particle, p_j is the induced dipole moment of j^{th} particle, ε_0 is the permittivity of free space, ε_L is the permittivity of the lower liquid, g is the interfacial tension, r is the distance between the particles.

The induced moments of the particles, p_i and p_j can be adjusted by selecting suitable fluids. The first term in Equation (1.9) shows the lateral capillary force which arises as a result of the total vertical force acting on the particles, which includes vertical electric forces and particles' buoyant weight. The second term is the attractive or repulsive dipole-dipole force between particles which can be understood from Figure 1.13. Both of these terms depend on the electric field intensity.

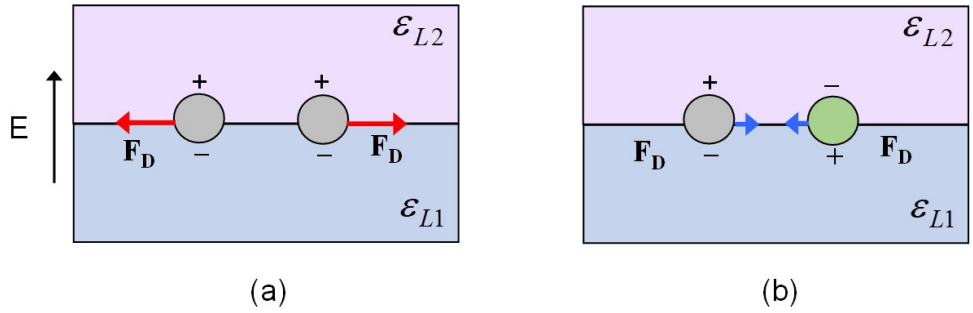

Figure 1.13 Dipole-dipole forces acting between two particles. (a) The force is repulsive when particles are of the same type having the same polarizabilities. (b) The force is attractive when particles have opposite polarizabilities.

Vertical forces on a particle. When an electric field is applied normal to a fluid-liquid interface, the particle's vertical position in equilibrium is determined by the condition of the sum of the forces acting on the particle being zero such that the buoyant force balances the capillary force, i.e., $F_c + F_b = 0$

1.3 Dissertation Organization

Chapter 2 discusses the self-assembly process of suspensions of dielectric particles in dielectric liquids. We showed that the problem of fragmentation of particles into chains and columns can be overcome by using a mixture of positively and negatively polarized particles, when an electric field was applied.

In Chapter 3, inter-particle forces that drive self-assembly in suspensions of ferromagnetic and diamagnetic particles in ferrofluids were studied. The mechanism that determines particles' distribution upon application of a magnetic field is analogous to the fluid-particle system as discussed in Chapter 2.

Chapter 4 investigates the behavior of dielectric particles on dielectric fluid-liquid interfaces. The problem consists of making UV-cured thin films with embedded monolayers of self-assembled gold particles on their surfaces. The substrates were then used for Surface-Enhanced Raman (SERS) applications.

Chapter 5 presents the dissertation summary and conclusion.

CHAPTER 2

DIRECTED SELF-ASSEMBLY OF SUSPENSIONS INTO COHESIVE HIERARCHICAL PATTERNS

The ability to create new macroscopic structures by assembling microscopic particles remains mostly undeveloped in part because of the inability of the currently available techniques to make assemblies of uncharged nonmagnetic microscopic particles of two or more different types. It is demonstrated that this shortcoming can be overcome if the application of an external electric field causes the particles of one kind to become positively polarized and of the second kind negatively. Experimental and direct numerical simulation results show that the resulting dipolar forces amongst the particles can cause them to rearrange to form hierarchical cohesive patterns spontaneously in which they attract their nearest neighbors. The polarization requirements can be met by suspending particles in a suitable liquid medium and selecting an appropriate electric field frequency as the complex permittivities of different types of particles are different. Furthermore, it is possible to tailor the assembled hierarchical macrostructure to create materials with new microscopic patterns by varying parameter values. This inter-particle forces driven assembly, which is analogous to the process by which complex macromolecules assemble from atoms, advances our state-of-the-art of bottom-up manufacturing utilizing microscopic particles.

2.1 Introduction

The existing bottom-up manufacturing capabilities employing nano to micron-sized particles (microparticles) are limited because of the absence of inter-particle forces between electrically neutral and nonmagnetic particles that can cause them to self-assemble. At atomic and molecular scales, self-assembly is driven by electrostatic charges, which occurs spontaneously. However, the importance of coulomb forces

decreases with increasing particle size—and so an alternate mechanism is needed to make microparticles self-assemble. Advances in particle syntheses, microscopy, and parallel computing have allowed us to explore alternate interaction mechanisms among microparticles, which can be exploited to guide their self-assembly into macroscopic structures.

In recent years, several mechanisms that give rise to inter-particle forces have been considered, such as capillarity, anisotropy in shape [45, 46, 47], steric [48] and entropic effects [49], and dipolar and magnetic interactions [50, 51, 52, 53, 54, 55, 56, 57, 58, 59, 60, 61, 62, 23, 63, 64, 65, 66]. This area of research has attracted enormous interest because the ability to manipulate the force between micron and nano-sized particles can be exploited to achieve our goal of the bottom-up fabrication of materials with organized structures and patterns using larger microparticles [67, 68, 69, 70]. It would also be helpful in other applications such as for creating smart materials whose properties can be tuned, on-demand, by an external stimulus [58, 59].

Inter-particle forces that arise due to the application of an external electric [50] or magnetic field [51] have also been considered for self-assembly. In fact, they are routinely used in electro- and magneto-rheology, where the goal is not self-assembly but rather to obtain changes in rheological properties (suspension viscosity) by modifying microstructure [52, 53, 54, 55, 56, 57]. Specifically, in response to the applied electric field, the particles of electrorheological (ER) suspensions polarize and their dipole moments align with the field direction which causes the particles to form chains and columns to resist shear.

The problem in applying this technique to direct self-assembly is that the dipole-dipole force is attractive only when the line joining the particle centers is aligned predominantly along the field direction (see Supplementary Information for a detailed discussion). When the line joining the particle centers is perpendicular to the applied field's direction, the force is repulsive, which causes the particle distribution

to fragment into chains and columns [50]. This chain/column formation was first reported by Winslow [60] (see Figure 2.1a, b). A recurring observation in many subsequent studies has been that particles do not pack closely in planes normal to the field. Specifically, although particles organize in chains and columns, there are particle-free regions in between them. This technique, therefore, does not meet the key requirement of a bottom-up fabrication technique as it cannot bring the particles together in both the field direction and the perpendicular plane.

Recent studies show that mixtures containing positively and negatively polarized particles on a two-dimensional surface self-assemble into the ring, flower-like, and other periodic arrangements [67, 68, 71]. They form fragmented chain/column-like patterns in three dimensions, with each column consisting of both types of particles [61, 23, 64, 72]. Similarly, particles of magnetorheological fluids formed by suspending diamagnetic (DM) and ferromagnetic (FM) particles in a ferrofluid fragment into chains and columns [51]. The fact that these field-induced columns do not combine to form a connected cluster, including when a surface pattern is used to guide their assembly [23], indicates that the forces among them are not attractive. However, studies also show that there is yield stress enhancement for certain mixtures of positively and negatively polarized/magnetized particles, which suggests that there is increased attraction among the fragmented chains and columns [61, 63, 64, 72].

In this problem, experimental and direct numerical simulation results demonstrate that there is a range of parameter values for which mixtures containing positively and negatively polarized particles self-assemble to form connected hierarchical clusters. The force between a particle and its nearest neighbor is attractive both along and normal to the direction of the applied electric field, and that the cluster's microstructure can modified be varying parameter values. The technique thus can be used to form a range of three-dimensionally connected assemblies of microparticles.

As discussed in Supplementary Information, it is possible to induce positive polarization in one type of particles and negative polarization in the second type by selecting a suitable liquid medium since the complex permittivities of different types of particles are different. We can also vary the frequency of the applied electric field to change their polarizibilities relative to one another [62, 73].

2.2 Particle Level Interaction Mechanisms

To understand the mechanism that causes the particle distribution to fragment, let us consider the dipole-dipole forces in the periodic arrangement of monodisperse particles shown in Figure 2.1c. We choose the periodic arrangement since it helps visualize why the dipole-dipole forces cannot cause particles to pack together tightly in all three directions. Notice that the dipole-dipole forces are attractive in the electric field's direction, but repulsive in the plane perpendicular to the field. Consequently, the particles come together and align in the electric field's direction but move apart in the perpendicular plane. If the particles' initial arrangement is not periodic, the particle pairs are also subjected to electric torques. These basic mechanisms thus cause particles to arrange into chains and columns [51, 55, 66, 74, 75]. Our direct numerical simulations (Figure 2.1d-f) show that, as in experiments (Figure 2.1a-b), the dipole-dipole forces cause particles to fragment into chains and columns that are aligned parallel to the electric field direction. The forces among the columns are repulsive, which cause them to move apart, as is the case for experiments.

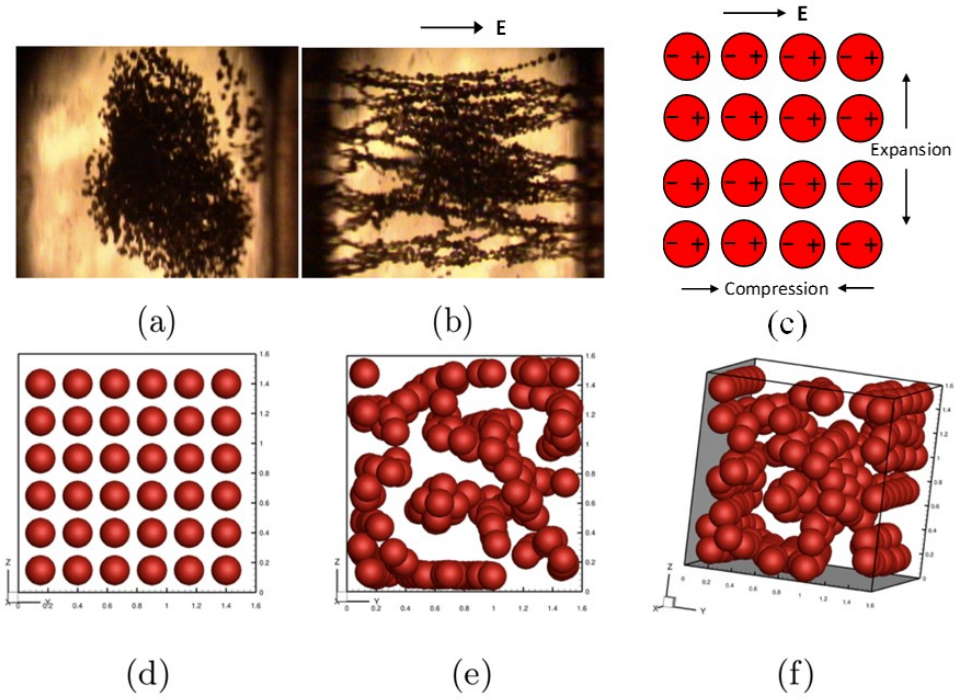

Figure 2.1 Electric field-induced rearrangement of positively polarizable particles. (a) Top view of the arbitrary initial configuration of a suspension of aluminum oxide (average size 102.5 μm, dielectric constant 9.8) particles in silicone oil (dielectric constant 6.85). (b) The application of electric field caused the particles to form chains and columns. The chains and columns moved away from each other creating particle-free regions. (c) A periodic arrangement of positively polarizable particles. The direction of polarization is superimposed on the particles to illustrate the compressive nature of dipole-dipole forces along the electric field direction (E) and repulsive in the normal direction. (d) The initial periodic arrangement of 216 monodisperse particles was used in numerical simulation, as viewed along the applied field direction (the x-axis). (e-f) Snapshots after application of the field, which causes the particles to form chains and columns. The repulsive dipole-dipole forces caused the chains and columns to move apart, filling the entire computational domain and creating particle-free regions.

2.2.1 Molecular Dipole-Dipole Forces

It is worth noting that such spatial fragmentation does not occur in the materials that are stabilized by molecular dipole-dipole forces. For example, polar water molecules can reorient to form a tetrahedral network of hydrogen bonds with each vertex occupied by a water molecule [76]. This is possible for a water molecule because its dipole's spatial direction is determined by its orientation (and not by that of an externally applied field). However, this is not possible in a dielectrically monodisperse suspension because the direction of polarization, which is determined by the applied field's direction, is the same for all particles (and cannot change for a particle even if it rotates).

2.2.2 Dielectrically Polydisperse Suspensions

Our goal is to design a suspension in which the particles self-assemble to form a three-dimensionally connected pattern when an electric field is applied. This can happen only if the electric field induced forces between a particle and all of its nearest neighbors are attractive, as is the case for the materials stabilized by molecular dipole-dipole forces, e.g., water. Such a suspension will be cohesive, as its particles will come together to form a connected pattern when an electric field is applied.

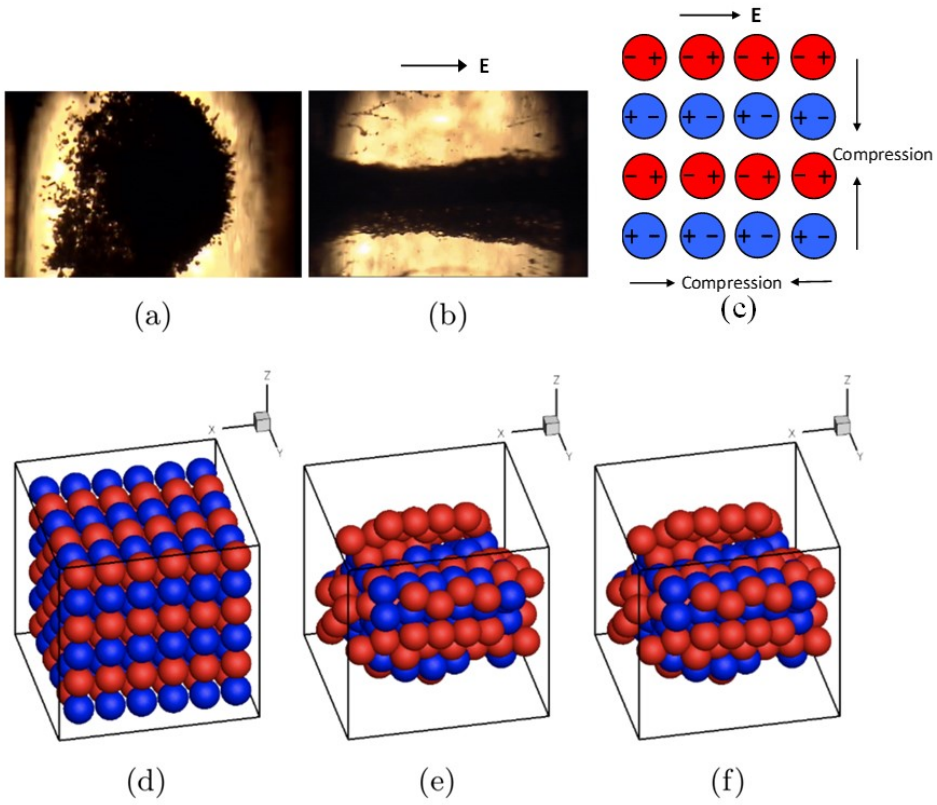

Figure 2.2 Electric field-induced rearrangement of a mixture of positively and negatively polarizable particles. (a) Top view of a suspension of a 50:50 mixture of aluminum oxide (average size 102.5 μm, dielectric constant 9.8) and calcium phosphate (average size 101.5 μm, dielectric constant 1.6) particles in silicone oil (dielectric constant 6.85). (b) The electric field's application causes the particles to form a band between the electrodes. Notice that the spatial distribution of the particles did not fragment into chains and columns and that the particles are packed tightly in the plane perpendicular to the electric field direction. Some particle scale gaps formed because of the incomplete mixing of aluminum oxide and calcium phosphate particles and the non-uniformities in the shape and size of the particles. (c) A periodic suspension of positively and negatively polarized particles. The direction of polarization is superimposed on the particles to illustrate the compressive nature of dipole-dipole forces along the electric field and the perpendicular direction. (d) The initial periodic arrangement of a 50:50 mixture of positively and negatively polarizable particles used in numerical simulation. The magnitudes of their polarizabilities are the same. The electric field is along the x-direction (e) Snapshot after applying the field; the particles coalesce in the y- and z-directions and align in the x-direction, decreasing the volume of the region occupied by the particles.

An electrically cohesive suspension can be formed by suspending a mixture of positively and negatively polarizable particles in a dielectric liquid. We illustrate this idea by considering a periodic arrangement of particles in Figure 2.2(c). Notice that the force between a particle and its nearest neighbors is attractive both in the field direction and in the perpendicular plane. The dipole-dipole forces cause particles to come closer, and so their distribution does not fragment into chains and columns. This was also the case in our experiments where the initial distribution of particles was not periodic, and the shape of the particles was only approximately spherical. An arbitrary initial configuration containing a mixture of positively and negatively polarizable particles (Figure 2.2(a)) did not fragment into chains and columns upon applying the electric field. Instead, the particles rearranged to form a band parallel to the electric field direction with tightly packed particles in the plane perpendicular to the field (Figure 2.2(b)). Tight packing happens because each particle is attracted to its nearest neighbors in both the parallel and perpendicular directions to the applied field. The DNS results presented in Figure 2.2(e) show that the particles formed chains parallel to the electric field direction and packed tightly together on applying an electric field, leaving about one half of the domain free of particles. The particles of the same type in the neighboring chains are staggered in the electric field direction, making their arrangement stable. The staggered chains combine to form sheets that are sandwiched by similar sheets of the oppositely polarized particles. On the other hand, as noted earlier, when only positively or negatively polarizable particles are present, the chains and columns move apart, increasing the volume over which they are distributed (see Figures 2.1b and 2.2b for comparison). Chain formation in the field direction is noticeable as the magnitude of forces along the field direction is twice that of the forces in the perpendicular direction (see SI for details). The assembled distributions are, therefore, anisotropic.

In our experiments, the suspensions were formed by thoroughly mixing particles before applying the electric field, which is essential to ensure that the suspension properties are uniform since they cannot mix on their own. When particles are not well mixed before applying the electric field, there are regions where the particle distribution locally fragments into chains and columns, indicating that particles' local number ratio is not suitable for forming a connected pattern. This behavior of suspensions is different from that of molecular systems, where particles can mix on their own as they are constantly moving and colliding with each other under the action of thermal forces.

2.2.3 Yield Stress in Dielectrically Polydisperse Suspensions

The formation of a band of closely packed particles without fragmentation in Figure 2.2(b and f) demonstrates that the suspension particles attract their nearest neighbors. To show that this change in the microstructure also causes changes in the suspension's mechanical properties, we measured its yield stress. For a suspension of positively (aluminum oxide) and negatively (calcium phosphate) polarizable particles, the yield stress was measured as a function of the volume fraction of positively polarized particles at three different electric field intensities (Figure 2.3). The total mass of particles in these experiments was kept constant while their respective volume fractions, which changes their number ratio or stoichiometric ratio, were varied. The figure shows that the yield stress of a mixture of positively and negatively polarizable particles was consistently greater than that of the suspensions consisting of only one type of particles, which indicates that the attraction between the particles is increased. Also, the yield stress increased with increasing electric field intensity. There is a relatively sharp peak of yield stress for a 40-60% mixture, which corresponds to the number ratio of 0.65:1 of aluminum oxide to calcium phosphate particles. (Note that this estimate is based on their average diameters, but in our experiments, the particles

used were not spherical, and their mean diameters varied). Additional experimental results are included in Supplementary Information.

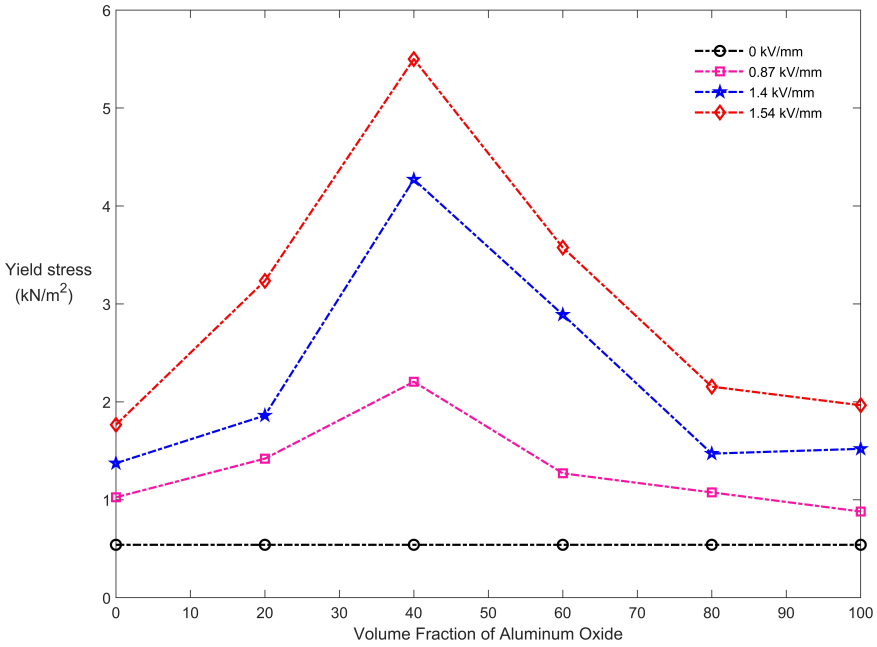

Figure 2.3 Yield stress as a function of the percent volume of aluminum oxide particles for three electric field intensities (see Supplementary Information Section 2). The yield stress was maximum when the volume fraction of aluminum oxide particles was around 40%.

We also conducted direct numerical simulations to determine the volume ratio range for which particles come together to form a connected pattern without fragmenting into chains and columns. For example, Figures 2.2 and 2.4, where the magnitudes of polarizabilities of positively and negatively polarized particles are equal, show that particles continue to form connected patterns even when the volume (or number) ratio deviates from 1:1. Figure 2.4a shows that there are changes in the microstructure with the number ratio resulting in a range of arrangements such as (i) the same type of particles arrange on sheets which sandwich the sheets of the oppositely polarized particles, (ii) the tubes of one type particles surround the chains of the oppositely polarized particles, and (iii) the oppositely polarized particles connect the columns consisting of one type of particle. The staggering of particles in the field direction makes the formation of sheets possible, and the sheets align so that their normal vectors are perpendicular to the electric field direction. For unequal sized particles, a larger number of smaller particles are needed to form a cohesive cluster. Furthermore, particles self-assemble into connected patterns even when the volume ratio deviates to 1:0.39. However, as the yield stress data of Figure 2.3 indicates, the attraction between the particles reduces from the peak value when the volume ratio deviates from the optimal value (also see Supplementary Information).

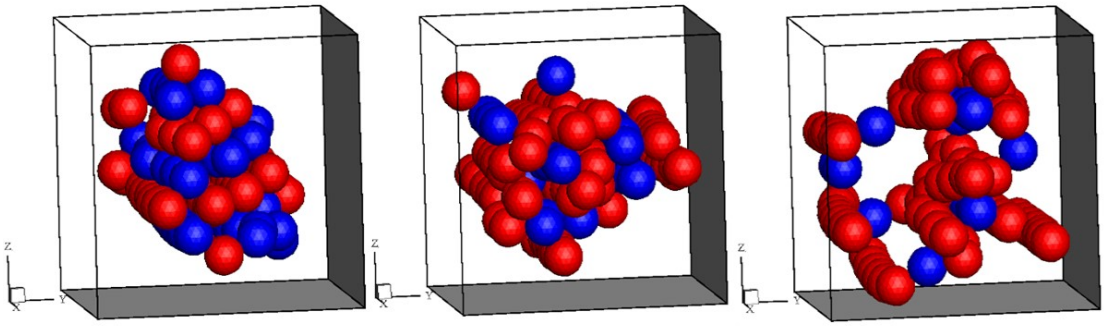

(a) 49-47 (b) 69-27 (c) 90-10

Figure 2.4 Dependence of the microstructural arrangement on the number ratio of positively and negatively of polarizable particles. (a) The magnitudes of polarizability and sizes are equal. There is a range of number ratios around 1:1 for which the particles pack together tightly, but the gaps begin to appear when the ratio deviates from 1:1. (b) The magnitudes of polarizability are equal, and the size ratio is 0.5. The arrangement consists of chains of larger particles that are surrounded by smaller particles. (a) 49-47 (b) 69-27 (c) 90-10

In general, when the sizes of both types of particles vary, and their polarizabilities are different, the yield stress data and the DNS results discussed in SI show that a cohesive pattern is possible only when the volume fraction of weakly polarizable particles is larger so that $V_p\beta_p \approx -V_n\beta_n$. Here β_p and β_n are, respectively, the Clausius-Mossotti factors of the positively and negatively polarizable particles, and V_p and V_n are their respective volume fractions.

Numerical simulations show that these results are also applicable to nanoparticle mixtures for which Brownian forces are important. However, as expected, the intensity of electric field required to direct their self-assembly and arrest their Brownian motion relative to one another is greater (see SI, Section 4). The strength of inter-particle forces is adjustable—it can be modified by changing the electric field intensity or frequency, by selecting a different suspending fluid or particles of varying dielectric constants, and/or by varying the volume fractions and the sizes of the two types of particles (see Supplementary Information). Furthermore, since it is possible to have more than two types of particles, with different polarizabilities and sizes, and

that their volume fractions can be varied, a range of complex arrangements can be obtained by changing these parameters. A comprehensive study of the roles of these parameters in self-assembly is beyond the scope of this study.

In conclusion, fragmentation of particles into chains and columns, which occurs when an electric field is applied, limits our ability to self-assemble cohesive three-dimensionally connected micro and nanoparticle aggregates in suspensions using this technique. This problem can be overcome by using a suitable mixture of positively and negatively polarizable particles for which particles spontaneously rearrange themselves, such that they attract all of their nearest neighbors and thus come together. The approach can be used to form a range of three-dimensional hierarchical patterns that depend on parameters such as their polarizabilities, the size ratio, and the number ratio of particles. This ability to utilize the dielectric polydispersity to guide self-assembly is elegant, tunable, and scalable. It is a significant step towards making engineered micro and nanoscales self-assemblies as ubiquitous as the molecular self-assembly observed in nature.

2.3 Methods

2.3.1 Experiments

Experiments were conducted in a rectangular prism-shaped device, which was 70 mm long and 24 mm deep. The distance between the device's sidewalls, where the electrodes were mounted, was varied between 4 and 7 mm. A variable frequency AC signal generator (BK Precision Model 4010A) was used along with a high voltage amplifier (Trek Model 610E) to apply high voltages (see Figure 2.8). The frequency used for the results reported in this paper was 100 Hz. The arrangement of particles was recorded using a digital camera connected to a Nikon Metallurgical microscope (MEC600).

The yield stress was determined by measuring the force on a thin 1cm x 1cm glass plate (100 μm thickness) when it is pulled up normal to the applied field direction, which is similar to the method used in Erb, et al. [67] (see Figure 2.9). The plate dimensions were much larger than the size of suspended particles, ensuring that the measured stress was independent of its size. The plate was connected to a force gage mounted on a vertical slide, which was moved at a constant speed by a DC motor giving the shear rate of $\sim 0.22s^{-1}$. The force initially increased with time, and then after reaching a maximum value, it decreased to a steady-state value. The maximum force was used to obtain the yield stress. The top surface of the fluid in these experiments was a free surface, and so the fluid was not subjected to any external normal stress, which could increase the yield stress because of particle jamming. The suspending fluid was silicone oil (FS 1265, Dow Chemicals) with a dielectric constant of 6.85. The suspensions were formed using aluminum oxide (Acros Organics, dielectric constant 9.8) and calcium phosphate (dielectric constant 1.6) particles. The mean particle size of aluminum oxide particles was 102.5 μm and of the calcium phosphate particles was 101.5 μm. As the dielectric constant of aluminum oxide particles is greater than that of silicone oil and calcium phosphate particles is smaller than that of silicone oil, the former particles were positively polarized and the latter negatively. The dielectric constant of the glass plate was approximately the same as that of silicone oil. This ensured that neither calcium phosphate nor aluminum oxide particles were strongly attracted or repelled by the glass plate.

The suspensions of particle mixtures were formed by thoroughly mixing aluminum oxide and calcium phosphate particles before and after they were suspended in silicone oil. The total mass fraction of particles in the suspension was held constant, while the volume fractions of the two types of particles were varied. The mixtures considered contained 0:100, 20:80, 40:60, 60:40, 80:20, 100:0 % fractions by volume of aluminum oxide and calcium phosphate particles. Since the only parameter varied

is the relative volume fraction of particles, the yield stress measures how the cohesive forces vary with the volume fraction. The experimental results in this paper are for particles about 5 to 100 micrometers in diameter; the results for nanoparticles are not included as agglomeration made their mixing difficult.

2.3.2 Direct Numerical Simulations (DNS)

A DNS approach based on the finite element method was used to study particle scale structure evolution in the dielectrically monodisperse and bi-disperse suspensions [74, 75, 76, 77, 78]. In our code, the governing mass and momentum conservation equations for the fluid and particles' motion are solved simultaneously. The rigid body motion constraint inside the particles is enforced by the distributed Lagrange multiplier method, and the buoyant weight of particles is neglected due to their small size. The Maxwell stress tensor approach is used to compute the electric stress from which the electric forces acting on the particles were computed. The approach, therefore, incorporates multibody electrostatic interactions among the particles.

The simulations were performed in the rectangular prism-shaped computational domains. As with the experiments, a uniform electric field was applied using the electrodes mounted in the domain walls parallel to the yz-coordinate plane. A typical computational domain size was $16a$, where a is the radius of the particle. Initially, particles were placed on a lattice, and the fluid and particle velocities were assumed to be zero. For the cases where the initial state was assumed to be randomly mixed, the particle properties at a given position were selected using a random distribution. For the cases in which the initial pattern was assumed to be periodic, the properties of a period cell were selected to be the same as the suspension's average properties. The fluid velocity at the domain boundaries was assumed to be zero and when the distance between the particle surface and the wall is less than $0.05a$, a repulsive wall force was applied to ensure they remain within the domain [74, 75, 76, 77, 78]. The presence

of the particles made the electric field non-uniform giving rise to the dipole-dipole forces that caused particles to rearrange. The parameters used for the simulations described in the paper are stated in Supplementary Information.

2.4 Supplementary Information

2.4.1 Mechanics of Particle Chains and Columns Formation

In this section, we first discuss the point-dipole (PD) approximation of the forces that act on particles in a uniform electric field and the direct numerical simulation (DNS) results that were used to describe the mechanism by which the particles form chains and columns. When a dielectric particle suspension in a dielectric fluid is subjected to an electric field, the particles become polarized and interact electrostatically and hydrodynamically with each other. The PD approximation provides a simple mechanistic explanation for the formation of particle chains and columns. The interaction force on a spherical particle i due to another particle j in the point-dipole approximation limit is given by [56, 79]

$$F_D(r,\theta) = 12\pi\varepsilon_0\varepsilon_c\beta_i\beta_j E_0^2\frac{(a_i a_j)^3}{r^4}((3\cos^2\theta - 1)e_r + \sin 2\theta e_\theta) \tag{2.1}$$

where $e_r = \frac{r_j - r_i}{|r_j - r_i|}$ is the unit vector along the line joining the centers of the spheres, e_θ is a unit vector normal to e_r in the plane containing the electric field direction, and θ is the angle between the electric field direction and e_r. Here $r = |r_j - r_i|$ is the distance between the particles, E_0 is the electric field intensity, $\varepsilon_0 = 8.8542 \times 10^{-12}$ F/m is the permittivity of free space, a_i and a_j are the radii of the two particles and $\beta_i(\omega) = Re(\frac{\varepsilon_\pi^* - \varepsilon_c^*}{\varepsilon_\pi^* + 2\varepsilon_c^*})$ is the Clausius-Mossotti (CM) factor of the i^{th} particle. Here ε_{pi}^* and ε_c^* are the frequency-dependent complex permittivities of the i^{th} particle and the suspending liquid, respectively. The complex permittivity is $\varepsilon^* = \varepsilon - \frac{j\sigma}{\omega}$, where ε is the permittivity, σ is the conductivity, ω is the frequency of

the applied ac field and $j = \sqrt{-1}$. The point-dipole approximation assumes that the distance between the particles is much larger than their radii, and hence its accuracy decreases when the distance is small. The direct numerical simulations based on the Maxwell stress tensor approach is used to improve accuracy, as we discuss below.

We first consider the case of two identical particles, i.e., $a_i = a_j = a$ and $\beta_i = \beta_j = \beta$. Hence, $\beta_i\beta_j = \beta^2 > 0$. Therefore, the radial component of force is attractive for $\theta < \cos^{-1}(\frac{1}{\sqrt{3}}) =\sim 54.74^\circ$ and repulsive for $\theta >\sim 54.74^\circ$. The magnitude of attraction is maximum when $\theta = 0^\circ$ (the line joining the centers is parallel to the electric field direction), whereas the magnitude of repulsion is maximum for $\theta = 90^\circ$ (the line joining the centers is perpendicular to the electric field direction). The symmetry of the problem implies that it is sufficient to consider the range $\theta \leq 90^\circ$. Therefore, when two particles are aligned so that the line joining their centers is parallel to the electric field direction, they attract, and when the line joining their centers is perpendicular, they repel. When θ is different from 0° or 90° the dipole-dipole force is not along the line joining the centers, which gives rise to a torque that causes the particle pair to rotate so that the line joining their centers becomes parallel to the electric field direction [56]. If $\theta > 54.74^\circ$, the particles initially repel each other while the torque causes θ to decrease and when $\theta < 54.74^\circ$ they attract and θ continues to decrease so that the particles align with the line joining their centers parallel to the electric field.

The mechanisms described above cause nearby particles to form chains parallel to the electric field direction (see Figure 2.5). The chains are under compression as the dipole-dipole forces between the particles of a chain are attractive. The interaction force between the particles of two nearby chains is complex in the sense that it can cause the chains to repel or merge to form a column. Our experiments and direct numerical simulations (DNS) show that the chains repel if their particles are aligned symmetrically, i.e., the line joining the center of a particle of the first chain and the

center of the nearest particle of the second chain is perpendicular to the electric field, as described in Figure 2.5. But, if the particles of the chains are staggered, and the distance between the chains is less than approximately $2.48a$, they weakly attract and join to form a column. Notice that the distance between two staggered chains in contact is $\sqrt{3}a$. The chains for which the distance is greater than $\sim 2.48a$, repel even when they are staggered. Such repelling chains can rotate and merge to form a single long chain. The nearby columns also repel, and so, as shown in Figure 2.6, they move apart, resulting in the formation of particle-free regions.

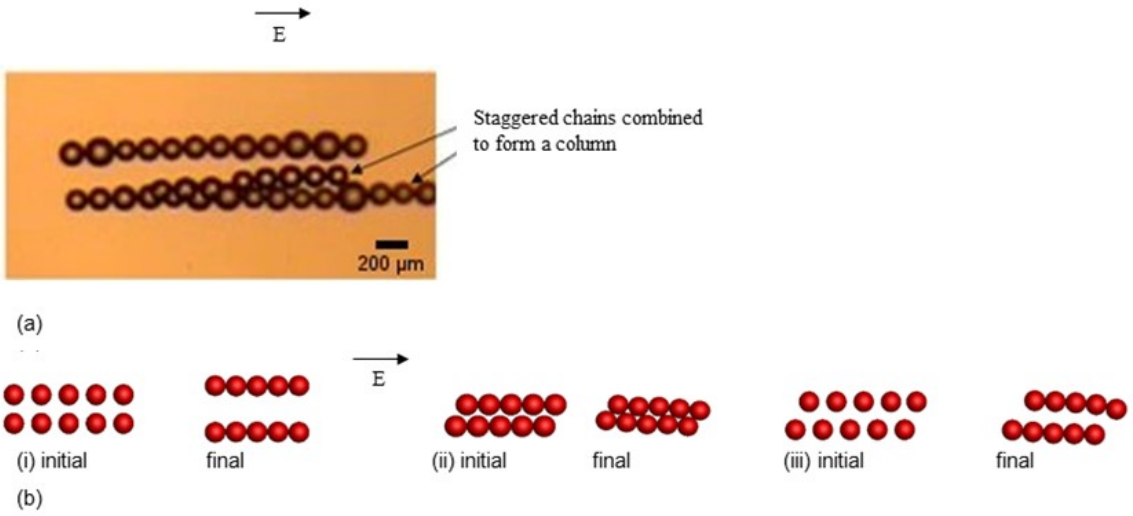

Figure 2.5 Forces between particle chains and columns in a uniform electric field. The applied electric field is in the horizontal direction; it is applied by the electrodes mounted in the left- and right side walls of the device/computational domain. (a) The photograph shows three chains of glass particles on the surface of corn oil. The lower two chains have merged to form a column. Notice that these chains' particles are staggered, and so the dipole-dipole force between the chains is attractive. The upper chain particles are not staggered relative to that of the lower one, so the dipole-dipole force between the upper and lower chains is repulsive. The images were taken by a camera mounted above the device. It was difficult to experimentally study the interaction between isolated chains that were fully immersed in the liquid as they slowly sedimented to the device's bottom. Once at the bottom, the chains did not move freely because of the friction with the bottom surface. Therefore, we studied the interaction between the particle chains that were trapped on the corn oil surface. These chains were free to move on the surface and so aligned according to the electric forces acting on them. (b) The DNS results for the interaction between two chains of positively polarizable particles. If the chains are aligned symmetrically, as in (i), the chains' particles come closer, and the chains move apart. If the chains are staggered, and the distance between them is smaller than approximately 2.48a, as in (ii), they merge to form a column. If the distance between the chains is larger than 2.48a, as in (iii), they repel even when they are staggered. These simulation results are similar to the experimental results shown in part (a) of this figure.

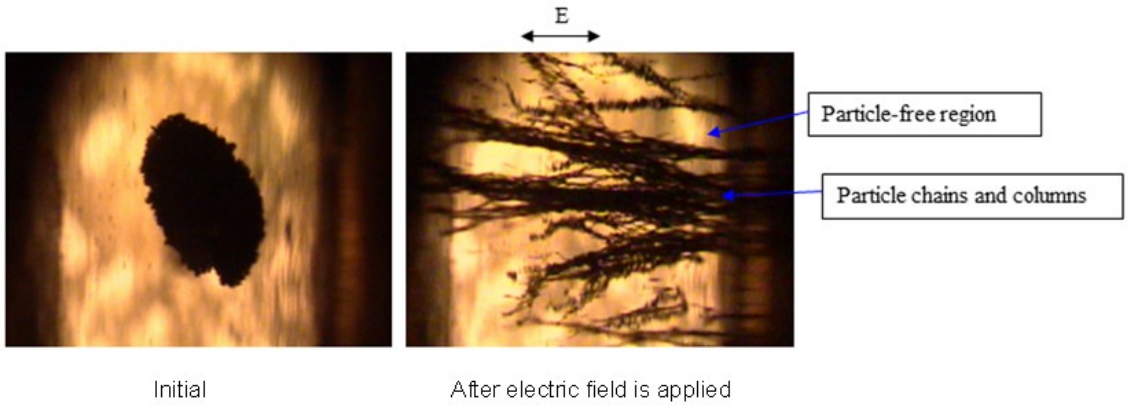

Figure 2.6 Formation of particle chains and columns in a dielectrically monodisperse suspension of calcium phosphate particles which were negatively polarized. Initially, particles are contained in the approximately oval-shaped regions at the bottom of the device. The photographs are taken by a camera mounted directly above the device. The electric field causes particles to form chains and columns, some of which spanned the gap between the electrodes. The chains and columns move away from each other, creating regions with no particles.

We next consider the case where the first type of particles are positively polarized ($\beta_i > 0$) and the second type are negatively polarized ($\beta_j < 0$), and so $\beta_i\beta_j < 0$. The dipole-dipole force, therefore, is negative (repulsive) for $\theta < 54.74°$ and positive (attractive) for $\theta > 54.74°$. The repulsive force is maximum for $\theta = 0°$, and the attractive force is maximum for $\theta = 90°$. The force for any other value of θ is not directed along the line joining the particle centers, causing the particle pair to align so that the line joining their centers is perpendicular to the field direction. This can be seen in Figure 2.7, which shows that a chain of glass particles (positively polarized) and a chain of polystyrene particles (negatively polarized) attract to form a two-chain column, in which the line joining the centers of neighboring particles is perpendicular to the electric field. For this two-chain column, the inter-particle attractive forces are strong in both the parallel and perpendicular directions to the electric field. If the chains are initially staggered, they become symmetrically aligned and come closer to form a column.

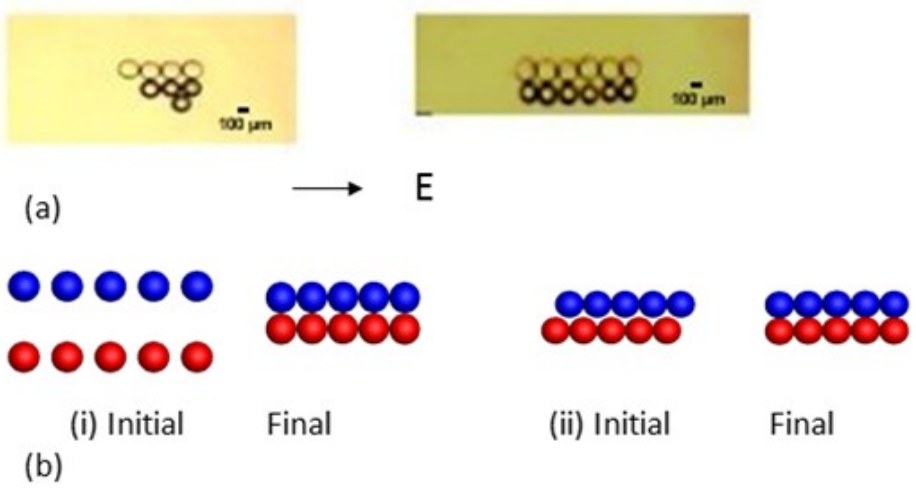

Figure 2.7 Forces between the particle chains of positively polarized (red) and negatively polarized particles (blue). The electrodes are mounted in the left and right sidewalls. The applied electric field is horizontal (a) A two-chain column is formed by the merger of a chain of positively polarized glass particles (radius 71 μm) and a chain of negatively polarized polystyrene particles (darker colored, radius 64 μm). Notice that the particles of the upper and lower chains are aligned so that the line joining their centers is perpendicular to the electric field direction. Also, notice that there is one polystyrene particle in the third row of the left photograph which is aligned in a staggered arrangement as its polarization is the same as that of the chain above. (b) The DNS results for the interaction between a chain of positively polarized particles (red, $\beta_1 = 0.25$) and a chain of negatively polarized particles (blue, $\beta_2 = -0.25$). The electric field causes the particles of the same polarizabilities to come together along the field direction and those of the opposite polarizabilities to align so that the line joining the centers of the nearest positively and negatively polarized particles is perpendicular to the electric field direction. In (i), the chains were initially symmetrically aligned, and in (ii), they were initially staggered. The final arrangements were identical. The two types of particles have the same radii. The electric field applied was 600 V/mm.

2.4.2 Sample Mixture Preparation and the Role of Various Parameters on Yield Stress

The spatial distribution of particles shown in Figures 2.1-2.2, the yield stress data of Figure 2.3, and the DNS results of Figure 2.4 all demonstrate that by mixing positively and negatively polarizable particles in a suitable proportion, it is possible to form a suspension whose particles self-assemble themselves into a three-dimensionally connected pattern when it is subjected to a uniform electric field. In general, particles of suspensions experience hydrodynamic, buoyancy, Brownian, and electric forces. The buoyancy force can be neglected when the density differences are small. Also, in the absence of Brownian motion, which is the case for larger particles, particles' motion is determined by the balance of electric and hydrodynamic forces. In this case, the electric field intensity determines the speed with which particles self-assemble, but not their tendency to self-assemble. For smaller particles, Brownian forces are important, so self-assembly is possible only when the electric field intensity is large enough to overcome Brownian forces.

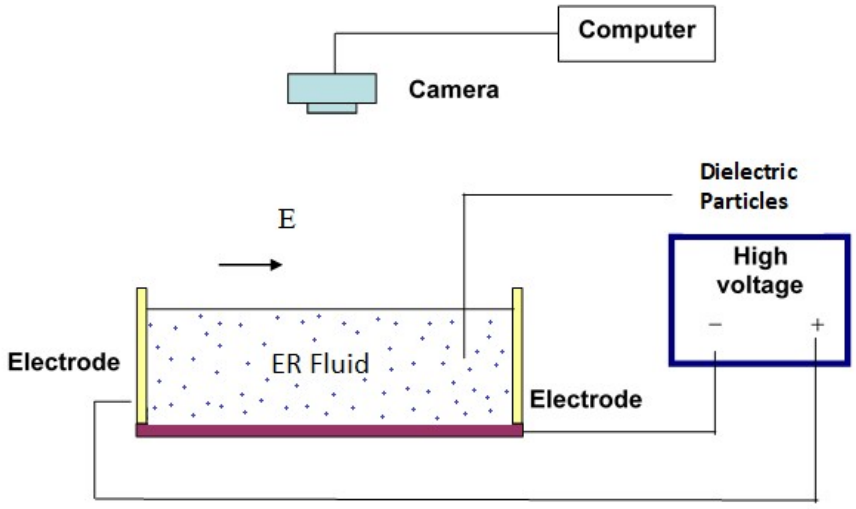

Figure 2.8 Schematic of the experimental setup. The electrodes are mounted in the left- and right side walls of the device containing a dielectric liquid. When an electric field is applied, particle chains are formed between these electrodes and the images are captured by an overhead camera.

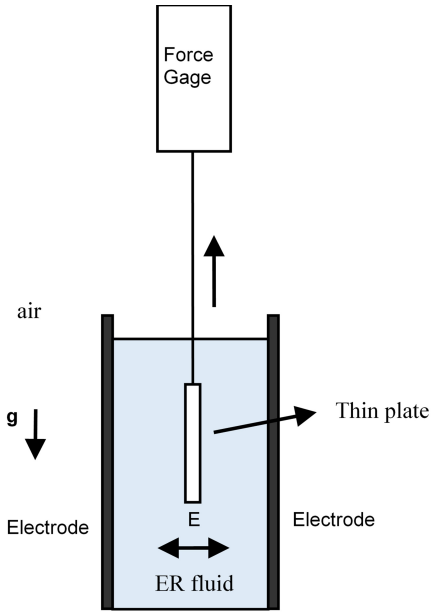

Figure 2.9 Schematic of the experimental setup used to measure yield stress. The electrodes are mounted in the left- and right sidewalls. The force acting on the plate is measured while it is moving in its plane at a constant speed.

(a) Sample preparation: In our experiments, the total mass of mixture particles in the suspensions were kept constant to ensure that the yield stress in the absence of the electric field was the same while their relative volume fractions were varied when the densities of both types of particles were approximately the same. This is important because the yield stress changes in the electric field's presence can be used to determine how the self-assembly behavior of a mixture of two types of particles depends on their volume fractions. The volume fraction of particles is related to the number ratio of particles, which, as discussed below, plays an important role in determining the particle scale arrangement.

To determine particles' volume fractions in a mixture, we must know the true volume of particles in each of the powders used for making the mixture. This cannot be obtained from their apparent volumes, as the powder particles do not pack tightly due to the presence of air pockets. Furthermore, when the densities of the two types of particles are different, the ratio of their mass fractions is not the same as the ratio

of their volume fractions. In this case, both the mass and the true density of particles must be used for determining the true volume of particles. Let $M_1, V_1, N_1 and \rho_1$ be the mass, volume, number, and density, respectively, of the first type of particles, and $M_2, V_2, N_2, and \rho_2$ be the respective values for the second type of particles. Then, the ratio of their volumes can be obtained using $\frac{V_1}{V_2} = \frac{M_1}{M_2}\frac{\rho_2}{\rho_1}$.

The particles used in our experiments were not monodispersed. Let R_1 and R_2 be the average radii of the two types of particles. The average number ratio of the two types of particles can be obtained from the volume ratio and the average radii. The number ratio based on the average radii is given by $\frac{N_1}{N_2} = \frac{V_1}{V_2}\frac{{R_2}^3}{{R_1}^3}$. The number ratio gives the number of negatively polarizable particles per positively polarizable particle in the mixture, i.e., it determines the mixture's stoichiometric ratio.

In addition to the aluminum oxide-calcium phosphate mixtures described in the paper, we considered mixtures of aluminum oxide with several sizes of hollow and solid glass and other particles. The expressions discussed above were used to obtain the ratio of volume fractions and the number ratios for these mixtures from the particles' radii, masses, and densities.

For hollow glass particles, the permittivity was obtained in terms of the radii ratio of the cavity and outer shell3, and the actual shell volume was incorporated in the computation of their effective densities. As the relative size of the cavity in the hollow glass particles considered in this study decreases with decreasing radius, both the effective density and permittivity increase with decreasing radius.

(b) Role of particle sizes and polarizability ratios in self-assembly: In this subsection, we present additional yield stress results in which the particle sizes and polarizabilities are varied. The aim of this study is to model the role of these parameters. The yield stress measurements were performed using the procedure described in the section on Methods.

Figures 2.10-2.16 show the yield stress as a function of the volume fraction of aluminum oxide particles for seven dielectrically polydispersed suspensions formed by mixing 102.5 μm (mean diameter) aluminum oxide particles (Acros Organics Brockmannn I) with: (i) 90 μm hollow glass spheres (Potters Q-CEL), (ii) 72 μm hollow glass spheres (Potters Q-CEL), (iii) 50 μm hollow glass spheres (Potters Q-CEL), (iv) 20 μm hollow glass spheres (Potters SPHERICEL), (v) 100 μm silica spheres, (vi) 120 μm extendospheres (Sphere One), and (vii) 160 μm extendospheres (Sphere One). Here the percent volume fractions is defined to be $\frac{volume\ of\ aluminum\ oxide\ particles}{total\ volume\ of\ particles} \times 100$. The CM factor of the aluminum oxide particles is 0.11, and of the 90 μm, 72 μm, 50 μm and 20 μm hollow glass particles are –0.39, –0.38, -0.36 and –0.35, respectively. As the CM factor of the hollow glass particles considered differs only slightly, these cases allow us to study relative particle sizes' role in the self-assembly process. Also, the CM factor of the hollow glass particles and the calcium phosphate particles are comparable.

The volume fraction of aluminum oxide particles at which the peak yield stress occurred in Figures 2.10-2.13 varied with the mean diameter of glass particles. There were two local yield stress peaks at low electric field intensities instead of a single one, which was the case in Figure 2.3. The presence of two peaks at low electric field intensities indicates that there are two possible particle scale arrangements, corresponding to different volume fractions of particles, which enhance the yield stress. For example, for case (i) shown in Figure 2.10, the peaks were at 30% and 60% volume fractions of aluminum oxide particles. However, when the electric field intensity was increased, there was only a single dominant peak at the 30% volume fraction of aluminum oxide particles. We remind the reader that for the case described in Figure 2.3, the peak yield stress was at around 40% volume fraction of aluminum oxide particles. The mean diameter of calcium phosphate particles was comparable to that

of aluminum oxide particles, and the CM factor of calcium phosphate particles was comparable to that of the hollow glass particles.

In Figure 2.10, the mean diameter of glass particles is about 12% smaller than that of aluminum oxide particles. Thus, the expressions discussed in the previous subsection imply that for the 30% volume fraction peak, the number ratio is 1:3. For the 60% volume fraction peak, which is present at the smaller electric field intensities, the number ratio is 1:6. For the higher electric field intensities, only the number ratio of 1:3 enhanced self-assembly. For case (ii) shown in Figure 2.11, where the average diameter of glass particles is approximately 35% smaller than that of the aluminum oxide particles, the 60% volume fraction peak emerged as the dominant peak when the electric field intensity was increased. Similar observations can be made in Figure 2.13, where the average diameter of glass particles is about 50% smaller than that of aluminum oxide particles. The experimental results of the particle mixtures containing a combination of aluminum oxide with silica particles and with extendospheres are shown in Figures 2.14-2.16.

Our experimental results indicate that when the yield stress of the suspensions formed using only aluminum oxide particles is comparable to that with only glass particles, there is a single dominant peak for the electric field intensities considered. For hollow glass and aluminum oxide particle mixtures, this happened when their particle sizes were comparable. However, when the yield stress values of the suspensions with only one type of particles differ substantially, as in Figures 2.10-2.12, there were two or more peaks at low electric field intensities. One of these peaks becomes dominant for the higher electric field intensities. We postulate that the appearance of one or two peaks' depends on the particle's' diameter ratio, which makes specific number ratios preferred for the particle level arrangements.

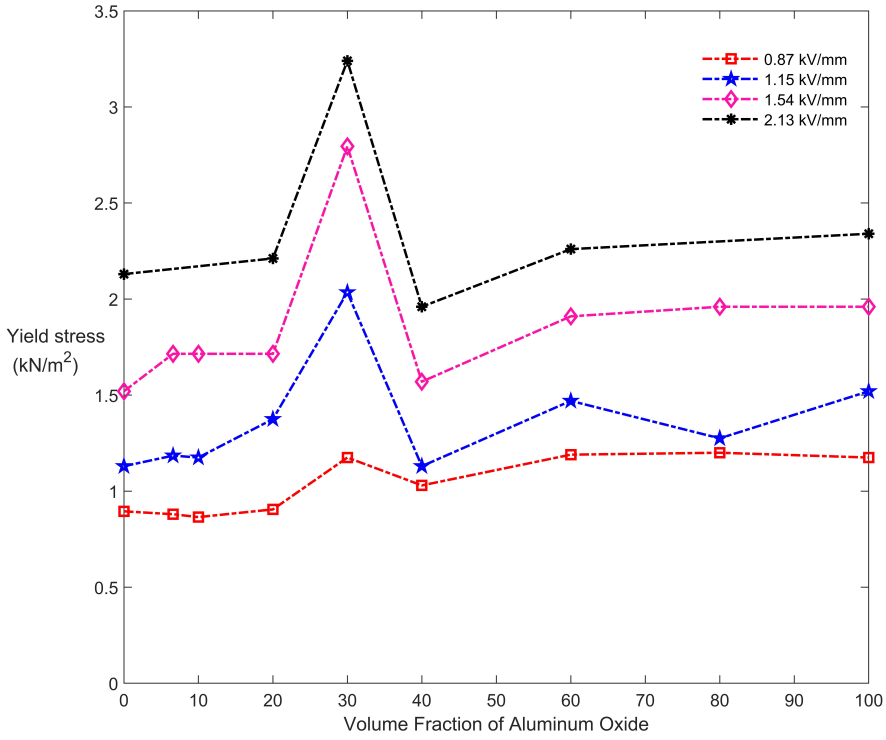

Figure 2.10 The yield stress as a function of the volume fraction of aluminum oxide particles for five electric field intensities. The sum of the volume fractions of the aluminum oxide and glass particles (90 μm) to the total volume was held constant at 0.50. The yield stress was maximal when the volume fraction of aluminum oxide particles was around 30%.

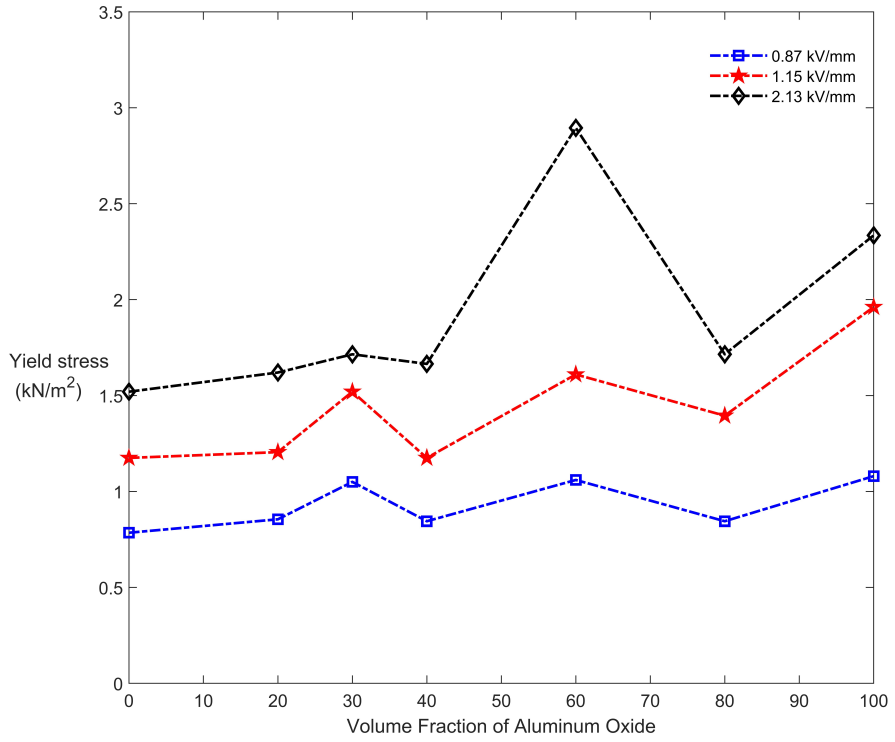

Figure 2.11 The yield stress as a function of the volume fraction of aluminum oxide particles for four electric field intensities. The sum of the volume fractions of the aluminum oxide and glass particles (72 μm) to the total volume was held constant at 0.46. The yield stress was maximal when the volume fraction of aluminum oxide particles was around 30%.

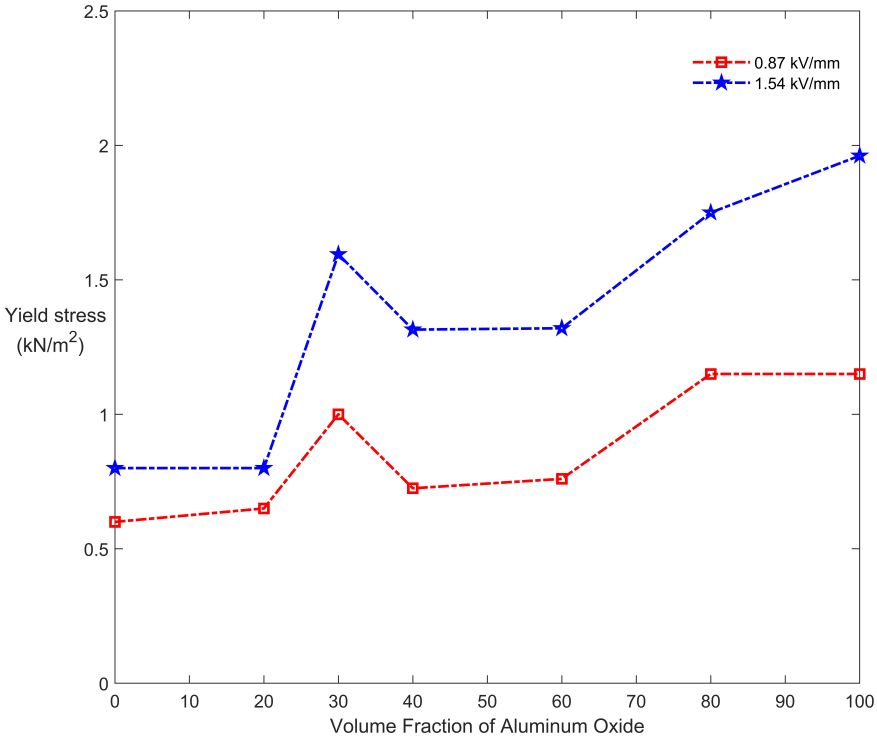

Figure 2.12 The yield stress as a function of the volume fraction of aluminum oxide particles for three electric field intensities. The sum of the volume fractions of the aluminum oxide and glass particles (20 μm) to the total volume was held constant at 0.46. The yield stress was locally maximal when the volume fraction of aluminum oxide particles was around 30%.

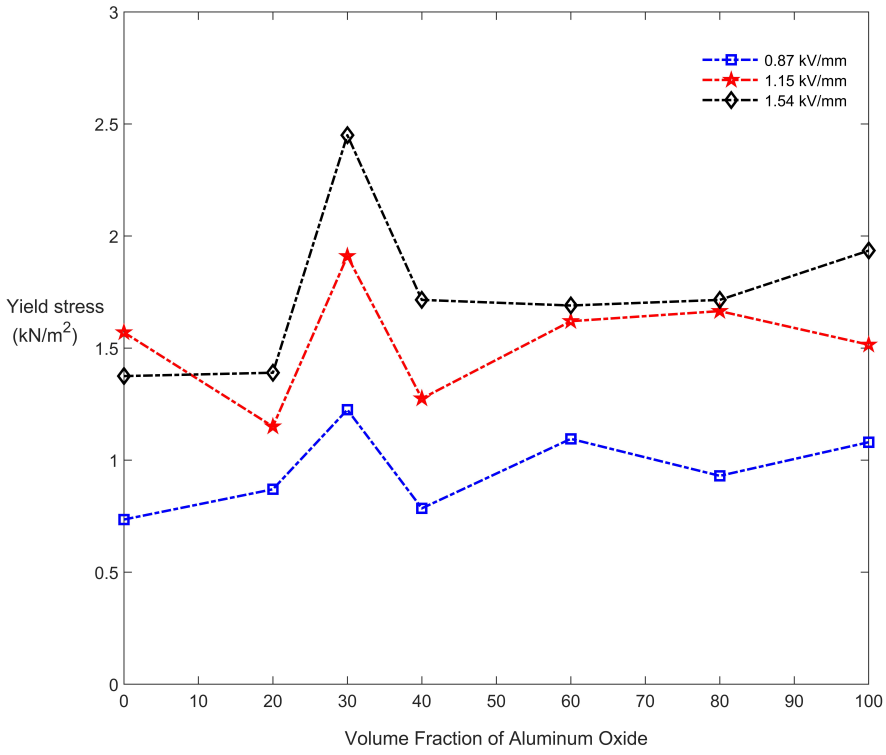

Figure 2.13 The yield stress as a function of the volume fractions of aluminum oxide and glass particles (50 μm) for five electric field intensities. The disappearance of secondary peaks can be seen at higher electric field intensities.

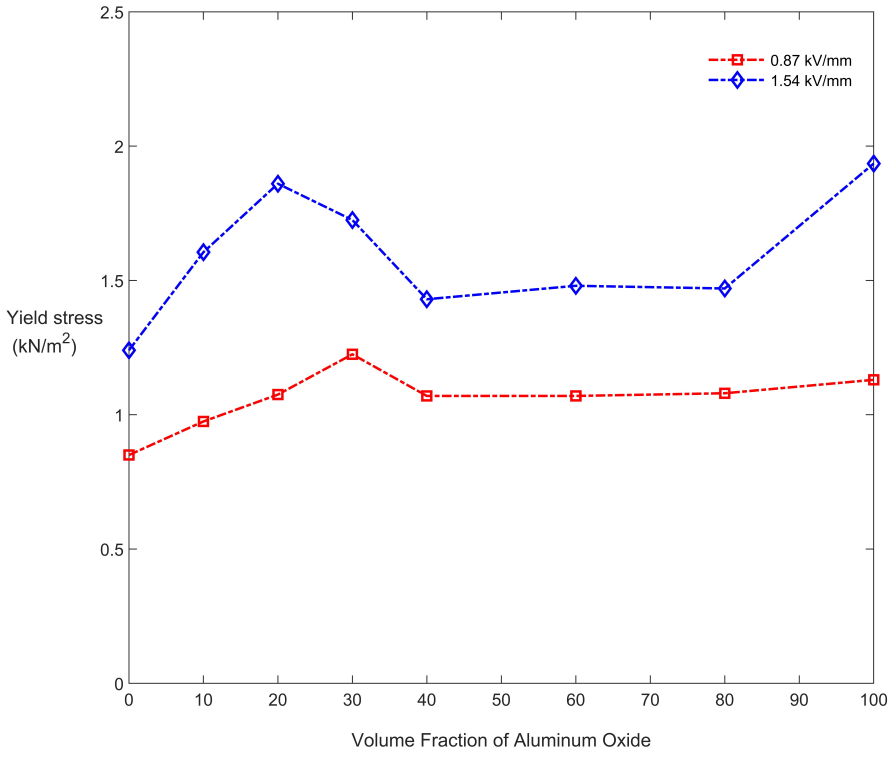

Figure 2.14 The yield stress as a function of the volume fraction of aluminum oxide particles for three electric field intensities. The sum of the volume fractions of the aluminum oxide and silica particles (100 μm) to the total volume was held constant at 0.46. The yield stress was maximal when the volume fraction of aluminum oxide particles was around 30%.

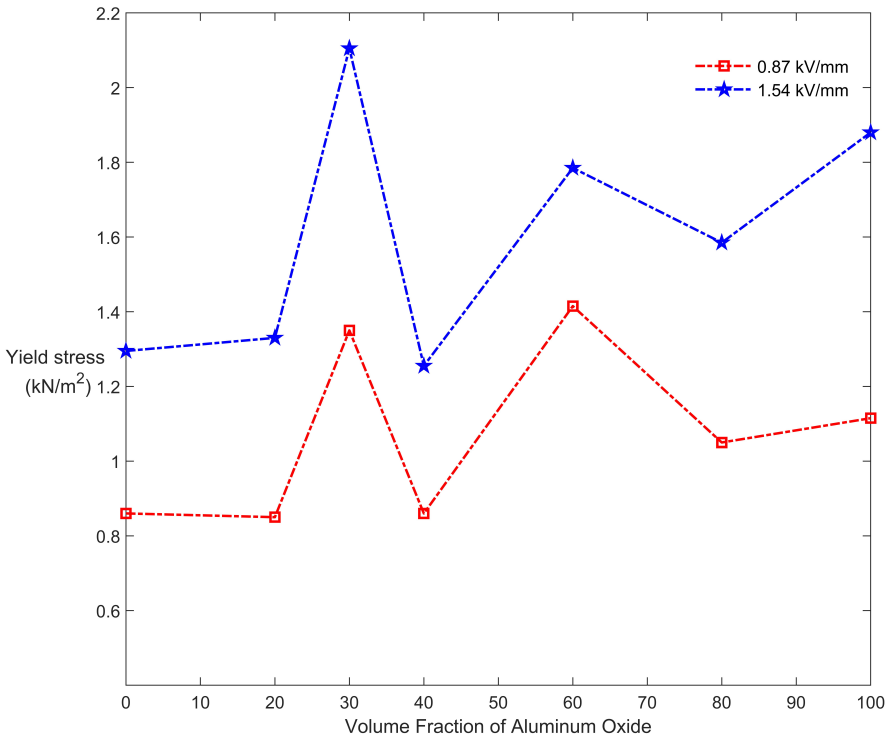

Figure 2.15 The yield stress as a function of the volume fraction of aluminum oxide particles for three electric field intensities. The sum of the volume fractions of the aluminum oxide and extendospheres particles (120 μm) to the total volume was held constant at 0.46. The yield stress was maximal when the volume fraction of aluminum oxide particles was around 30%.

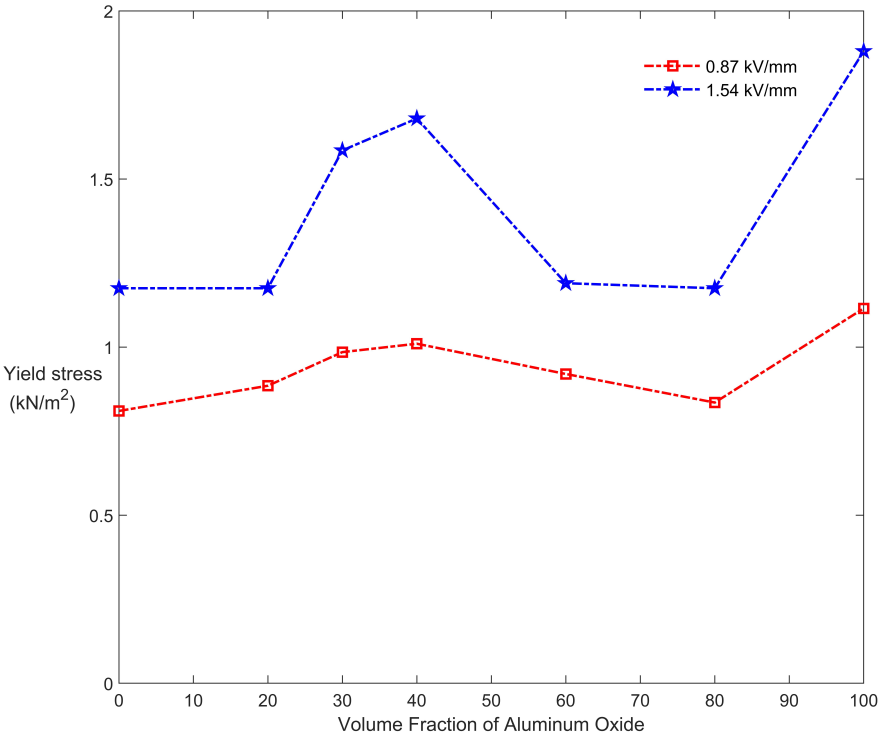

Figure 2.16 The yield stress as a function of the volume fraction of aluminum oxide particles for three electric field intensities. The sum of the volume fractions of the aluminum oxide and extendospheres particles (160 μm) to the total volume was held constant at 0.46. The yield stress was maximal when the volume fraction of aluminum oxide particles was around 40%.

2.4.3 Numerical Simulations

This section discusses the DNS results for the self-assembly behavior of suspensions of neutrally buoyant particles subjected to a uniform electric field. We first discuss the case of larger particles of radii 100 μm for which Brownian forces are negligible compared to electric and hydrodynamic forces. We will assume that in both cases, initially, particles are a well-mixed state. The electric forces cause particles to self-assemble, and the hydrodynamic forces resist their motion relative to the fluid during the self-assembly process. The simulations were stopped after a steady configuration was reached. The results are used to model the roles of parameters such as the CM factors and the number and size ratios of positively and negatively polarized particles on the nature of self-assembled configuration.

The parameter, $12\pi\varepsilon_0\varepsilon_c\beta_i\beta_j {E_0}^2 \frac{a_i {a_j}^3}{r^4}$, in Equation (2.1) can be written as $p^2 a_p^2 \beta_i' \beta_j' \frac{(a_i' a_j')^3}{r'^4}$. Here $p^2 = 12\pi\varepsilon_0\varepsilon_c\beta_p{}^2 E_0^2 {a_p}^2$, and the characteristic parameters are: a_p = radius of positively polarized particles, and β_p = CM factor of positively polarized particles. The dimensionless radii are $a_i' = \frac{a_i}{a_p}$ and $a_j' = \frac{a_j}{a_p}$, the dimensionless distance $r' = \frac{r}{a_p}$, and the dimensionless CM factors are $\beta_i' = \frac{\beta_i}{\beta_p}$ and $\beta_j' = \frac{\beta_j}{\beta_p}$. For this selection of the characteristic parameters, the dimensionless CM factor of the positively polarized particles, β_p', is equal to one and of the negatively polarized particles, β_n', is negative, and its magnitude is varied. The parameter p and the dimensionless parameters r' and β_n' are used to specify the problem parameters.

For the numerical results reported in this paper for non-Brownian particles, the diameter of the positively polarized particles is 100 μm, β_p is 0.1 and p = 25.42. The dimensionless CM factor (β_n') and size (r') of negatively polarized particles are varied to simulate the role of these parameters. For the cases requiring longer simulations, the electric forces were computed using the point dipole approximation, and the hydrodynamic forces were calculated using the Stokes drag formula. We next describe the role of particle size, polarizability, and number ratios on the assembled

arrangement. We first consider the case where the size of positively and negatively polarized particles is equal, and the dimensionless CM factor of negatively polarized particles is varied.

(a) Relative polarizabilities of positively and negatively polarized particles: Simulations show that the tendency of particles to self-assemble themselves into a connected pattern increases as the dimensionless CM factor of the negatively polarized particles (β'_n) is varied from -0.1 to -1.0, while holding all other parameters fixed. The number of positively and negatively polarized particles and their sizes are assumed to be equal. As $|\beta'_n|$ is increased, the magnitude of force among the negatively polarized particles, and the positively and negatively polarized particles increase, and the force among the positively polarized particles remains the same. Figure 2.17 shows that the particles come together with increasing $|\beta'_n|$, but only when it is between -0.8 and -1.0 that the mixture particles pack together tightly. We may, therefore, conclude that for the assumed parameter values, the mixture particles self-assemble themselves into a connected pattern only when the magnitudes of the CM factors of the negatively ($|\beta'_n|$) and positively polarized particles ($|\beta'_p|$) are comparable.

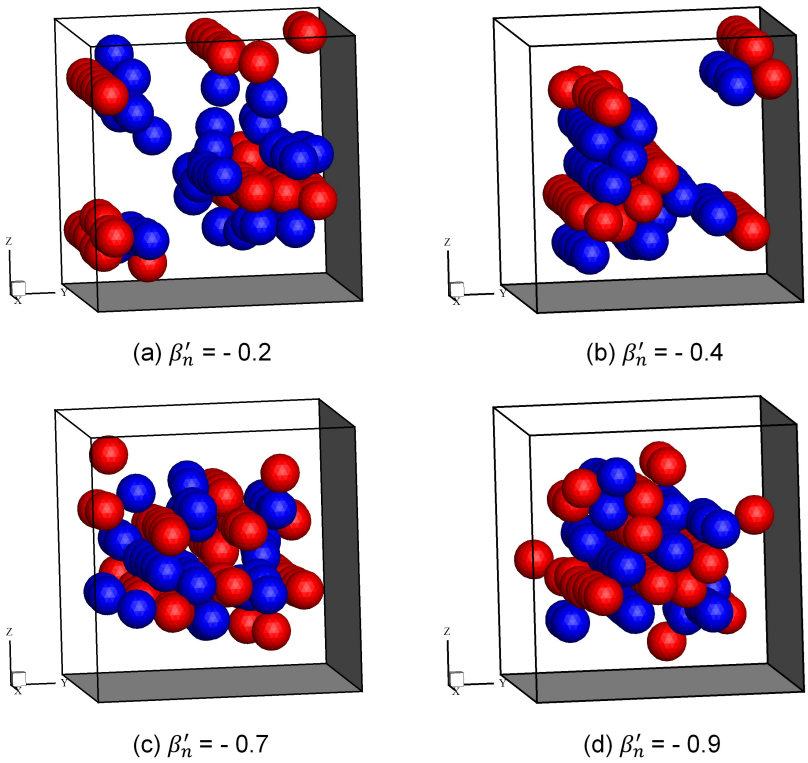

Figure 2.17 Steady-state arrangement of a mixture of positively and negatively polarized particles. 96 particles were initially arranged randomly and subjected to an electric field in the x-direction. There are equal numbers of positively and negatively polarized particles and their diameters are equal. The dimensionless CM factor of the positively polarized particles $\beta'_p = 1.0$ and of the negatively polarized particles ($|\beta'_n|$) is varied. The tendency to self-assemble to form a connected pattern increases as $|\beta_n|$ increases and becomes equal to β_p.

(b) Number ratio of positively and negatively polarized particles: Next, we describe how the tendency to self-assemble changes when the number of oppositely polarized particles is varied while holding their CM factors and sizes fixed. In Figure 2.18, $\beta_p' = 1.0$ and $\beta_n' = -0.3$. The figure shows that when there is an equal number of positively and negatively polarized particles, the dipolar forces do not bring them together (Figure 2.18 (a)). Thus, their distribution fragments into several columns. However, when the number of negatively polarized particles (which are weakly polarized) increases, as in Figure 2.18 (b), the particle chains merge to form a connected pattern. On the other hand, they again divide into several columns that move apart when the number of positively polarized particles (which are more strongly polarized) is greater than the number of negatively polarized particles, as shown in Figure 2.18 (c). From these results, we may conclude that if $\beta_p > |\beta_n|$, then to form connected self-assembly, the suspension must have a greater number of particles of negatively polarized particles, and vice versa.

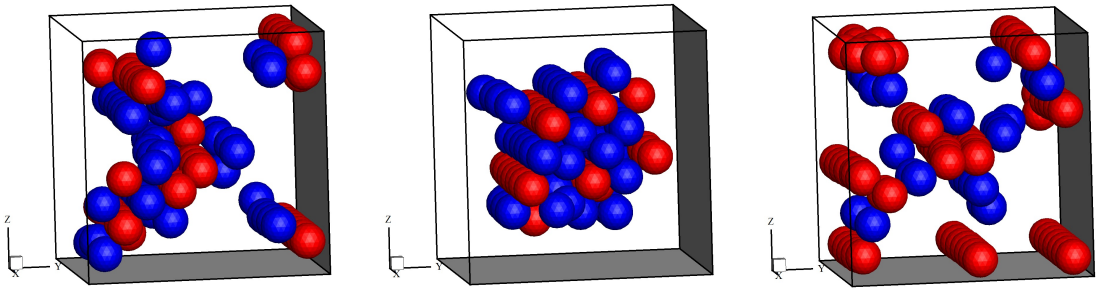

(a) 48 positive-48 negative particles

(b) 33 positive-63 negative particles

(c) 69 positive-27 negative particles

Figure 2.18 Steady-state arrangement of a mixture of positively and negatively polarized particles. Oppositely polarized particles are initially arranged randomly and subjected to an electric field in the x-direction. The dimensionless CM factor of the positively and negatively polarized particles is held constant at 1 and -0.3, respectively, and their sizes are the same, while their number is varied. (a) An equal number of oppositely polarized particles. (b) The number of positively polarized particles is 33, and negatively polarized particles are 63. (c) The number of positively polarized particles is 69, and negatively polarized particles are 27.

(c) The size ratio of positively and negatively polarized particles: The self-assembled arrangement changes when the relative sizes of oppositely polarized particles are varied while holding their CM factors and number ratio fixed. In Figure 2.19, $\beta'_p = 1.0$ and $\beta'_n = -0.1$. The figure shows that when the negatively polarized particles are four times smaller than the positively polarized particles, the forces among them cause most of the smaller particles to collect near the larger particle's equator (Figure 2.19 (a)). Here the equator is defined as the circle on the sphere's surface, which is perpendicular to the electric field direction (i.e., the x-direction). Also, notice that the smaller particles are arranged in two circular rings in the x-constant planes slightly offset from the equatorial plane. The particles in the two rings are staggered relative to one another. However, when the negatively polarized particles are only two times smaller, as in Figure 2.19 (b), they formed six chains (of different lengths) and did not collect on the surface of the positively polarized particle's equator. Three of these chains are attached to the positively polarized particle, and the other three chains are independent and away from the positively polarized particle. One particle from each of the connected chains is attached with the positively polarized particles at the latter's equatorial plane. The three attached particles, one from each chain, are evenly spaced along the equatorial circle.

When the particle sizes are equal, the negatively polarized particles formed two independent chains and a two-chain column (in which the particles were staggered relative to one another in the electric field direction), as shown in Figure 2.19 (c). The positively polarized particle attracted only one of the single-particle chains. This is due to the repulsive forces among the chains which keep them apart, and so only one chain came in contact with the positively polarized particle.

We may conclude from these results: (i) When the size ratio is small, the smaller sized particles collect near the oppositely polarized larger particle's equator. This tendency diminishes with increasing size ratio. (ii) When the size ratio approaches

one, the smaller sized particles form chains that repel each other, and so only one of the chains attaches to the oppositely polarized particle.

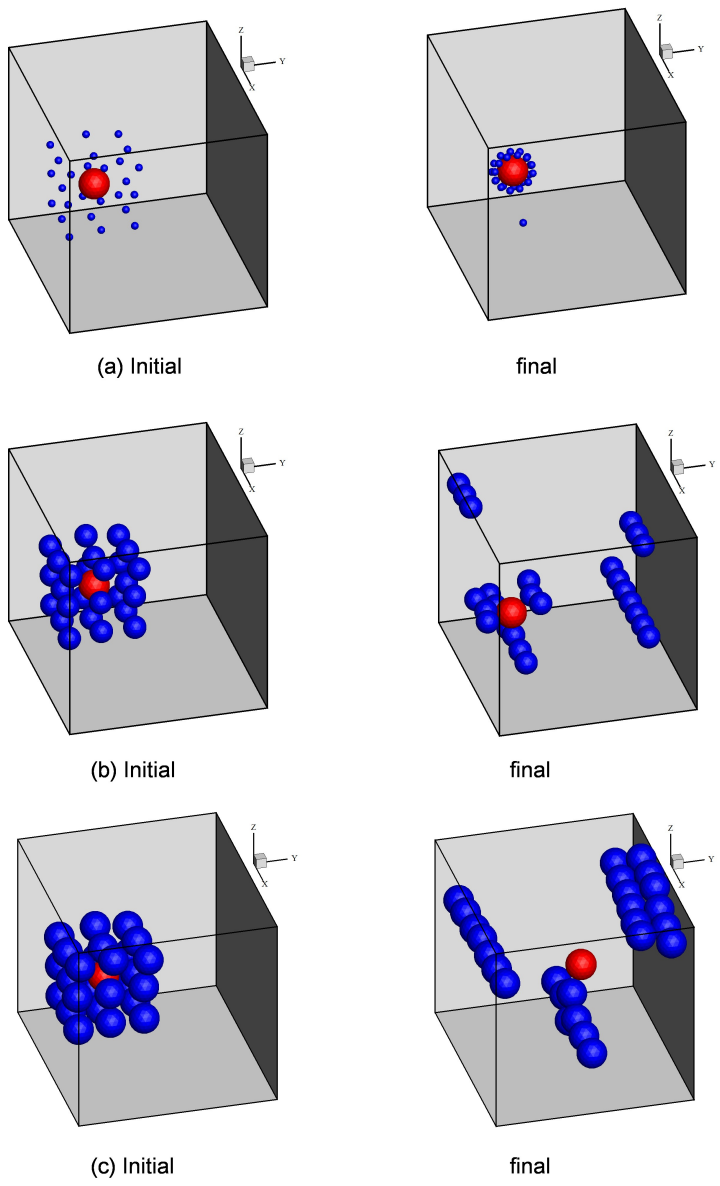

Figure 2.19 Steady-state rearrangements of a single positively polarized particle that is initially surrounded by 26 negatively polarized particles. The magnitude of the dimensionless CM factor of the negatively polarized particles is 0.1, and their size is varied. The initial and final arrangements are shown. (a) The ratio of the radii of the particles is 0.25. The negatively polarized (smaller) particles do not form chains; instead, all particles except for one were captured by the larger positively polarized particle near its equator. (b) The ratio of the radii of the particles is 0.5. Initially, the smaller particles formed six chains along the electric field direction. Three of these chains became attached to the positively polarized particle. (c) The ratio of the radii of the particles is 1.0. The negatively polarized particles formed two chains and one two-chain column. One of these chains became attached to the positively polarized particle.

(d) Relative polarizabilities of positively and negatively polarized particles of different sizes: We next consider the case where the particle size ratio is fixed at 0.5, and the CM factor of negatively polarized particles is varied. There are 189 negatively polarized particles and 27 positively polarized particles. So, the volume ratio of positively and negatively polarized particles is 1:0.875. The results presented in Figure 2.20 show that the polarizability ratio plays an important role in determining the final arrangement. Also, as is the case when the size ratio is one, the suspension particles self-assemble into a cohesive cluster when the CM factor of negatively polarized particles is within a specific range.

For example, 2.20 (b) shows that when the magnitudes of the CM factors of positively and negatively polarized particles are equal, and the volume ratio is 0.875, the particles form a cohesive cluster consisting of chains of larger particles. The chains are sandwiched by smaller oppositely polarized particles, which makes the cluster cohesive. The shape of the cluster, including the distribution of chains in the cluster, depends on the initial distribution of particles, but the overall qualitative arrangement of particles in the cluster remains similar. The cluster volume is smaller than the volume over which the particles were distributed initially. Simulations also show that when the magnitude of the CM factor of negatively polarized particles was between approximately 0.93 and 1.31, the mixture particles self-assembled into cohesive clusters. The distribution gradually fragments into chains and columns outside this range.

When the magnitude of the CM factors of the negatively polarized (smaller particles) is 2.6 (see Figure 2.20 (c)), there are chains of positively and negatively polarizable particles, some of which combined to form columns. There is a maximum of three chains of negatively polarized particles surrounding a chain of positively polarized particles. The remaining chains of negatively polarized particles, which did not combine with the chains of positively polarized particles, moved apart, leaving

gaps in-between them. This is due to the increased repulsion between the chains of negatively polarized particles due to their CM factor's increased magnitude. The columns of positively and negatively polarized particles also moved apart, which shows that the force between them was repulsive. Thus, for these parameter values, the particle mixture is not cohesive.

On the other hand, when the magnitude of the negatively polarized particles' CM factor is 0.4 (see Figure 2.20 (d)), their tendency to form chains is diminished, and so they collect individually around the chains of positively polarized particles to form columns. The columns, however, move apart, which indicates that the net force between them is repulsive. This is due to the weaker polarization of negatively polarized particles, which is not strong enough to make the net force between the composite columns attractive.

Similarly, when the volume ratio of positively and negatively polarized particles is 1:3.25 and $\beta_p = |\beta_n|$, particles do not self-assemble to form a cohesive cluster, as shown in Figure 2.21. There are 208 negatively polarized particles and eight positively polarized particles in the figure, and the radii ratio is 0.5. The positively polarized particles combine with nearby negatively polarized particles to form a cohesive cluster, but the remaining negatively polarized particles form chains that move apart from each other.

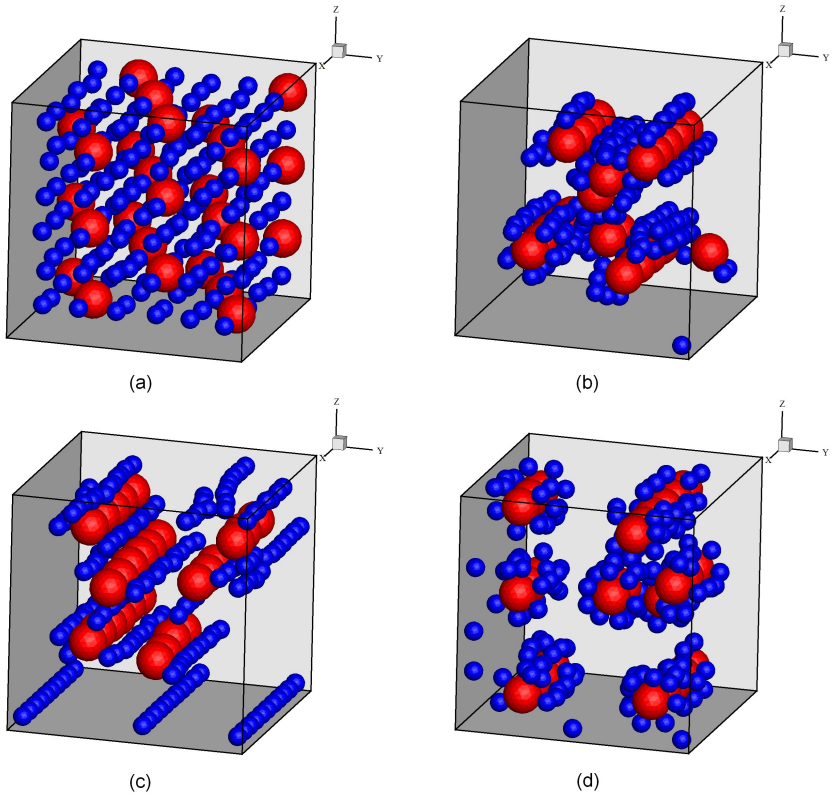

Figure 2.20 Steady-state arrangements of the mixtures of positively and negatively polarized particles for the size ratio of 0.5. There are 27 positively polarized particles and 189 negatively polarized particles. The initial arrangement is shown in (a). The dimensionless CM factor of the positively polarized particles is held constant at 1.0, and of the negatively polarized particles is: -1.0 in (b), -2.6 in (c), and -0.4 in (d).

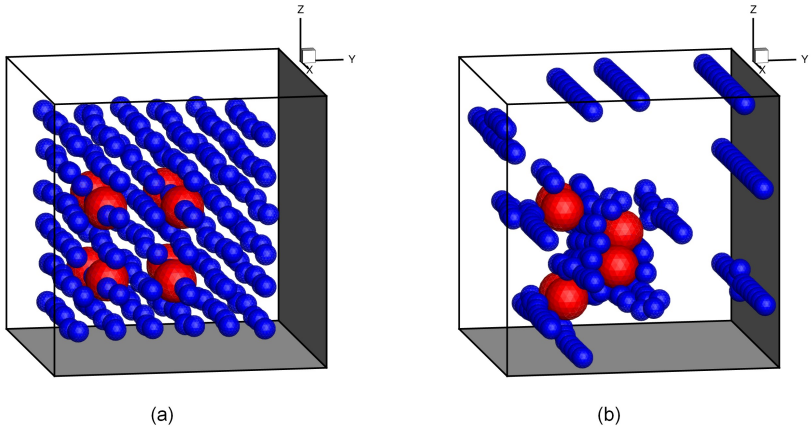

Figure 2.21 Steady-state arrangements of the mixtures of positively and negatively polarized particles for the size ratio of 0.5. There are 8 positively polarized particles and 208 negatively polarized particles. The initial arrangement is shown in (a), and the final in (b). The dimensionless CM factor of the positively polarized particles is 1.0, and of the negatively polarized particles is -1.0.

In summary, the simulation results discussed above show that well-mixed mixtures of positively and negatively polarized particles of different radii can also self-assemble to form cohesive clusters. This happens when the product of the volume of positively polarizable particles and their CM factor is comparable to that for the negatively polarizable particles. However, when this is not the case, although the oppositely polarized particles come together to form composite columns, the columns do not come together to form a cohesive cluster as the net forces between them are repulsive.

2.4.4 Condition for the Formation of Cohesive Mixtures

The results described above and in the main article imply that a suspension of equal-sized positively and negatively polarizable particles can form connected self-assembly only if $N_p\beta_p \approx -N_n\beta_n$, where N_p and N_n are the number of positively and negatively polarizable particles, respectively. When the sizes of positively and negatively polarizable particles are not equal, this result generalizes to

$$V_p\beta_p \approx -V_n\beta_n \tag{2.2}$$

Here V_p and V_n are the volumes of the positively and negatively polarizable particles, respectively. This condition is consistent with the experimental data, which shows that when $\beta_p \approx |\beta_n|$, the peak in the yield stress occurs when $V_p \approx V_n$.

2.4.5 Suspensions of Brownian Particles

Nanoparticle suspensions' behavior differs from that of suspensions with larger sized particles because nanoparticles are also subjected to Brownian forces, which cause them to move randomly in the fluid. This continues to be the case unless a sufficiently strong electric field is applied to arrest particles' motion relative to one another. The ratio of the electric and Brownian forces, given by the dimensionless parameter $P_7 = \frac{\sqrt{3\tau\pi a^3}\varepsilon_0\varepsilon_0\beta^2|E_0|^2}{8\xi\sqrt{\eta K_B T}}$, determines the relative importance of these two forces [80]. Here, a is the particle radius, η is the dynamic viscosity, τ is the time step used in the simulations, ξ is the magnitude of a Gaussian random parameter, K_B is the Boltzmann constant and T is the temperature in Kelvin. Particles self-assemble into patterns similar to those formed in micron-sized particles' suspensions when the dipolar forces are strong enough to overcome Brownian forces.

Figure 2.22 shows the DNS results for a mixture of positively and negatively polarizable nanoparticles. The radii of both positively and negatively polarizable particles are 100 nm, and the magnitudes of their CM factors is 0.05, i.e., $\beta_p = |\beta_n| = 0.05$. The initial arrangement of particles is assumed to be random. The figure shows that the mixtures self-assemble into a cohesive arrangement only when $P_7 > O(1.0)$. When $P_7 < 1$, particles do not tightly pack together because they continue to move around under Brownian forces' action. This is also the case for the mixtures in which particle sizes vary, provided $P_7 > O(1.0)$ for the smallest particles, i.e., the electric

field strength results in the dipolar forces that are large enough to arrest the smallest particles' motion.

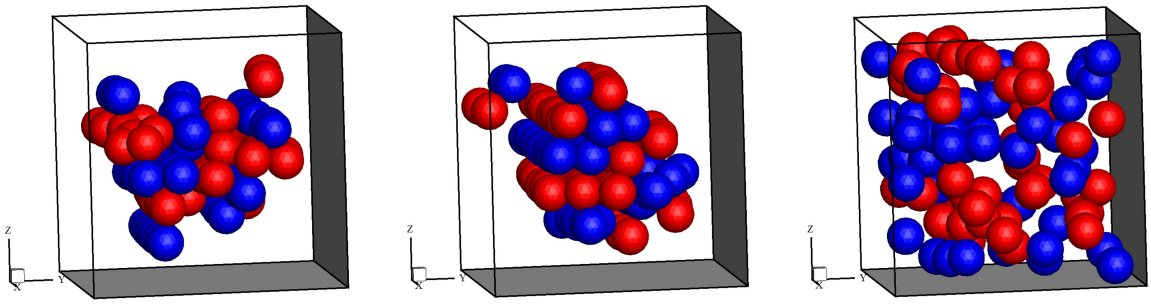

Figure 2.22 Steady-state arrangement of a mixture of positively and negatively polarized particles. 96 particles were initially arranged randomly and subjected to a uniform electric field in the x-direction. There are equal numbers of positively and negatively polarized particles, and their diameters and the magnitudes of the CM factors are equal. The electric field strength is varied to change parameter P7, which is 1.7 in (a), 0.034 in (b), and 0.00034 in (c).

CHAPTER 3

MAGNETIC FIELD-INDUCED SELF-ASSEMBLY OF DIAMAGNETIC AND FERROMAGNETIC PARTICLES IN MAGNETORHEOLOGICAL FLUID

When a magnetorheological (MR) fluid is subjected to a uniform external magnetic field, the suspended particles become magnetized and rearrange in chains and columns aligned parallel to the electric field direction, increasing the yield stress. However, if the MR fluid contains only positively or negatively magnetizable particles, these chains and columns repel each other, causing them to move apart. Consequently, the particle distribution gets fragmented into chains and columns. This behavior of MR fluids is analogous to that of electrorheological (ER) fluids containing only positively or only negatively polarizable particles. Also, just as for the ER fluids, the fragmentation problem is overcome when the MR fluid is formed using a suitable mixture of positively and negatively magnetizable particles. In this work, we study the yield stress of the MR fluids formed by mixing positively and negatively magnetizable particles. The MR fluids were prepared by mixing ferromagnetic and diamagnetic particles in a ferrofluid. The former particles are positively magnetized, and the latter negatively. In our experiments, the volume fraction of the positively magnetized particles in the suspensions was varied while holding the total volume fraction of particles constant. The results show that there is an optimal volume fraction of positively magnetized particles for which the yield stress is maximum. Also, as for the ER fluids, when the particle volume fractions are near the optimal values, they come together to form a cohesive suspension, which increases the yield stress.

3.1 Introduction

When a magnetic field is applied to a magnetorheological (MR) fluid, a suspension of micron-sized iron particles in a carrier liquid, its particles rearrange to form chain-like structures. This happens because the particles acquire magnetic moments, causing particles to rearrange relative to one another and get aligned along the applied field direction. The rearrangement of the particles changes the liquid's free-flowing nature to a semi-solid one [81], and its rheological properties are also modified, e.g., the viscosity is increased [82, 83]. Particle chain formation in a magnetic field occurs due to the magnetic dipole-dipole interactions.

In recent years, magnetic dipole-dipole interactions have been extensively studied, including the effect of concentration of magnetite particles, core-shell structure, particle morphology and aggregation, and fluid stability [84, 85, 86, 87, 88]. The problem in applying a magnetic field to an MR fluid containing only one type of particles, i.e., either positively or negatively magnetized particles, is that the interaction force between particles is attractive only when the line joining the particle centers is parallel to the magnetic field direction. The force is repulsive when they are aligned in a perpendicular direction to the field. Therefore, particles do not come together in both the parallel and perpendicular plane of the applied field. This causes the particle distribution to get fragmented into chains and columns with gaps between the particles. Thus, the particle chains cannot resist shear collectively, and the yield stress is limited. This behavior is analogous to that of the electrorheological (ER) fluids containing either positively or negatively polarized particles, which is discussed in Chapter 2.

Several studies have been conducted in which different combinations of particles were used for preparing MR fluids and utilizing a ferrofluid (FF) as the suspending liquid. For example, Erb et al. illustrated the magnetic assembly of a mixture of paramagnetic and nonmagnetic particles in FF, which showed various structures

such as "Saturn rings," "flowers," "poles," and "two-tone" arrangements [67]. Ray et al. used paramagnetic and diamagnetic particles, which showed colloidal flowers and strings [89]. Similarly, Lopez-Lopez et al. used diamagnetic and ferromagnetic particles as the colloidal suspension in FF and studied the rheological behavior of an Inverse Magnetorheological Fluid [90]. Susan-Resiga et al. formulated different samples of ferrofluid-based magnetorheological fluids while varying the nanometer-sized and micrometer-sized iron particles' volume fractions and the total volume fractions [91] of particles. They concluded that the dynamic and static yield stresses increase with iron particle volume fraction and the total volume fraction of particles. Magnetic susceptibility of particles and the suspending liquid influence the MR suspension's rheological properties and determined the self-assembled patterns. An extremely bidisperse MR fluid presents an enhanced viscosity with increasing particle concentration, and particles show repulsion at closer distances [31, 32, 92]. A mixture of ferromagnetic (FM) and diamagnetic (DM) particles suspended in a ferrofluid for forming inverse magnetorheological fluid shows clusters of FM particles around single particle chains of larger sized DM particles and shows fragmentation of particles into chains and columns. The fact that these field-induced columns do not combine to form a connected cluster, including when a surface pattern is used to guide their assembly [93], indicates that the forces among them are not attractive.

In this work, we experimentally investigated MR fluids' yield stress behavior formed by suspending mixtures of ferromagnetic and diamagnetic particles in ferrofluids (FF), which shows that the yield stress is maximum when the volume fraction of ferromagnetic particles is around sixty percent. This is because of the chains' attraction in both parallel and perpendicular directions to the applied magnetic field for this critical volume fraction ratio of both types of particles. Therefore, particles self-assemble to form a cohesive structure which increases the yield stress of the suspension. It is possible to induce positive polarization in one

type of particles and negative polarization in the second type by selecting a liquid medium with a suitable magnetic susceptibility.

Experimental results show an increase in the mixtures' yield stress, indicating that the particles form a cohesive structure. We also found that MR fluids' rheological response depends on various parameters, including the particles' concentration, magnetic susceptibility of the suspending liquid, and the applied magnetic field intensity.

The MR fluids' behavior differs from that of the ER fluids because the negative magnetization of particles in MR fluids is much weaker than of the positively polarized particles. This is because the magnetic susceptibility of ferrofluids is much smaller than that of iron particles.

3.1.1 Mechanisms of Interaction of Particles

The mechanism that determines particles' distribution upon application of a magnetic field is analogous to that in an electrorheological fluid as discussed in Chapter 2. Particles attract each other when they are aligned parallel to the field direction, and they repel when aligned in a perpendicular direction to the field due to dipole-dipole interaction.

The applied magnetic field causes particles to acquire magnetic moments, due to which they get aligned along the field direction. The interaction between particles causes the formation of alternating bands of ferromagnetic and diamagnetic particle chains in the MR suspension. In an external magnetic field $\mathbf{H}_0$, the magnetic moment acquired by a particle of relative permeability μ_p is given by:

$$\mathbf{m} = 3\mu_f \beta_p V \mathbf{H_0} = \chi V \mathbf{H}_0 \tag{3.1}$$

where V is the particle volume, μ_f represents the relative magnetic permeability of the fluid medium, $\beta_p = \frac{\mu_p - \mu_f}{\mu_p + 2\mu_f}$ is the magnetic Clausius-Mossotti factor or the magnetic contrast factor, and χ is the particle's magnetic susceptibility. For ferrofluids, $\mu_f > 1$, which can be varied by varying the particle concentration [67]. For diamagnetic particles, $\mu_p \approx 1$, and so $\beta < 0$. However, for ferromagnetic particles $\mu_p >> 1$. In our experiments, β values for diamagnetic particles were in the range of -0.26 to -0.31, and that of ferromagnetic particles were 0.997 to 0.998 for suspensions containing EFH1 and EFH3 ferrofluids, respectively. Therefore, the diamagnetic particles have their magnetic moments in the opposite direction of the magnetic field, and the ferromagnetic particles acquire magnetic moments in the direction of the field. The dipole-dipole interaction force acting on a particle i due to another particle j is given by:

$$\mathbf{F}_{ij} = \frac{\mu_0}{4\pi\mu_f}\left\{3\frac{\mathbf{m}_i\mathbf{m}_j}{r^5}\mathbf{r} + \frac{3}{r^5}[(\mathbf{m}_i.\mathbf{r})\mathbf{m}_j + (\mathbf{m}_j.\mathbf{r})\mathbf{m}_i] - \frac{15}{r^7}(\mathbf{m}_i.\mathbf{r})(\mathbf{m}_j.\mathbf{r})\mathbf{r}\right\} \qquad (3.2)$$

Here, $\mathbf{m}_i$ and $\mathbf{m}_j$ are the magnetic moments of particles i and j, respectively, μ_0 is the magnetic permeability of vacuum and r is a vector connecting the center of two adjacent particles. When adjacent particles are of the same type, their magnetic moments are equal and are aligned in the field's direction. When the line joining the particle centers is parallel to the magnetic field direction, the interaction force is attractive and becomes repulsive when it is perpendicular to the field. If the particles are aligned at an intermediate angle, they experience a magnetic torque that rotates them to align along the field direction. Consequently, neighboring particles of the same type come together and form close-packed chains. However, if two particles are of different types, the force is repulsive when the line joining the particle centers is parallel to the field direction. The force will be attractive only when the line joining the centers is perpendicular to the field.

3.1.2 Experimental

(a) Sample preparation: The MR fluid suspensions were prepared by mixing micron-sized ferromagnetic and diamagnetic particles in ferrofluids where they become positively and negatively magnetized, respectively. Iron particles (1-3 μm, Alfa Aesar) and glass particles (3-6 μm, Cospheric) were selected as ferromagnetic and diamagnetic particles, respectively. We used two ferrofluids with different magnetic susceptibilities and magnetic particle concentrations- EFH1 (Magnetic particle concentration: 7.9% vol., Educational Innovations and Ferrotec) and EFH3 (Magnetic particle concentration: 11.8% vol., Ferrotec). In our experiments, the total volume fraction of particles in the suspension was held constant while the volume fractions of positively (iron) and negatively (glass) magnetized particles were varied. For EFH1 as the suspending liquid, the β values for the diamagnetic and ferromagnetic particles are -0.26 and 0.998, respectively, and for EFH3 as the suspending liquid, the β values for the diamagnetic and ferromagnetic particles are -0.31 and 0.997, respectively.

The MR fluids were formed by first thoroughly mixing iron and glass particles and then adding the particle mixture to the ferrofluid. The mixture was added to the suspending fluid in small portions and stirred continuously, which ensured a homogeneous suspension. The total volume fraction of particles was selected to be in the range of 30%-53% of the total MR suspensions. We experimentally investigated the prepared MR fluids' behavior as a function of the total particle volume fraction, the relative particle fractions, and the magnetic field intensity.

(b) Yield stress measurement: To quantify the changes in the microstructures of a MR fluid, we measured its yield stress upon the application of an external magnetic field. A vane spindle rheometer (YR-1 Yield Stress Rheometer, Brookfield Engineering) with an accuracy of $\pm 2\%$ was used. The experimental setup is shown in Figure 3.1. The MR fluid was placed in a 69mm long cylindrical device with

a diameter of 32mm, which was then placed in a hollow 3-D printed square box, 42mm long, 50mm deep, and 5mm thick, to ensure that the magnitude of the applied magnetic field was uniform. Two square-shaped ceramic magnets (McMaster-Carr, USA, 5738K67) having a length of 101.6 mm and the thickness of 6.35 mm and two disc-shaped magnets (McMaster-Carr, USA, 58605K77) having a diameter of 12.7 mm and the thickness of 6.35 mm with a maximum pulling capacity of 7 pounds (lbs.) each were placed touching the device such that the magnetic field lines were perpendicular to the vane spindle of the rheometer. Two adjoined 3-D printed separators having a thickness of 12.7 mm were placed between the box and the magnets to vary the magnetic field intensity. The magnetic field intensity was 35 mT, 23 mT, or 16 mT at the center of the device containing the MR fluid suspension.

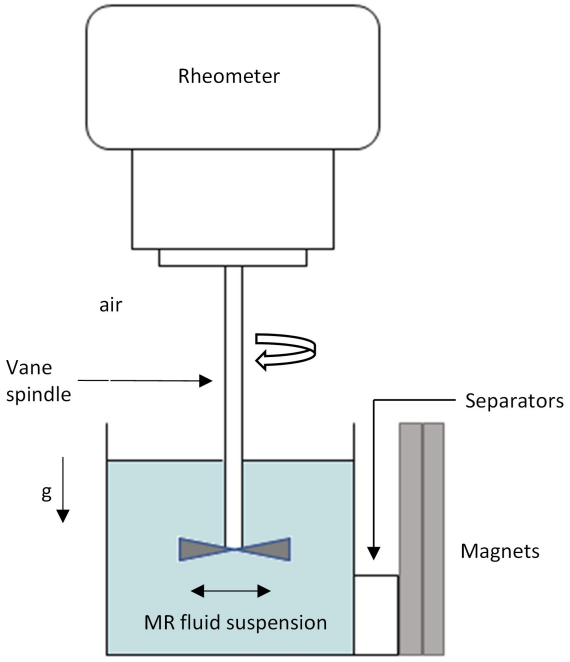

Figure 3.1 Schematic of the experimental setup used to measure yield stress. Magnets are placed on the sidewalls of the device containing the MR suspension. Values are recorded when the vane spindle rotates.

The magnetic field strength was measured using a 3-axis magnetic field sensor (Go Direct, Vernier Software and Technology). The field strength was in the range of 23-35 mT, as shown in Figures 3.2-3.4.

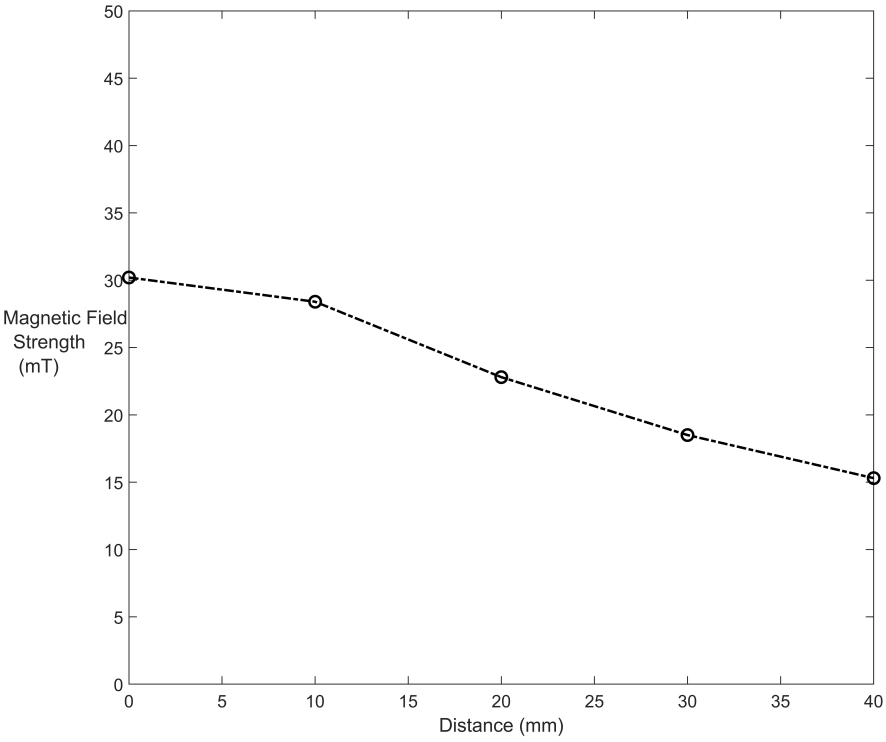

Figure 3.2 Magnetic field strength (mT) as a function of the distance. The field lines were perpendicular to the surface, and the distance was varied from 0 mm to 40 mm (left to right) when two square-shaped magnets were placed together on one side of the device. The magnetic field strength in the middle was 23 mT.

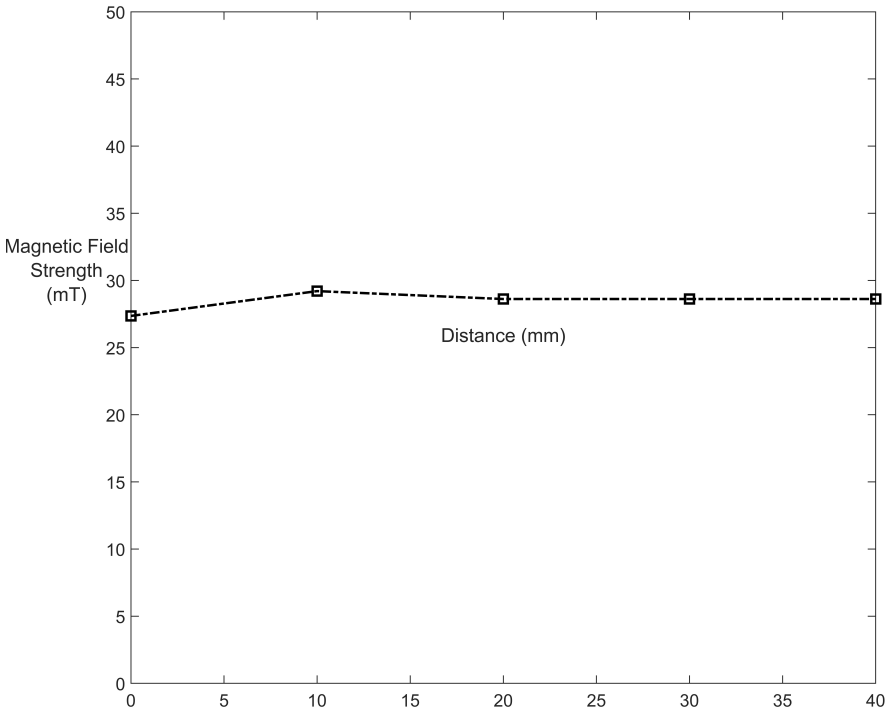

Figure 3.3 Magnetic field strength (mT) as a function of the distance. The field lines were perpendicular to the surface, and the distance was varied from 0 mm to 40 mm (left to right) between two square-shaped magnets placed on each side of the device. The magnetic field strength in the middle was 28 mT.

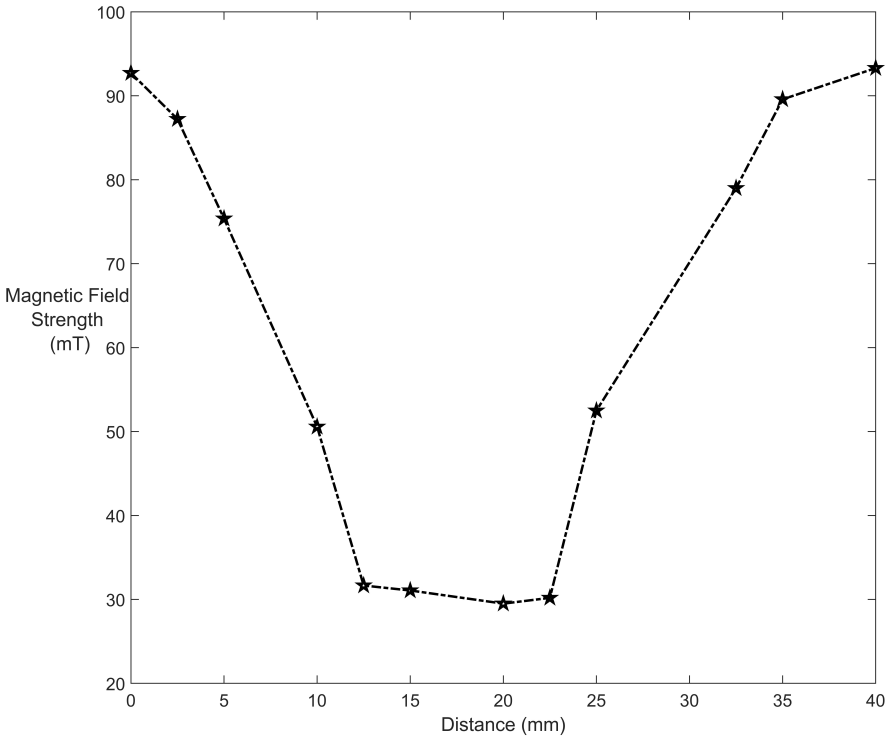

Figure 3.4 Magnetic field strength (mT) as a function of the distance. The field lines were perpendicular to the surface, and the distance was varied from 0 mm to 40 mm (left to right) between two circular-shaped magnets placed together on one side of the device. The magnetic field strength in the middle was 35 mT.

The rheological measurements were conducted for three different intensities of the magnetic field. The test parameters were as follows: (i) Spindle 73: medium vane spindle; (ii) Primary Immersion mark: the vane spindle mark was matched up to the fluid boundary; (iii) 0 rpm pre-shear speed: the shearing of the sample before measuring its yield properties; we skipped this step since the fluid was already mixed for twenty minutes; (iv) 0.5 rpm zero-speed: the rheometer rotates the spindle in the appropriate direction until 0% torque is achieved (v) 2.5 rpm running speed: the motor speed at which the material is tested; (vi) 100% Torque Reduction: this parameter causes the test to stop as soon as there are no torque increases; (vii) 2.32% Base Increment Calibration: base increment is the amount of time in milliseconds between data points used for taking torque readings. Next, the vane spindle was immersed in the suspensions for measuring yield stress. Without changing the parameters, ten consecutive measurements were performed to ensure reproducibility of results. A similar procedure was followed with all the MR fluids having different particle concentrations.

3.1.3 Results and Discussion

This section discusses the measured yield stress results as a function of varying volume fraction of positively magnetized (iron) particles while holding the total volume fraction of particles constant. The measurements were performed for three different magnetic field intensities. For this purpose, three device configurations were used as shown in Table 3.1.

Table 3.1 Device Configurations Showing Different Magnetic Field Strengths

Configuration	**Description**	**Magnetic field strength (in mT)**
1	Circular magnets on each side	35
2	Two square-shaped magnets on one side	23
3	Two square-shaped magnets on one side with separators	16

(a) Role of particles' concentration and applied magnetic field intensity: In this subsection, we present yield stress results in which the concentration of particles and the magnetic field intensity are varied. The aim of this study is to model the role of these parameters.

Figures 3.6-3.12 show the yield stress as a function of the volume fraction of iron particles for five MR suspensions formed by mixing iron and glass particles in ferrofluids. Here the percent volume fractions is defined to be $\frac{volume\ of\ iron\ particles}{total\ volume\ of\ particles} \times 100$. The volume fraction at which the peak yield stress occurred varied with the magnetic field intensity. Figure 3.5 shows the results for the MR suspensions formed using the ferrofluid EFH1 with the total particle volume fractions of 0.2 and 0.3. For a magnetic field strength of 35 mT, we found that the yield stress reached the peak value at 50% volume fraction of iron particles when the total particle volume fraction was 0.2. The yield stress for the total volume fraction of 0.3 increased with the increasing volume fraction of iron particles. In both cases, peaks were not prominent. The yield stress for 100% iron was higher for 0.3 than 0.2. This behavior shows that an increase in the total particle concentration enhances the yield stress.

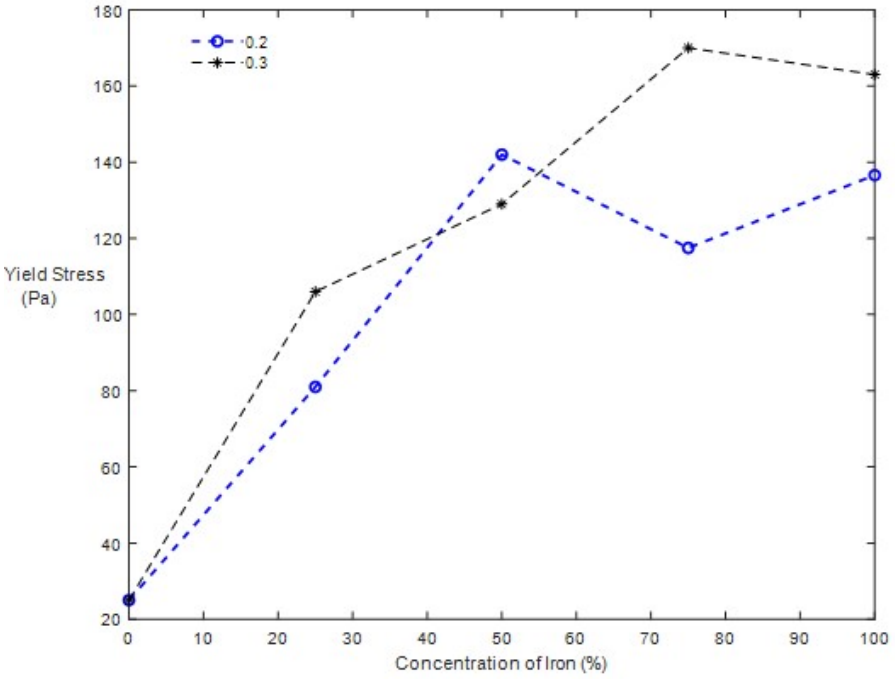

Figure 3.5 Yield stress versus volume fraction of iron particles for EFH1 containing a mixture of iron and glass particles under the application of a magnetic field of intensity 35 mT. The total volume fraction of particles was kept constant at 0.2 or 0.3 while the concentration of iron particles was increased from 0 to 100%. The yield stress was larger for 0.3.

In Figure 3.6, the yield stress of the above MR fluid for the total particle volume fraction of 0.3 is shown. For a magnetic field strength of 23 mT, the yield stress increased with an increase in the volume fraction of iron particles, and after reaching a maximum value, it decreased. This indicates that there are critical volume fractions of both types of particles for which the yield stress is maximum. A sharp peak of 303 Pa was observed at 75% iron. Therefore, applying a magnetic field strength of 23 mT was selected for conducting additional experimental studies because an intermediate peak was observed.

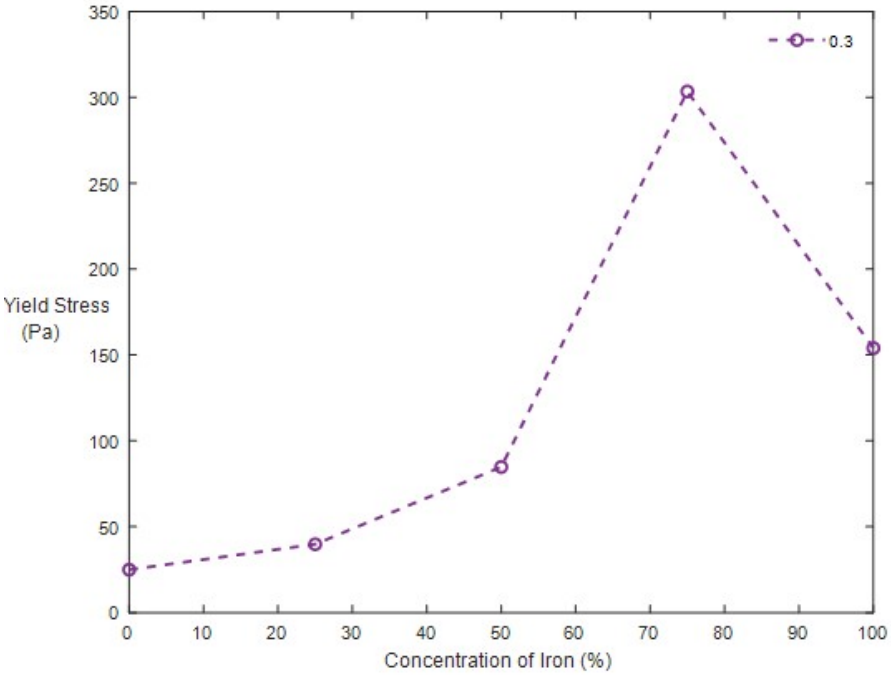

Figure 3.6 Yield stress versus volume fraction of iron particles for EFH1 containing a mixture of iron and glass particles under the application of a magnetic field of intensity 23 mT. The total volume fraction of particles was kept constant at 0.3. The yield stress was maximum for 75% volume fraction of iron particles.

In Figure 3.7, the performance of the MR suspension with EFH1 as the suspending liquid is shown, for the total particle volume fractions of 0.3 and 0.5 for a magnetic field strength of 16 mT. A curve was observed for 0.3, with a maximum value at 100% iron. When the total particle volume fraction was increased to 0.5, the peak was found at the 75% volume fraction of iron particles.

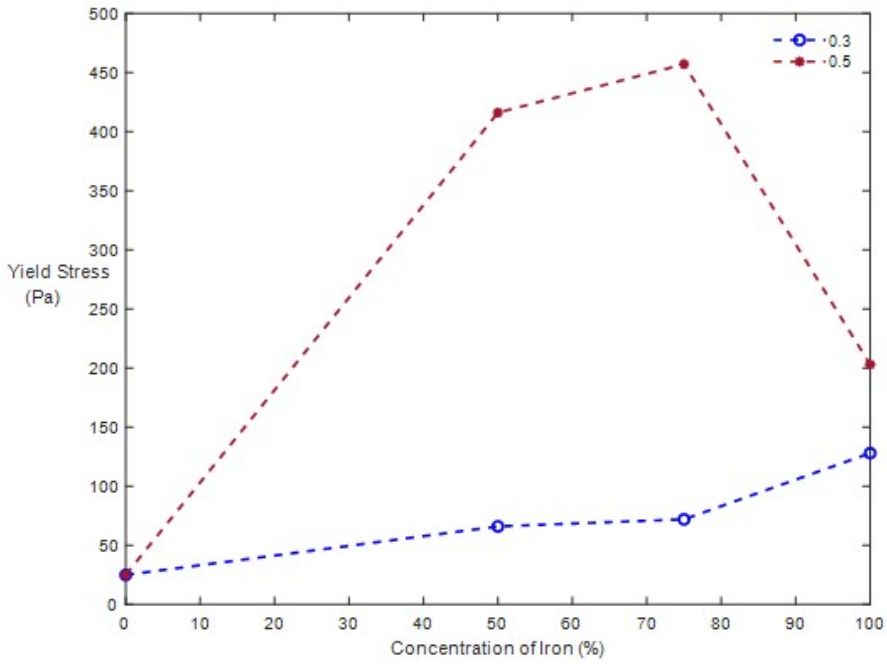

Figure 3.7 Yield stress versus volume fraction of iron particles for EFH1 containing a mixture of iron and glass particles under the application of a magnetic field of intensity 16 mT. The total volume fraction of particles was kept constant at 0.3 and 0.5. The yield stress had a peak of around 75% iron for a total volume fraction of 0.5.

The measurements were repeated for an MR suspension with EFH1 (Ferrotec) as the suspending liquid and the results were analyzed for a magnetic field strength of 23 mT and 16 mT. The total particle volume fractions of 0.35, 0.4, 0.5 and 0.53 were considered (Figures 3.8 and 3.9, respectively). In both the figures, a curve was observed for 0.35 without a major peak. A sharp peak was emerged when the total particle concentration was increased. For example, both 0.4 and 0.5 cases had a

greater yield stress value for the 60% volume fraction of iron particles. For the total particle volume fraction of 0.53, the curve plateaued as the maximum limit of the Rheometer reached. For a magnetic field strength of 23 mT, the yield stress was larger than the maximum limit. A comparison of Figures 3.8 and 3.9 shows greater peak values of 799 Pa for a magnetic field strength of 23 mT as compared to 650 Pa for a magnetic field strength of 16 mT, for a total particle volume fraction of 0.5.

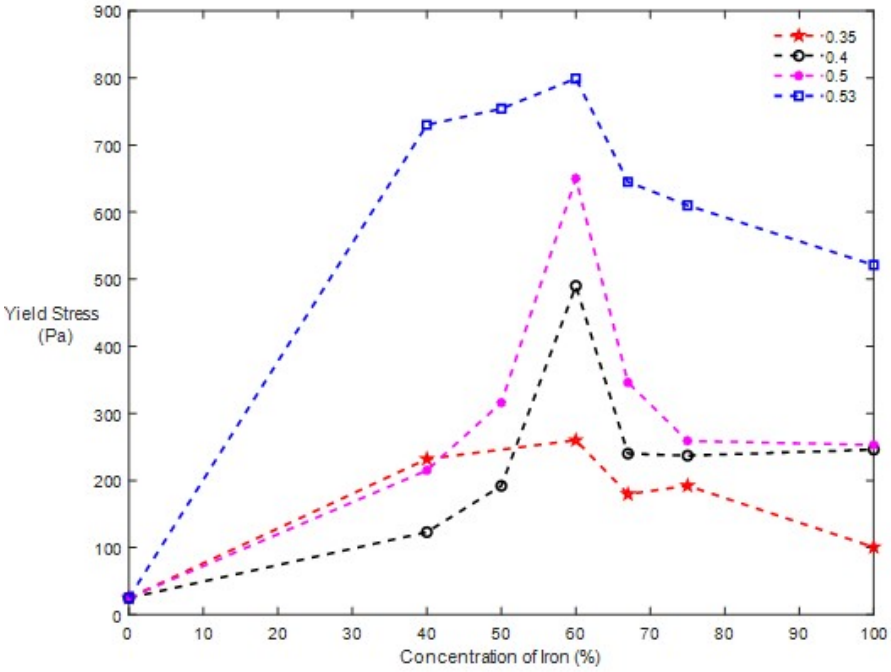

Figure 3.8 Yield stress versus volume fraction of iron particles for EFH1 (Ferrotec) containing a mixture of iron and glass particles under the application of a magnetic field of intensity 16 mT. The total volume fraction of particles was kept constant at 0.4, 0.5 and 0.53. The yield stress showed a sharp peak at 60% iron.

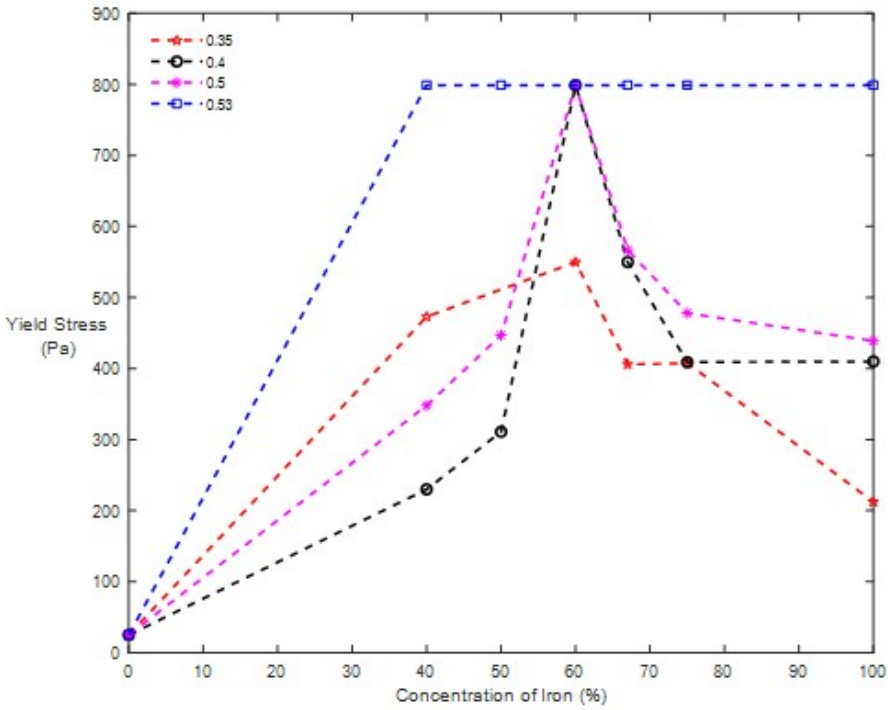

Figure 3.9 Yield stress versus volume fraction of iron particles for EFH1 (Ferrotec) containing a mixture of iron and glass particles under the application of a magnetic field of intensity 23 mT. The yield stress showed an enhanced peak at 60% iron.

We next present results for the MR fluids formed using the ferrofluid EFH3 (Ferrotec, USA), which contains a larger concentration of magnetic particles than EFH1. The yield stress curve was nearly flat at lower concentrations of iron as shown in Figures 3.10 and 3.11. When the applied magnetic field strength is 23 mT, the yield stress was constant for smaller particle concentrations. However, a sharp peak emerged for the 60% concentration of iron particles.

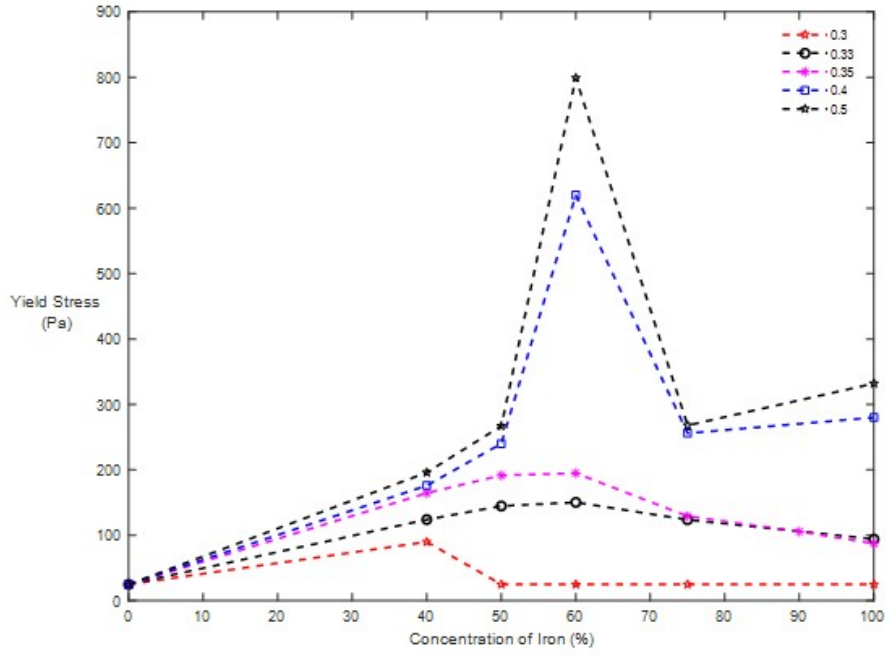

Figure 3.10 Yield stress versus volume fraction of iron particles for EFH3 (Ferrotec) containing a mixture of iron and glass particles under the application of a magnetic field of intensity 16 mT. The yield stress showed an enhanced peak at 60% iron.

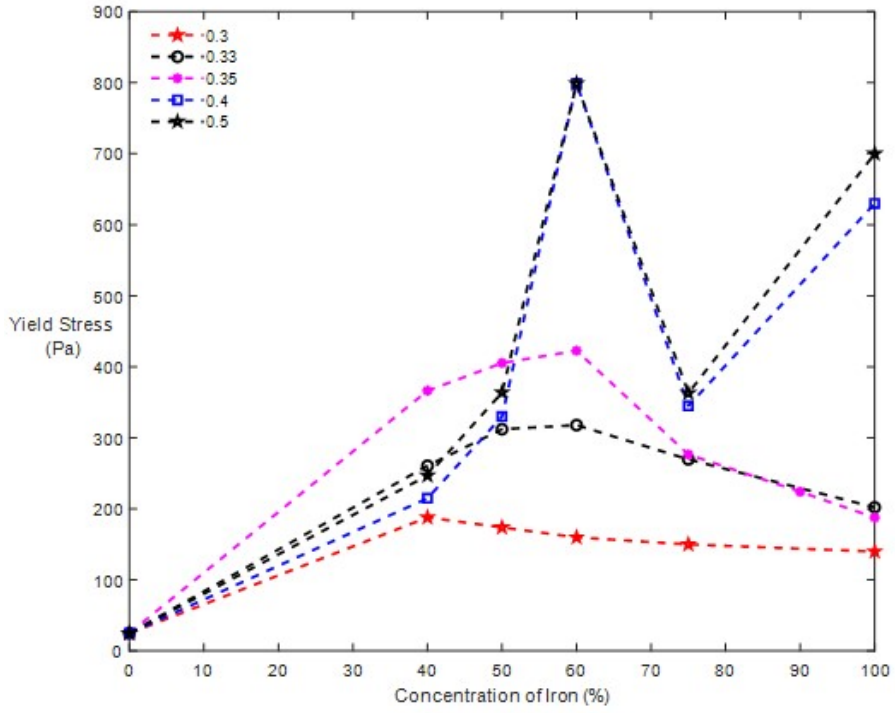

Figure 3.11 Yield stress versus volume fraction of iron particles for EFH-3 (Ferrotec) containing a mixture of iron and glass particles under the application of a magnetic field of intensity 23 mT. The yield stress showed an enhanced peak at 60% iron.

(b) Role of magnetic susceptibility of the suspending liquid: In this subsection, we present yield stress results in which the magnetic susceptibility of the suspending liquids is varied.

As previously discussed, magnetic dipole moments acquired by the particles depend on the susceptibility of the suspending liquid. By varying the susceptibility we change the positive and negative magnetization induced on the particles. This affects the formation of chain-like structures and hence, the yield stress. For example, comparison of Figures 3.9 and 3.11 shows distinct effects of ferrofluid properties of EFH1 and EFH3 respectively, on MR fluid behavior when a magnetic field is applied. For example, for a total particle volume fraction of 0.5 in Figure 3.8, yield stress reached its peak value of 650 Pa at 60% volume fraction of iron particles when EFH1 was used whereas a value of 800 Pa was reached when EFH3 was used. Therefore, EFH3 exhibits an enhanced MR effect owing to its higher magnetic susceptibility.

The experimental results show that the tendency of particles to self-assemble into clusters can be tuned on demand by applying a varying intensity of the magnetic field. The data also show that MR fluids' rheological response depends on various parameters, including the particles' concentration, magnetic susceptibilities of the suspending liquid, and the applied magnetic field intensity.

Listed below are the properties of particles and carrier liquid.

Table 3.2 Particle Properties

Name	**Particle Diameter (μm)**	**Relative Magnetic Permeability**	**Magnetic Susceptibility**
Alfa Aesar Iron	1-3	5000	200000
Cospheric Glass	3-6	1	-1×10^{-6}

Table 3.3 Suspending Fluid Properties

Name	Particle Diameter (nm)	Magnetic Particle Concentration (%vol)	Relative Magnetic Permeability at 20 Oe	Viscosity at 17 °C (cP)	Initial Magnetic Susceptibility	Density (g/cc)
EFH1	10	7.9	2.6	6	0.21	1.21
EFH3	10	11.8	3.4	<12	0.29	1.42

3.1.4 Conclusion

Magnetorheological suspensions prepared using a mixture of ferromagnetic and diamagnetic particles in ferrofluid as the suspending liquid, with different magnetic susceptibilities and magnetic particle concentration, exhibited different modifications in their rheological properties when a magnetic field was applied. The extent of connected structure formation was quantified by measuring the yield stress, which was investigated as a function of varying volume fractions of positively polarized particles while keeping the total particle volume fraction constant. Experimental results show that the yield stress increased with increasing volume fraction of positively polarized particles and decreased after reaching a maximum value. This indicates that there is an optimal volume fraction of particles for which the formation of a connected pattern is maximum. Also, the yield stress's peak value increased with an increase in the total particle volume fraction. We also found that the suspensions prepared using ferrofluid with greater magnetic susceptibility and magnetic particle concentration have greater changes in the yield stress.

CHAPTER 4

THIN FILMS WITH SELF-ASSEMBLED MONOLAYERS EMBEDDED ON THEIR SURFACES FOR SURFACE ENHANCED RAMAN SPECTROSCOPY APPLICATIONS

The current work presents a technique for the self-assembly of submicron-sized gold nanoparticles on a non-conducting film's surface. This was achieved by placing particles on a UV curable liquid's surface, applying an electric field normal to the surface to conduct self-assembly, enabling control of lattice spacing, and solidifying the monolayer once a suitable arrangement was formed. This method produces uniform surface patterns of self-assembled particle monolayers, and is rapid and cost-effective. The monolayers formed were used to prepare substrates for Surface-Enhanced Raman Scattering (SERS) applications. Gold particles' size and inter-particle spacing were considered for preparing substrates because they can enhance the SERS effect; namely, larger-sized particles exhibit an increase in wavelength with maximum absorbance, and a highly ordered arrangement with adjustable inter-particle spacing provides a larger area of enhancement, respectively. The experimental results show that the laboratory-built substrates are more efficient and deliver an enhanced SERS intensity compared to the commercial SERS substrates.

4.1 Introduction

In recent years, techniques employing self-assembly on liquid surfaces have drawn much attention because they can be used to form periodic monolayers of particles. One such technique of formation of particle monolayers is capillary-based self-assembly. Several research studies have been conducted to understand this process because it has a wide range of applications in technology, e.g., for forming novel micro and nanostructured materials, for stabilizing emulsions, and separation of ink and toner particles [94], and it helps in understanding particles' behavior in fluid-liquid

interfaces, e.g., pollination in hydrophilous plants [95], dispersion of proteins [96] and clustering of insect eggs [35, 36].

The phenomenon of naturally occurring capillary-induced self-assembly can be easily understood by a common example of clustering of cheerios on the surface of milk. The deformation of the interface by floating particles gives rise to lateral capillary forces, which cause them to cluster. However, capillary-induced monolayers formed this way have defects, lack long-range order, lattice spacing is not adjustable, and hierarchical structures are not possible. Moreover, lateral capillary forces are too small to move small micron and nano-sized particles to form self-assembled patterns.

We used a technique of applying an electric field to guide the particles' self-assembly process to overcome the aforementioned shortcomings. In this technique, an electric field is applied normal to the interface containing particles which results in the formation of self-assembled monolayers. The current work focuses on the self-assembly of submicron-sized gold nanoparticles (600 nm and 50-100 nm diameter) on a non-conducting film's surface. This was achieved by placing particles on a UV curable liquid's surface, applying an electric field normal to the surface to conduct self-assembly enabling control of lattice spacing, and solidifying the monolayer once a suitable arrangement was formed. As shown in Figure 4.1(a), monodisperse glass particles sprinkled on an air-oil interface self-assembled under capillary forces, but there were void gaps between them. When an electric field was applied normal to the interface (Figure 4.1(b)), particles moved away from each other and arranged themselves in patterns. Experimental results have shown that these electric field-induced monolayers have long-range order, are defect-free, and their lattice spacing is adjustable. The interparticle distance can also be varied by varying electric field strength. The assembled monolayers can be embedded on a thin films' surface to create a substrate for Surface-Enhanced Raman Scattering (SERS) technique.

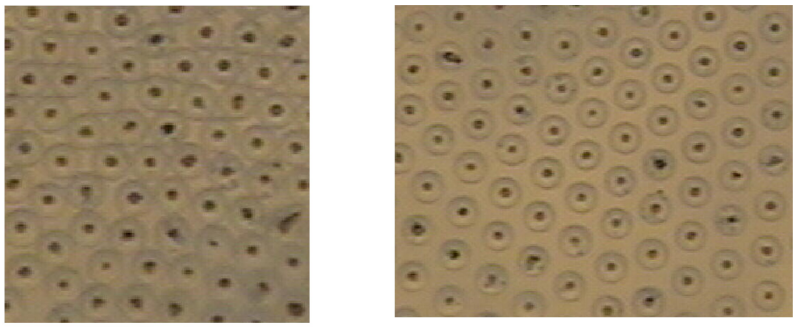

0 V (before using E) 5000 V

Figure 4.1 Substrates containing glass particles of radius 40.5 mm at the air-oil interface. (a) Particles self-assembled under the action of capillary forces when the electric field was 0 V. Notice that there are lot of void gaps as particles are physically touching each other. (b) Electric field-induced ordered monolayers are formed when an electric field of 5000 V was applied.

Surface-enhanced Raman Scattering (SERS) is a surface-sensitive technique that uses the concept of inelastic light scattering (see Figure 4.2) by molecules absorbed on rough metal surfaces activated by a laser source resulting in the enhancement of Raman scattering by factors of $10^{10} - 10^{15}$. As SERS helps in the structural detection of molecules, this technique has widespread applications in life sciences for cell and tissue-based analysis, quality control in the pharmaceutical industry, counterfeit detection, security purposes, including detection of explosives, forensics, food safety, biomolecular identification [97], single-molecule detection [98, 99], chemical, and bioanalytical sensing and imaging [100, 101]. The most commonly used metals for SERS technique are gold, silver, and copper. Gold and silver have been widely employed because of their unique physical properties such as air stability, biocompatibility, and optical properties for biomedical applications [102], while copper is more reactive.

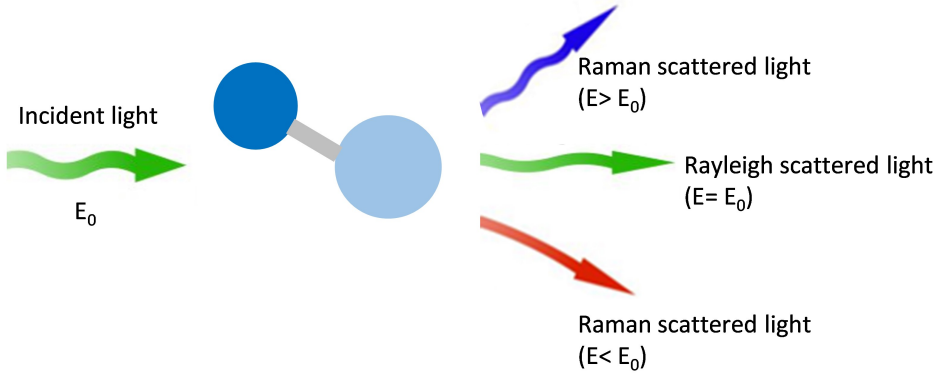

Figure 4.2 Types of scattering processes when light interacts with a molecule. Rayleigh scattered light has an energy equal to the incident light (elastic). Stokes and Anti-Stokes Raman scattering (inelastic) have energies greater than and less than the incident light, respectively.

The two main contributors to SERS are the electromagnetic and chemical enhancement mechanisms. However, the electromagnetic mechanism is found to be a major contributor to most SERS processes [103]. It occurs because of the interaction between laser radiation and electrons on a metal surface. When an incident light strikes a metal surface, delocalized electrons of the metal structure undergo oscillations (surface plasmons) and create a charge motion. This gives rise to an electromagnetic field outside the metal, as shown in Figure 4.3. When the incident light's frequency becomes equal to the oscillation frequency of free electrons in the metal, surface plasmon resonances (SPRs) occur. The SPRs, which are localized to a specific location called localized surface plasmon resonances (LSPRs), cause the energy of the incident light to get scattered or absorbed, which enhances the electromagnetic field. The field enhancement magnifies the intensity of incident light which excites the Raman modes of molecules. This excitation causes the Raman scattering signal to get increased which is further magnified by the metal surface. The total enhancement obtained is the electric field to the fourth power. The electromagnetic enhancement for SERS is estimated to reach factors of $10^{10} - 10^{11}$ [104].

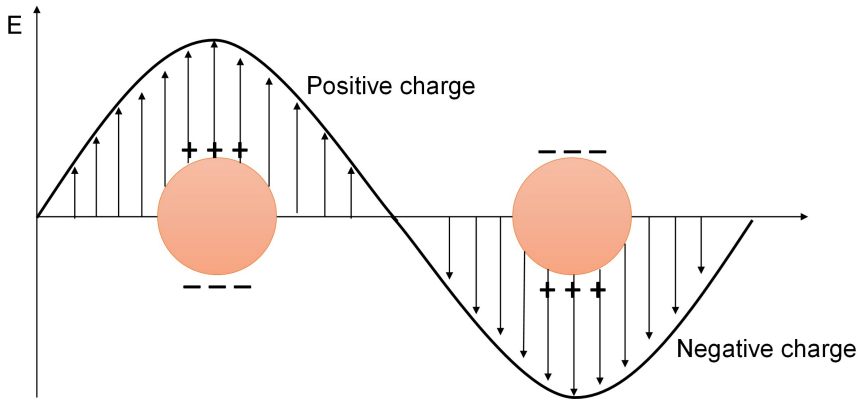

Figure 4.3 Localized surface plasmon resonances in electromagnetic enhancement mechanism.

The chemical enhancement mechanism involves charge transfer between adsorbed molecules and the metal surface [105]. This happens when the molecule adsorbs strongly on the metal's surface, leading to a change in its polarizability. The contribution of chemical enhancement to Raman Scattering is found to be 10^2. The total SERS enhancement factor is the product of electromagnetic and chemical enhancement mechanisms.

Since the phenomenon of enhanced Raman spectra of pyridine on roughened silver was discovered in 1974, researchers have investigated several factors that play a role in enhancing the Raman signal. Some of the factors are the selection of substrates and an appropriate excitation source. The enhancement was the largest in the few nanometers closest to the substrate surface as the maximum SERS enhancing region decreases with distance [103]. An excitation source is selected such that it enables efficient excitation of the plasmon resonance. The maximum signal is found when the laser wavelength is shifted to the blue of the plasmon resonance or the maximum peak wavelength red-shifts [106]. Local field hotspots [107] around adsorbed metal nanoparticles [108] and aggregated metallic nanoparticles were other contributing factors for SERS [109]. The strongest SERS activity occurs in nanoparticles of silver [110] and gold [111]. Different shapes of gold nanoparticles were also considered, such

as spheres, triangles, rods, hexagons, and stars for biomedical applications [100]. For example, Tiwari et al. used silver nano triangles to study the effect of curvature and estimated enhanced field strength around the vertices [112]. Tian et al. showed that gold nanosphere aggregations had a local field enhancement [113]. However, the enhancement exhibited by the substrates was not greater than for commercially available substrates.

Our aim is to prepare substrates with embedded particle monolayers which show an optimized SERS performance. For the preparation of such substrates, gold particles' size and inter-particle spacing were considered, which play an important role in obtaining a higher enhancement. This is because the wavelength with maximum absorbance increases with an increase in particle size20, and ordered particle arrangements with a high-density of sub-10 nm-interparticle spacing offer a larger surface area for adsorption of target analytes providing a large density of local field hotspots [114, 115]. For our experimental studies, substrates were prepared using spherical gold nanoparticles of sizes 600 nm (diameter) and 50-100 nm. An electric field was applied normal to the interface to obtain self-assembled particle monolayers. However, the present work will mainly focus on the performance of substrates containing monolayers of 600 nm gold particles. Figure 4.4 shows a thin film and monolayers of micron to nano-sized particles assembled under our technique with different arrangements. Our method produces SERS substrates with uniform surface patterns of metallic particles, which is rapid and cost-effective. Dr. Jenny Lockard's team conducted SERS measurements of the substrates at Rutgers University. The experimental results show that the substrates' performance depends on the particle concentration and the inter-particle distance. We also found that the laboratory-built substrates are more efficient and show an enhanced SERS intensity compared to the commercial SERS substrates.

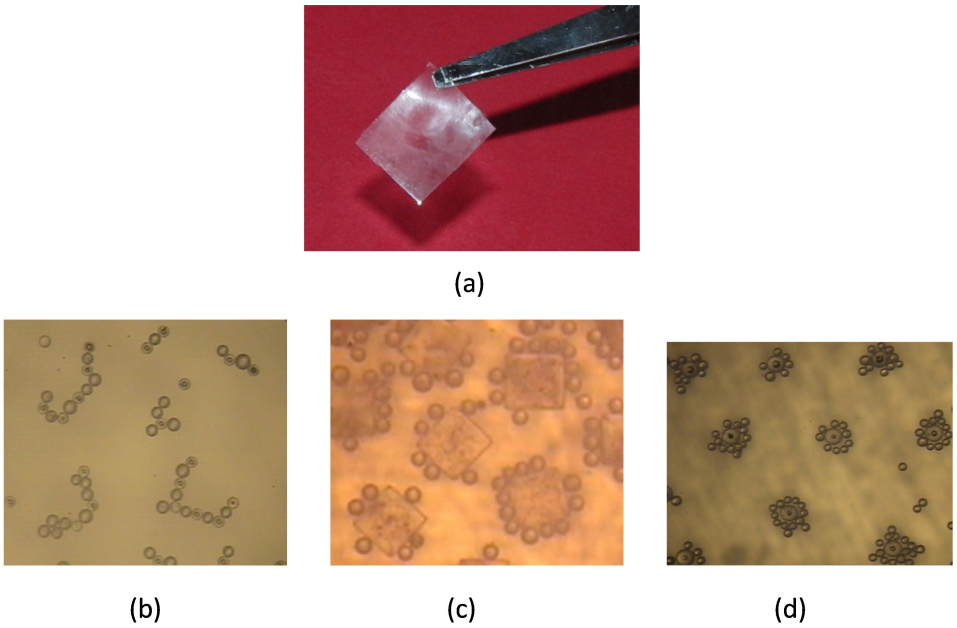

Figure 4.4 Films with customizable surface patterns. Self-assembled mono- and poly-dispersed dielectric and metallic particles arranged into a range of hierarchical patterns. These patterns of micron to nano-sized particles are then embedded on thin films. The spacing between the particles is adjustable.

4.2 Experimental

In this section, the procedure for preparing SERS substrates using electric field-induced self-assembly technique and SERS measurements is discussed.

(a) Sample Preparation: The first step in the sample preparation process is preparing substrates with embedded gold nanoparticles distributed uniformly throughout the surface. We used our technique to control the lattice spacing and solidified the monolayer once a suitable arrangement was formed. The experimental set-up consisted of a device containing two fluids, mounted with electrodes at the top and the bottom, as shown in Figure 4.5. The top electrode was transparent so that the monolayer could be seen using a microscope. A uniform electric field in the direction normal to the interface was obtained by applying a high voltage between the upper and lower electrodes. For this purpose, a variable frequency ac signal generator (BK Precision Model 4010A) was used along with a high voltage amplifier

(Trek Model 610E). The arrangement of particles was recorded using a digital camera connected to a Nikon Metallurgical microscope (MEC600). In our experiments, the top fluid was air, and the bottom liquid was a suspension of gold particles (600 nm and 50-100 nm) in UV adhesive (silicone). When an electric field was applied, the particles were trapped at the air-liquid interface. The substrate was made by freezing the UV adhesive to obtain a thin film embedded with trapped gold particles. In this study, we have prepared substrates with varying concentrations of gold nanoparticles (600 nm diameter).

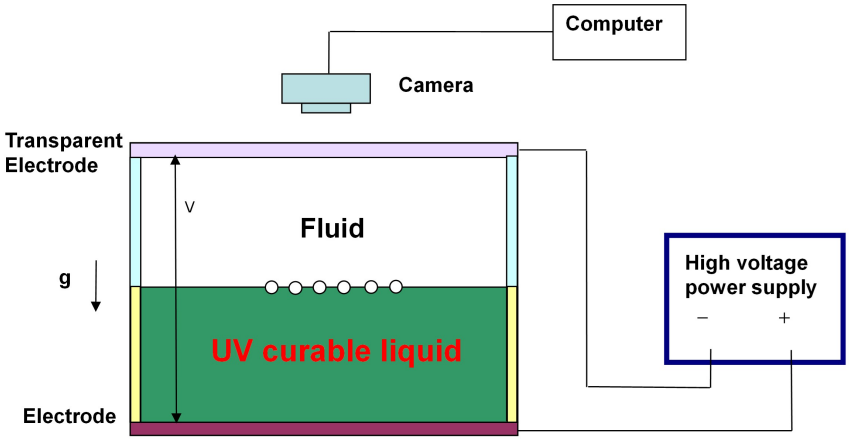

Figure 4.5 Experimental set-up.

The substrates embedded with gold nanoparticles' monolayers need to be prepared before SERS measurements can be conducted. This is done by adding an analyte to the particles, which gets adsorbed on the particles' surfaces (see Figure 4.6). Analytes are important as SERS enhancement is dependent on the number of molecules getting adsorbed on the substrate surface. In our experiments, DTNB (Ellman's Reagent or 5,5-dithio-bis-(2-nitrobenzoic acid)) was used as an analyte. Samples for SERS measurements were prepared by first adding the analyte, DTNB (Sigma Aldridge), to the substrate's surface. For this purpose, the samples were soaked in a 20 mM DTNB solution of methanol for 24 hours at room temperature and then washed them with methanol three times to remove excess unreacted DTNB.

Then the samples were dried in the open air to get the prepared substrates ready for SERS measurements.

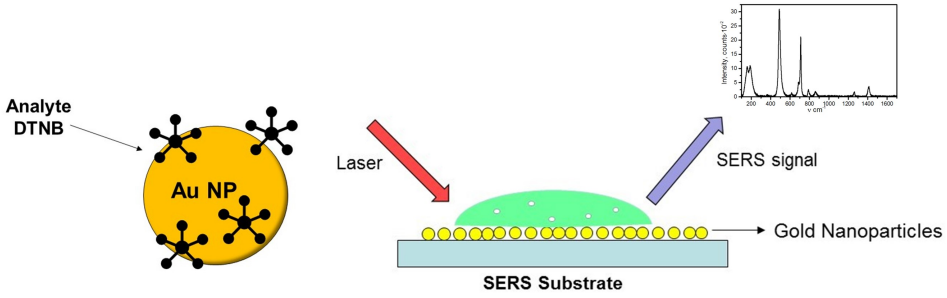

Figure 4.6 SERS Technique. (a) Molecules of the analyte getting adsorbed on the surface of gold nanoparticles. (b) Detailed SERS Technique.

(b) SERS Measurement: For measuring SERS, high-intensity laser radiation with wavelengths in either the visible or near-infrared regions is passed through the SERS substrates. The laser source excites the plasmon resonance, and SERS signals are generated, as shown in Figure 4.6(b). A filter is used to absorb or reflect any Rayleigh scattering allowing Raman signal to get transmitted. A spectrograph and a detector are then used to image Raman spectra across a wide spectral region shown in Figure 4.7.

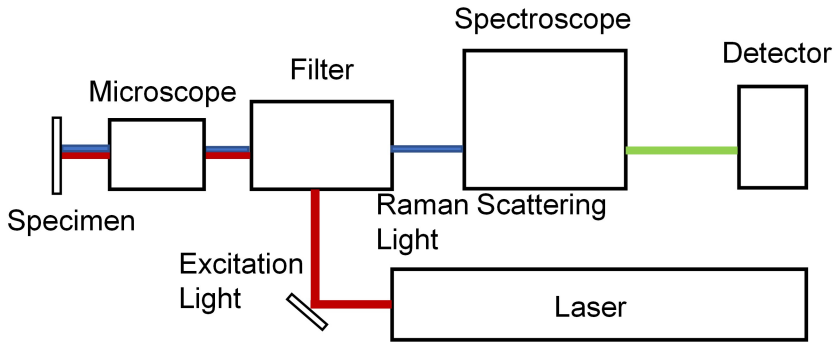

Figure 4.7 Raman Microscope components.

In our experiments, Raman spectra were collected at room temperature using a 785 nm single-frequency diode-pumped solid-state laser (Spectra-Physics) with ∼8 mW power, a triple monochromator, and a 1340×100-pixel liquid nitrogen-cooled

CCD detector (Princeton Instruments). Samples were spun during data acquisition and sample alignment to minimize photo- and thermal damage due to exposure to the laser light. SERS signals collected by the detector were used to observe aggregated particles by comparing the location of the maximum peak wavelength in the UV-Vis spectra.

4.3 Results and Discussion

In this section, we discuss our experiments' results to show self-assembly of gold nanoparticles under the application of an electric field and evaluate the SERS performance of thin films embedded with electric field-induced self-assembled monolayers of gold particles on their surfaces.

4.3.1 Directed Self-Assembly of Gold Nanoparticles

Figure 4.8(b) shows the formation of monolayers of gold nanoparticles when an electric field was applied. These defect-free monolayers are then used for obtaining SERS spectra.

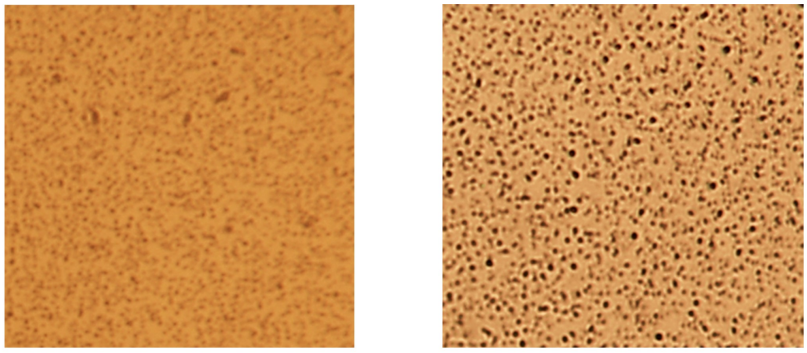

Figure 4.8 Gold nanoparticles of diameter 600 nm. (a) Particles self-assembled under the action of capillary forces when the electric field was 0 V. (b) Electric field-induced monolayers are formed when an electric field of 5000 V was applied.

4.3.2 SERS Studies of Silicone Substrates

Raman spectra were recorded to evaluate the degree of enhancement shown by our laboratory-built silicone-based substrates and compare their performance with commercially available substrates. For this purpose, we have recorded the performances shown by silicone substrates with embedded monolayers of varying concentrations of gold particles and by a commercial substrate.

The results are reported by a plot showing Raman radiation's intensity as a function of Raman shift calculated in wavenumbers. The horizontal axis of the Raman spectrum indicates the vibrational information of the adsorbed molecule and the vertical axis shows the intensity of activity. Figure 4.9 below shows the enhancement shown by a commercially available gold substrate (G1-102 Q-SERS Raman Enhancement Substrate). The black- and red-colored traces illustrate the SERS intensity by a pure gold substrate and when the substrate was treated with DTNB analyte, respectively. The pink-colored trace shows the pure SERS Signal, which indicates an enhancement. The pure SERS signal is the extracted SERS after subtraction of the spectrum of an untreated sample from the spectrum of the treated sample. The traces clearly show an enhancement of the Raman signal. This occurs because of the generation of local hotspots by the aggregated gold particles, which enhances the local electric field. Here, the peaks indicate enhanced vibrational modes.

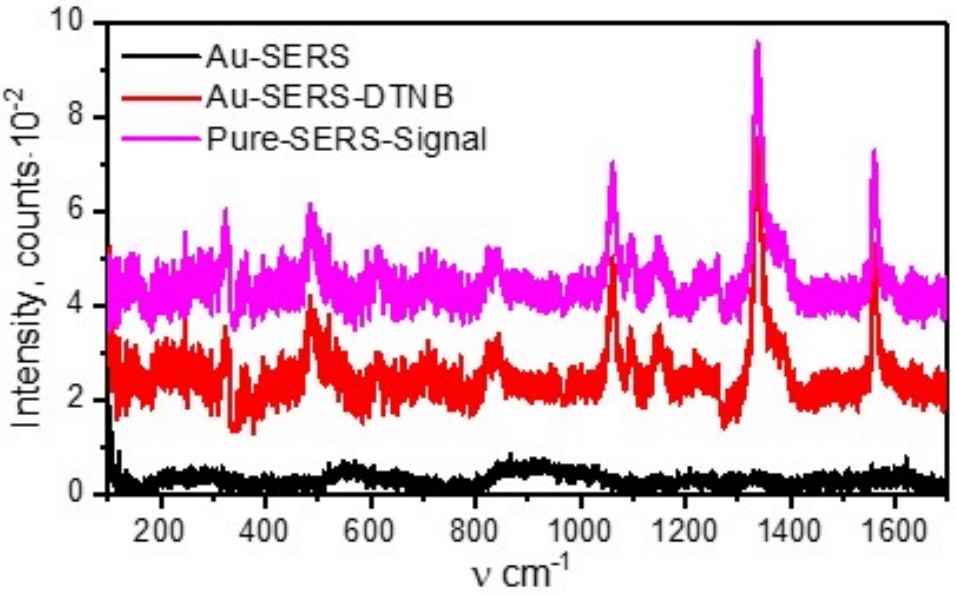

Figure 4.9 Intensity of Raman Radiation vs Raman Shift for commercial SERS substrate. Au-SERS – pure commercial Au substrate, Au-SERS-DTNB - commercial Au substrate treated with DTNB, pure-SERS-Signal - SERS extracted after subtraction of spectrum of untreated sample from spectrum of treated sample.

Figures 4.10 and 4.11 show the SERS intensity obtained from the prepared substrates with low and high concentrations of gold nanoparticles, respectively. We found that there was a difference in the intensity of the pure SERS signal obtained from the substrates. This behavior can be explained by the dependency of the SERS effect on the number of aggregated particles18. Here, the concentrated substrate's enhancement containing a greater number of gold particles and particle aggregations is stronger than the diluted one containing fewer particles.

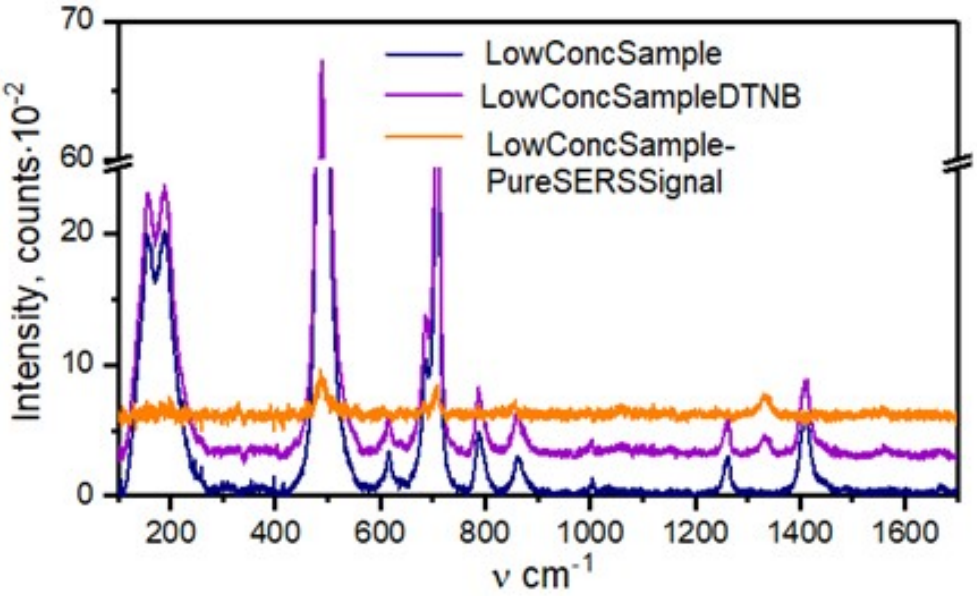

Figure 4.10 Intensity of Raman Radiation vs Raman Shift for a sample with a low concentration of gold nanoparticles. SilSERSDil – pure silicone-based substrate with low nanoparticle concentration, SilSERSDil -DTNB - silicone-based substrate treated with DTNB, pure-SERS-from SilSERSDil - SERS extracted after subtraction of spectrum of untreated sample from the spectrum of treated sample.

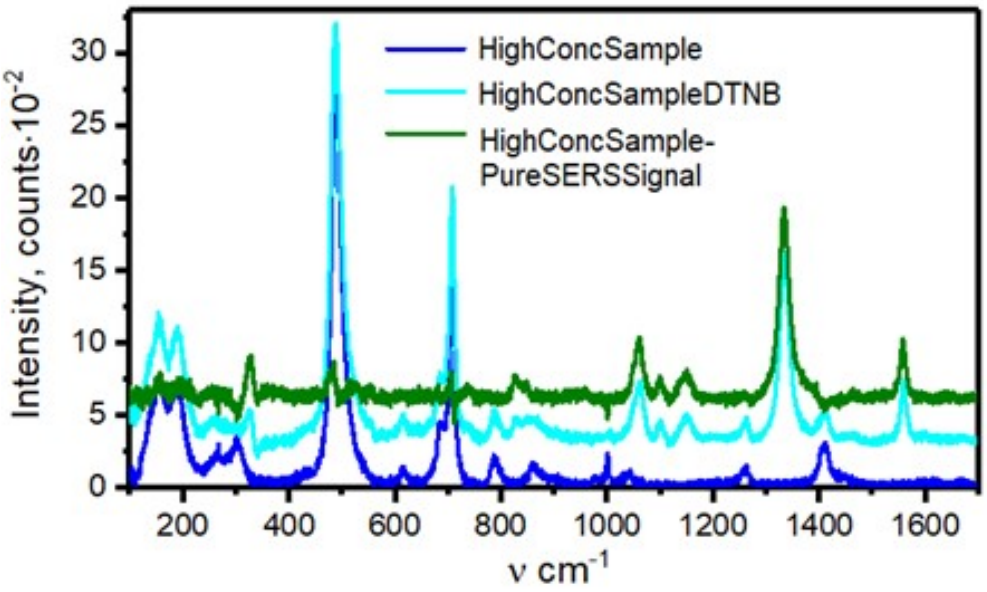

Figure 4.11 Intensity of Raman Radiation vs Raman Shift for a sample with a high concentration of gold nanoparticles. SilSERSConc – pure silicone-based substrate with high nanoparticle concentration, SilSERSConc -DTNB - silicone-based substrate treated with DTNB, pure-SERS-from SilSERSConc - SERS extracted after subtraction of spectrum of untreated sample from the spectrum of treated sample.

Figure 4.12 shows a comparison between the substrates containing a low and high concentration of gold nanoparticles and the commercially available gold substrate. The pink-colored trace illustrates the enhancement by a commercially available SERS substrate. The green and orange-colored traces show the prepared substrates' enhancement having a low and high concentration of gold nanoparticles, respectively. We found that the enhancement shown by our substrates is greater than the commercial substrate, which indicates a strong SERS effect.

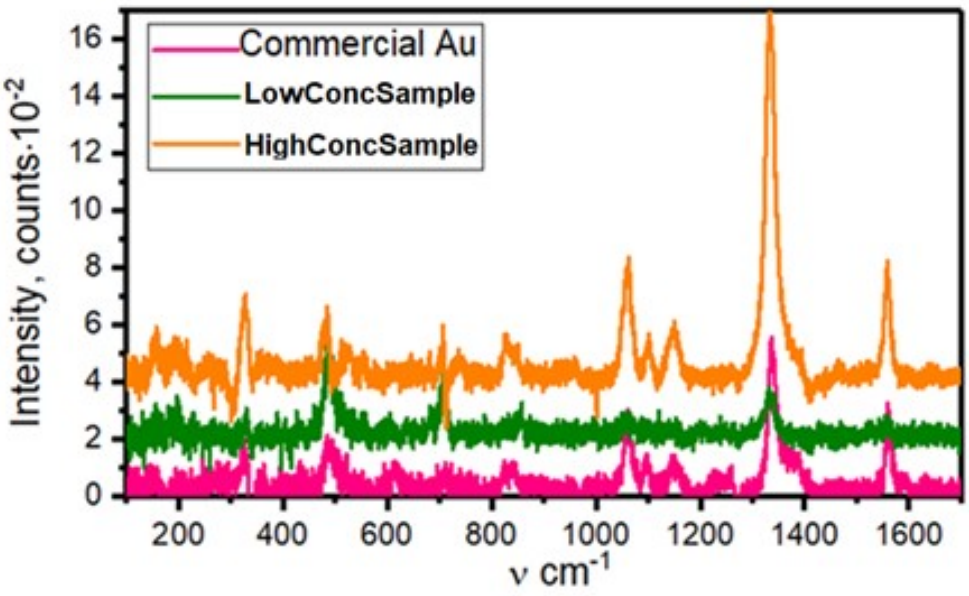

Figure 4.12 Intensity of Raman Radiation vs Raman Shift. SERS extracted from a) commercial substrate (Au),b) a silicone-based substrate with low nanoparticle concentration (Diluted), c) silicone-based substrate with high nanoparticle concentration (Concentrated).

4.3.3 Surface Area of the Substrates Covered with Gold Particles

We have also calculated the total area covered with gold nanoparticles for the highly concentrated gold nanoparticle substrate and the commercial substrate. Figures 4.13 and 4.14 show a comparison of our laboratory-built substrate's surface area and the commercially available ones, respectively. The Integrated Intensity technique was employed to estimate the enhancement correctly and to calculate the area covered

with particles. First, each peak was fitted with two pseudo-voigt functions (red and green dotted traces) in Origin 9.5. Once the fit was complete, reports were generated showing areas for those components, and their sum is the integrated intensity for the peak. The area was also calculated using the same technique. The relationship between the intensity measured on the detector and the integrated intensity is simply the surface area (in reciprocal space) of the spherical shell of scattering intensity. The blue-colored trace shows intensity for high gold concentration substrate, and the black-colored trace shows intensity for commercial SERS substrate. Results show that the peak intensity for our substrate is higher than the commercial one. We also found that the highly concentrated substrate is covered over nearly 46% of its surface area with gold particles and is ~6.75 times more efficient per gold particle than the commercial SERS substrate.

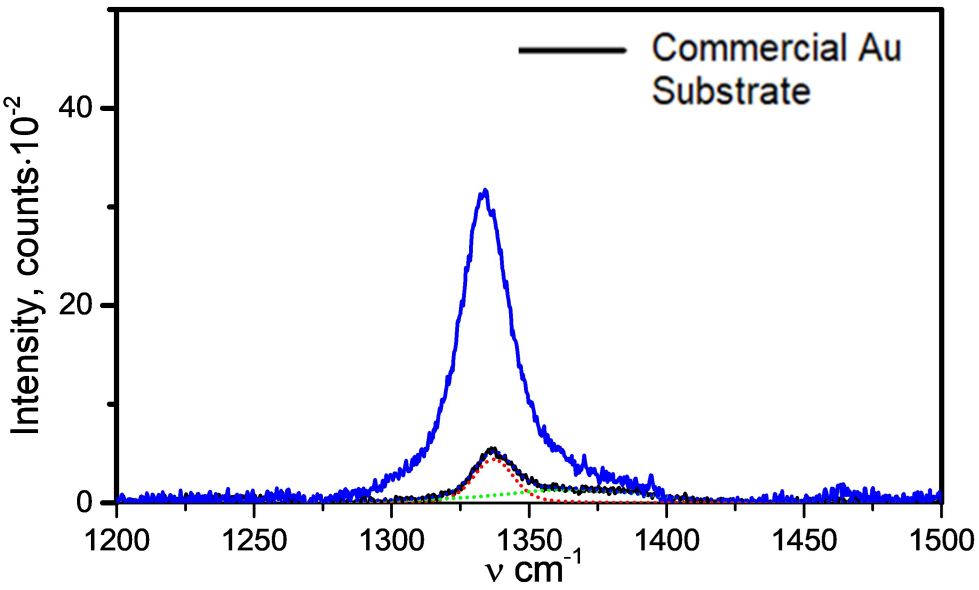

Figure 4.13 Surface area of gold nanoparticles on commercial gold substrate (blank line) Total area of the substrate covered with gold nanoparticles was 22301 (9189+13112).

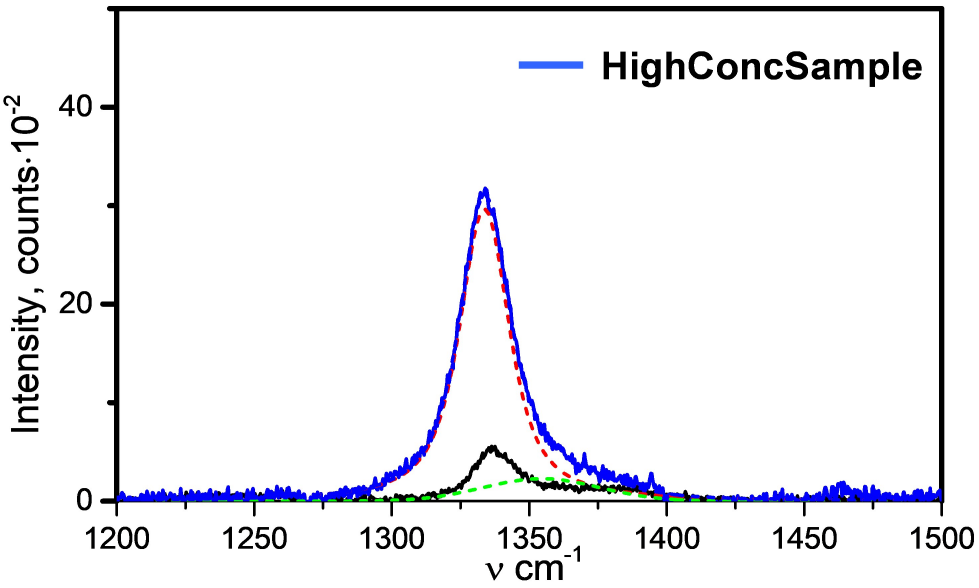

Figure 4.14 Surface area of gold nanoparticles on the prepared substrate having a high concentration of gold nanoparticles (blue line). Total area of the substrate covered with gold nanoparticles was 105538 (93397+12141).

4.4 Conclusion

Thin films with improved properties were prepared by curing UV-liquid-containing gold nanoparticle monolayers which were formed when an electric field was applied. The films were then used as substrates for Surface-Enhanced Raman Scattering applications. Experiment results show that the performance of the laboratory-built substrates containing varying concentrations of gold nanoparticles was better, indicating a stronger SERS effect than a commercial SERS substrate. Our substrates are 6.75 times more efficient per gold particle compared to the commercial ones. It is also found that 46% of the substrates' surface area was covered with gold particles which is another reason for the observed enhancement.

CHAPTER 5

DISSERTATION SUMMARY AND CONCLUSION

This dissertation explores the mechanisms that drive self-assembly in binary mixtures of particles suspended in liquids and on fluid-liquid interfaces when they are subjected to a uniform electric or magnetic field.

In Chapter 1, the rheological behavior and microstructure of electrorheological fluids formed by mixing positively and negatively polarized particles are discussed. Experimental and numerical techniques are used to show that the problem of fragmentation, which occurs when either positively or negatively polarized particles are used, is avoided by using suitable mixtures of positively and negatively polarized particles. In a uniform electric field, particles formed chain-like structures attracting their nearest neighbors. As a result, a three-dimensional connected structure is formed. The strength of inter-particle forces that guides the self-assembly process particles depends on electric field intensity, particle polarizabilities, particles' size ratio, and the number ratio. In our experiments, the microstructure modification is measured in terms of the yield stress as a function of the volume fraction of positively polarized particles for different electric field intensities. The total mass of particles was kept constant while their respective volume fractions were varied. Experimental results show that the yield stress of a mixture of positively and negatively polarizable particles was consistently greater than that of the suspensions consisting of only one type of particles, indicating an increased attraction among the particles. A range of volume fractions exists for which particles come together to form a connected pattern without fragmentation into chains and columns. Also, the yield stress increased with increasing electric field intensity. The direct numerical simulation results were in agreement with the experimental results.

In chapter 2, a similar approach is used to study the behavior of magnetorheological fluids formed using mixtures of positively polarized iron particles and negatively polarized glass particles in a ferrofluid when an external magnetic field was applied. MR fluids' rheological response depends on parameters such as the particles' concentration, magnetic susceptibilities of the suspending liquid, and the applied magnetic field intensity. The degree of formation of a connected structure was investigated in terms of the yield stress and analyzed as a function of varying volume fractions of positively polarized particles keeping the total particle volume fraction constant. Experimental results show that the yield stress increased with increased volume fractions of positively polarized particles and decreased after reaching a maximum point. This indicates that there is a specific volume fraction of particles for which a connected pattern forms. In addition, the peak value of the yield stress increased with an increase in the total particle volume fraction. We also found that the yield stress increases with increasing susceptibility and concentration of magnetic particles.

Chapter 3 discusses a technique for the self-assembly of submicron-sized gold nanoparticles on a non-conducting film's surface. This was achieved by placing particles on a UV curable liquid's surface, applying an electric field normal to the surface to conduct self-assembly, enabling control of lattice spacing, and solidifying the monolayer once a suitable arrangement was formed. The monolayers formed were used to prepare substrates for Surface-Enhanced Raman Scattering (SERS) applications. The experimental results show that the performance of the laboratory-built substrates containing varying concentrations of gold nanoparticles was better, indicating a stronger SERS effect than a commercial SERS substrate. Our substrates are $\sim$6.75 times more efficient per gold particle compared to the commercial substrates. It is also found that 46% of the substrates' surface area was covered with gold particles which is another reason for the observed enhancement.

APPENDIX A

PROPERTIES OF PARTICLES AND SUSPENDING LIQUID IN ER SUSPENSIONS

The properties of particles and suspending liquid for preparing ER fluid suspensions are shown in the table below:

Table A.1 Physical Properties of Dispersed Phases and Dispersion Medium in an ER Fluid

Material	**Density**(g/cm^3)	**Dielectric Constant**
Al_2O_3	3.97	9.8
CaP	3.14	1.6
Glass	$0.19 - 0.6$	$1.165 - 1.56$
Silicone Oil	1.27	7.1

APPENDIX B

CALCULATION OF NUMBER RATIO

The number ratio of both types of particles are calculated for two different cases of particle densities as shown below:

$$Density(\rho) = \frac{Mass(M)}{Volume(V)}$$

$$Mass_{Gl/Si} = M_1$$

$$Mass_{Al_2O_3} = M_2$$

$$M_1 = \rho_1 \times V_1$$

$$M_2 = \rho_2 \times V_2$$

$$\frac{M_1}{M_2} = \frac{\rho_1}{\rho_2} \times \frac{V_1}{V_2}$$

Case 1: When

$$\rho_1 = \rho_2$$

$$\frac{M_1}{M_2} = \frac{V_1}{V_2} = \frac{N_1}{N_2}$$

Case 2: When

$$\rho_1 \neq \rho_2$$

$$\frac{V_1}{V_2} = \frac{M_1}{M_2} \times \frac{\rho_2}{\rho_1}$$

$$\frac{V_1}{V_2} = \frac{N_1}{N_2} = \frac{M_1}{M_2} \times \frac{\rho_2}{\rho_1}$$

Number ratio=Volume ratio

$$\frac{N_1}{N_2} = \frac{V_1}{V_2}$$

$$\frac{N_1}{N_2} + 1 = \frac{V_1}{V_2} + 1 = \left(\frac{M_1}{M_2}\frac{\rho_2}{\rho_1}\right) + 1$$

$$\frac{N_1 + N_2}{N_2} = \left(\frac{M_1}{M_2}\frac{\rho_2}{\rho_1}\right) + 1 = \frac{V_1 + V_2}{V_2}$$

$$\frac{N_2}{N_1 + N_2} = \frac{V_2}{V_1 + V_2} = \frac{1}{\left(\frac{M_1}{M_2}\frac{\rho_2}{\rho_1}\right) + 1}$$

$$V = N \times \left(\frac{4}{3}\pi R^3\right)$$

$$\frac{V_1}{V_2} = \frac{N_1}{N_2}\frac{{R_1}^3}{{R_2}^3}$$

$$\frac{N_1}{N_2} = \frac{V_1}{V_2}\frac{{R_2}^3}{{R_1}^3}$$

APPENDIX C

CALCULATION OF EFFECTIVE PERMITTIVITY FOR HOLLOW PARTICLES

If a layered dielectric particle is spherically symmetric then the original particle is replaced by an equivalent homogenous sphere of the same radius. The effective permittivity of this equivalent particle, ε_2', reflects the attributes of the original particles' structure. The expression for the effective permittivity ε_2' of the equivalent particle is given by the following equation:

$$\varepsilon_2{}' = \varepsilon_2 \times \left\{ \frac{a_3 + 2(\frac{\varepsilon_3 - \varepsilon_2}{\varepsilon_3 + 2\varepsilon_2})}{a_3 - (\frac{\varepsilon_3 - \varepsilon_2}{\varepsilon_3 + 2\varepsilon_2})} \right\}$$

APPENDIX D

DATA TABLES

The data tables for the ER fluid mixtures are here under:

Table D.1 Data for an ER Fluid Containing a Mixture of Aluminum Oxide and Glass Particles

Mixtures	**Mean size of glass (μm)**	**Max. electric field intensity (kV/mm)**	**Force (g)**	**Number of Peaks**	**Yield Stress (kN/m^2)**	**Volume fractions of $Al_2O_3 : Gl$**	**Size Ratio $\frac{Mean_{Al_2O_3}}{Mean_{Gl}}$**	**Number Ratio $\frac{N_{Al_2O_3}}{N_{Gl}}$**
Al_2O_3-Gl	90	1.54	57	1	2.795	30:70	1.13	0.29
Al_2O_3-Gl	72	1.54	31, 32.8	2	1.52, 1.61	30:70, 60:40	1.42	0.15, 0.52
Al_2O_3-Gl	50	1.54	50	1	2.45	30:70	2.05	0.05
Al_2O_3-Gl	20	1.54	32.55	2	1.595, 1.75	30:70, 80:20	5.125	0.003, 0.029

Table D.2 Data for an ER Fluid Containing a Mixture of Aluminum Oxide and Calcium Phosphate Particles

Mixtures	**Mean size of CaP (μm)**	**Max. electric field intensity (kV/mm)**	**Force (g)**	**Number of Peaks**	**Yield Stress (kN/m^2)**	**Volume fractions of $Al_2O_3 : CaP$**	**Number Ratio $\frac{N_{Al_2O_3}}{N_{CaP}}$**
$Al_2O_3 - CaP$	101.5	1.54	113	1	5.5	40:60	0.65

Table D.3 Data for an ER Fluid Containing a Mixture of Aluminum Oxide and Silica Particles

Mixtures	**Mean size of CaP (μm)**	**Max. electric field intensity (kV/mm)**	**Force (g)**	**Number of Peaks**	**Yield Stress (kN/m^2)**	**Volume fractions of $Al_2O_3 : Si$**	**Number Ratio $\frac{N_{Al_2O_3}}{N_{Si}}$**
$Al_2O_3 - Si$	101	1.54	37.95	1	1.86	20:80	0.232

Table D.4 Dielectric Mismatch

Particle Name	**Mean Size (μm)**	**Effective density**	R_1, R_2	**Effective/ Complex Permittivity**	**Dielectric Mismatch**
Al_2O_3	102.5	-	-	9.8	0.1125
CaP	101.5	-	-	1.6	-0.35
Gl (solid)	-	-	-	4	-0.17
Gl (Hollow)	90	0.21	45, 43.8	1.178	-0.39
Gl (Hollow)	72	0.19	36, 35.13	1.165	-0.38
Gl (Hollow)	50	0.48	25, 23.42	1.421	-0.36
Gl (Hollow)	20	0.6	10, 9.2	1.56	-0.35
Si	100	-	-	2.5	-0.28

REFERENCES

[1] S. C. Glotzer and M. J. Solomon, "Anisotropy of building blocks and their assembly into complex structures," *Nature Materials*, vol. 6, no. 8, p. 557, 2007.

[2] B. Luo, A. Kim, J. W. Smith, Z. Ou, Z. Wu, J. Kim, and Q. Chen, "Hierarchical self-assembly of 3d lattices from polydisperse anisometric colloids," *Nature Communications*, vol. 10, no. 1, p. 1815, 2019.

[3] K. Miszta, J. de Graaf, G. Bertoni, D. Dorfs, R. Brescia, S. Marras, L. Ceseracciu, R. Cingolani, R. van Roij, M. Dijkstra, and L. Manna, "Hierarchical self-assembly of suspended branched colloidal nanocrystals into superlattice structures," *Nature Materials*, vol. 10, no. 11, p. 872, 2011.

[4] A. M. Kalsin, M. Fialkowski, M. Paszewski, S. K. Smoukov, K. J. M. Bishop, and B. A. Grzybowski, "Electrostatic self-assembly of binary nanoparticle crystals with a diamond-like lattice," *Science*, vol. 312, no. 5772, p. 420, 2006.

[5] K. Singh, A. Raghav, P. K. Jha, and S. Satapathi, "Effect of size and charge asymmetry on aggregation kinetics of oppositely charged nanoparticles," *Scientific Reports*, vol. 9, no. 3762, 2019.

[6] H. Block and J. P. Kelly, "Electro-rheology," *Journal of Physics D: Applied Physics*, vol. 21, no. 12, p. 1661, 1988.

[7] R. M. Erb, H. S. Son, B. Samanta, V. M. Rotello, and B. B. Yellen, "Magnetic assembly of colloidal superstructures with multipole symmetry," *Nature*, vol. 457, no. 7232, p. 999, 2009.

[8] A. P. Gast and C. F. Zukoski, "Electrorheological fluids as colloidal suspensions," *Advances in Colloid and Interface Science*, vol. 30, no. C, p. 153, 1989.

[9] T. C. Halsey, "Electrorheological fluids," *Science*, vol. 258, no. 5083, p. 761, 1992.

[10] K. S. Khalil, A. Sagastegui, Y. Li, M. A. Tahir, J. E. S. Socolar, B. J. Wiley, and B. B. Yellen, "Binary colloidal structures assembled through ising interactions," *Nature Communications*, vol. 3, no. 794, 2012.

[11] D. L. Klass and T. W. Martinek, "Electroviscous fluids. i. rheological properties," *Journal of Applied Physics*, vol. 38, no. 1, p. 67, 1967.

[12] S. Nöjd, P. S. Mohanty, P. Bagheri, A. Yethiraj, and P. Schurtenberger, "Electric field driven self-assembly of ionic microgels," *Soft Matter*, vol. 9, no. 38, p. 9199, 2013.

[13] M. Parthasarathy and D. J. Klingenberg, "Electrorheology: Mechanisms and models," *Materials Science and Engineering: R: Reports*, vol. 17, no. 2, p. 57, 1996.

[14] R. Tao and J. M. Sun, "Three-dimensional structure of induced electrorheological solid," *Physical Review Letters*, vol. 67, no. 3, p. 398, 1991.

[15] W. Wen, X. Huang, S. Yang, K. Lu, and P. Sheng, "The giant electrorheological effect in suspensions of nanoparticles," *Nature Materials*, vol. 2, no. 11, p. 727, 2003.

[16] A. F. Demirörs and L. Alison, "Electric field assembly of colloidal superstructures," *The Journal of Physical Chemistry Letters*, vol. 9, no. 15, p. 4437, 2018.

[17] J. E. Martin and A. Snezhko, "Driving self-assembly and emergent dynamics in colloidal suspensions by time-dependent magnetic fields," *Reports on Progress in Physics*, vol. 76, no. 12, p. 126601, 2013.

[18] R. Saldivar-Guerrero, R. Richter, I. Rehberg, N. Aksel, L. Heymann, and O. S. Rodriguez-Fernández, "Viscoelasticity of mono- and polydisperse inverse ferrofluids," *The Journal of Chemical Physics*, vol. 125, no. 8, p. 084907, 2006.

[19] A. Snezhko, M. Belkin, I. S. Aranson, and W. K. Kwok, "Self-assembled magnetic surface swimmers," *Physical Review Letters*, vol. 102, no. 11, p. 118103, 2009.

[20] W. M. Winslow, "Induced fibration of suspensions," *Journal of Applied Physics*, vol. 20, no. 12, p. 1137, 1949.

[21] A. Yethiraj, "Tunable colloids: control of colloidal phase transitions with tunable interactions," *Soft Matter*, vol. 3, no. 9, p. 1099, 2007.

[22] Y. Chen, A. F. Sprecher, and H. Conrad, "Electrostatic particle-particle interactions in electrorheological fluids," *Journal of Applied Physics*, vol. 70, no. 11, p. 6796, 1991.

[23] V. Liljeström, C. Chen, P. Dommersnes, J. O. Fossum, and A. H. Gröschel, "Active structuring of colloids through field-driven self-assembly," *Current Opinion in Colloid and Interface Science*, vol. 40, p. 25, 2019.

[24] T. Liu, X. Gong, Y. Xu, and S. Xuan, "Magneto-induced stress enhancing effect in a colloidal suspension of paramagnetic and superparamagnetic particles dispersed in a ferrofluid medium," *Soft Matter*, vol. 10, no. 6, p. 813, 2014.

[25] L. Rodríguez-Arco, M. T. López-López, A. Y. Zubarev, K. Gdula, and J. D. G. Durán, "Inverse magnetorheological fluids," *Soft Matter*, vol. 10, no. 33, p. 6256, 2014.

[26] P. Sheng and W. Wen, "Electrorheological fluids: Mechanisms, dynamics, and microfluidics applications," *Annual Review of Fluid Mechanics*, vol. 44, no. 1, p. 143, 2012.

[27] K. Raj and R. Moskowitz, "Commercial applications of ferrofluids," *Journal of Magnetism and Magnetic Materials*, vol. 85, no. 1, p. 233, 1990.

[28] B. Berkovski, V. G. Bashtovoi, and Unesco, *Magnetic fluids and applications handbook*. New York, NY; Wallingford: Begell House, Inc., 1996.

[29] A. S. Lübbe, C. Alexiou, and C. Bergemann, "Clinical applications of magnetic drug targeting," *Journal of Surgical Research*, vol. 95, no. 2, p. 200, 2001.

[30] Q. A. Pankhurst, J. Connolly, S. K. Jones, and J. Dobson, "Applications of magnetic nanoparticles in biomedicine," *Journal of Physics D: Applied Physics*, vol. 36, no. 13, p. R167, 2003.

[31] N. Wereley, A. Chaudhuri, J.-H. Yoo, S. John, S. Kotha, A. Suggs, R. Radhakrishnan, B. Love, and T. Sudarshan, "Bidisperse magnetorheological fluids using fe particles at nanometer and micron scale," *Journal of Intelligent Material Systems and Structures*, vol. 17, no. 5, p. 392, 2006.

[32] D. Susan-Resiga and L. Vékás, "Yield stress and flow behavior of concentrated ferrofluid-based magnetorheological fluids: the influence of composition," *Rheologica Acta*, vol. 53, p. 645, 2014.

[33] M. T. López-López, J. de Vicente, G. Bossis, F. González-Caballero, and J. D. G. Durán, "Preparation of stable magnetorheological fluids based on extremely bimodal iron–magnetite suspensions," *Journal of Materials Research*, vol. 20, no. 4, p. 874, 2005.

[34] P. A. Cox and R. B. Knox, "Two-dimensional pollination in hydrophilous plants: Convergent evolution in the genera halodule (cymodoceaceae), halophila (hydrocharitaceae), ruppia (ruppiaceae), and lepilaena (zannichelliaceae)," *American Journal of Botany*, vol. 76, no. 2, p. 164, 1989.

[35] P. Singh and D. D. Joseph, "Fluid dynamics of floating particles," *Journal of Fluid Mechanics*, vol. 530, p. 31, 2005.

[36] P. Singh, D. D. Joseph, and N. Aubry, "Dispersion and attraction of particles floating on fluid–liquid surfaces," *Soft Matter*, vol. 6, p. 4310, 2010.

[37] P. Singh, D. D. Joseph, S. K. Gurupatham, B. Dalal, and S. Nudurupati, "Spontaneous dispersion of particles on liquid surfaces," *Proceedings of the National Academy of Sciences of the United States of America*, vol. 106, p. 19761, November 2009.

[38] S. Nudurupati, M. Janjua, P. Singh, and N. Aubry, "Effect of parameters on redistribution and removal of particles from drop surfaces," *Soft Matter*, vol. 6, p. 1157, 2010.

[39] N. Aubry, P. Singh, M. Janjua, and S. Nudurupati, "Micro- and nanoparticles self-assembly for virtually defect-free, adjustable monolayers," *Proceedings of the National Academy of Sciences*, vol. 105, no. 10, p. 3711, 2008.

[40] B. Sharma, R. R. Frontiera, A.-I. Henry, E. Ringe, and R. P. Van Duyne, "Sers: Materials, applications, and the future," *Materials Today*, vol. 15, no. 1, p. 16, 2012.

[41] T. B. Jones, *Electromechanics of Particles*. Cambridge, New York, NY: Cambridge University Press, 1995.

[42] H. Fröhlich, *Theory of dielectrics; dielectric constant and dielectric loss*. Oxford, Oxfordshire: Clarendon Press, 1958.

[43] N. Bowden, J. Tien, W. T. S. Huck, and G. M. Whitesides, "Mesoscale self-assembly: the assembly of micron-and millimeter-sized objects using capillary forces," in *Supramolecular Organization and Materials Design* (C. N. R. Rao and W. Jones, eds.), p. 103, Cambridge, GBR: Cambridge University Press, 2001.

[44] P. Singh and D. Joseph, "Fluid dynamics of floating particles," *Journal of Fluid Mechanics*, vol. 530, p. 31, 2005.

[45] S. C. Glotzer and M. J. Solomon, "Anisotropy of building blocks and their assembly into complex structures," *Nature Materials*, vol. 6, no. 8, p. 557, 2007.

[46] B. Luo, A. Kim, J. W. Smith, Z. Ou, Z. Wu, J. Kim, and Q. Chen, "Hierarchical self-assembly of 3d lattices from polydisperse anisometric colloids," *Nature Communications*, vol. 10, no. 1, p. 1815, 2019.

[47] K. Miszta, J. de Graaf, G. Bertoni, D. Dorfs, R. Brescia, S. Marras, L. Ceseracciu, R. Cingolani, R. van Roij, M. Dijkstra, and L. Manna, "Hierarchical self-assembly of suspended branched colloidal nanocrystals into superlattice structures," *Nature Materials*, vol. 10, no. 11, p. 872, 2011.

[48] A. M. Kalsin, M. Fialkowski, M. Paszewski, S. K. Smoukov, K. J. M. Bishop, and B. A. Grzybowski, "Electrostatic self-assembly of binary nanoparticle crystals with a diamond-like lattice," *Science*, vol. 312, no. 5772, p. 420, 2006.

[49] K. Singh, A. Raghav, P. K. Jha, and S. Satapathi, "Effect of size and charge asymmetry on aggregation kinetics of oppositely charged nanoparticles," *Scientific Reports*, vol. 9, no. 1, p. 3762, 2019.

[50] S. Nöjd, P. S. Mohanty, P. Bagheri, A. Yethiraj, and P. Schurtenberger, "Electric field driven self-assembly of ionic microgels," *Soft Matter*, vol. 9, no. 38, p. 9199, 2013.

[51] R. Tao and J. M. Sun, "Three-dimensional structure of induced electrorheological solid," *Physical Review Letters*, vol. 67, no. 3, p. 398, 1991.

[52] H. Block and J. P. Kelly, "Electro-rheology," *Journal of Physics D: Applied Physics*, vol. 21, no. 12, p. 1661, 1988.

[53] A. P. Gast and C. F. Zukoski, "Electrorheological fluids as colloidal suspensions," *Advances in Colloid and Interface Science*, vol. 30, no. C, p. 153, 1989.

[54] T. C. Halsey, "Electrorheological fluids," *Science*, vol. 258, no. 5083, p. 761, 1992.

[55] D. L. Klass and T. W. Martinek, "Electroviscous fluids. i. rheological properties," *Journal of Applied Physics*, vol. 38, no. 1, p. 67, 1967.

[56] M. Parthasarathy and D. J. Klingenberg, "Electrorheology: Mechanisms and models," *Materials Science and Engineering: R: Reports*, vol. 17, no. 2, p. 57, 1996.

[57] W. Wen, X. Huang, S. Yang, K. Lu, and P. Sheng, "The giant electrorheological effect in suspensions of nanoparticles," *Nature Materials*, vol. 2, no. 11, p. 727, 2003.

[58] J. E. Martin and A. Snezhko, "Driving self-assembly and emergent dynamics in colloidal suspensions by time-dependent magnetic fields," *Reports on Progress in Physics*, vol. 76, no. 12, p. 126601, 2013.

[59] A. Snezhko, M. Belkin, I. S. Aranson, and W. K. Kwok, "Self-assembled magnetic surface swimmers," *Physical Review Letters*, vol. 102, no. 11, p. 118103, 2009.

[60] W. M. Winslow, "Induced fibration of suspensions," *Journal of Applied Physics*, vol. 20, no. 12, p. 1137, 1949.

[61] R. Saldivar-Guerrero, R. Richter, I. Rehberg, N. Aksel, L. Heymann, and O. S. Rodriguez-Fernández, "Viscoelasticity of mono- and polydisperse inverse ferrofluids," *The Journal of Chemical Physics*, vol. 125, no. 8, p. 084907, 2006.

[62] A. F. Demirörs and L. Alison, "Electric field assembly of colloidal superstructures," *The Journal of Physical Chemistry Letters*, vol. 9, no. 15, p. 4437, 2018.

[63] T. Liu, X. Gong, Y. Xu, and S. Xuan, "Magneto-induced stress enhancing effect in a colloidal suspension of paramagnetic and superparamagnetic particles dispersed in a ferrofluid medium," *Soft Matter*, vol. 10, no. 6, p. 813, 2014.

[64] L. Rodríguez-Arco, M. T. López-López, A. Y. Zubarev, K. Gdula, and J. D. G. Durán, "Inverse magnetorheological fluids," *Soft Matter*, vol. 10, no. 33, p. 6256, 2014.

[65] P. Sheng and W. Wen, "Electrorheological fluids: Mechanisms, dynamics, and microfluidics applications," *Annual Review of Fluid Mechanics*, vol. 44, no. 1, p. 143, 2012.

[66] Y. Chen, A. F. Sprecher, and H. Conrad, "Electrostatic particle-particle interactions in electrorheological fluids," *Journal of Applied Physics*, vol. 70, no. 11, p. 6796, 1991.

[67] R. M. Erb, H. S. Son, B. Samanta, V. M. Rotello, and B. B. Yellen, "Magnetic assembly of colloidal superstructures with multipole symmetry," *Nature*, vol. 457, no. 7232, p. 999, 2009.

[68] K. S. Khalil, A. Sagastegui, Y. Li, M. A. Tahir, J. E. S. Socolar, B. J. Wiley, and B. B. Yellen, "Binary colloidal structures assembled through ising interactions," *Nature Communications*, vol. 3, no. 794, 2012.

[69] A. Yethiraj, "Tunable colloids: control of colloidal phase transitions with tunable interactions," *Soft Matter*, vol. 3, no. 9, p. 1099, 2007.

[70] E. V. Shevchenko, D. V. Talapin, N. A. Kotov, S. O'Brien, and C. B. Murray, "Structural diversity in binary nanoparticle superlattices," *Nature*, vol. 439, no. 7072, p. 55, 2006.

[71] P. Singh, M. S. Hossain, S. k. Gurupatham, K. Shah, E. Amah, D. Ju, M. Janjua, S. Nudurupati, and I. Fischer, "Molecular-like hierarchical self-assembly of monolayers of mixtures of particles," *Scientific reports*, vol. 4, p. 7427, 2014.

[72] Y. Fu, J. Yao, H. Zhao, G. Zhao, and Y. Qiu, "Simulation of a bidisperse magnetorheological fluid using the combination of a two-component lattice boltzmann method and a discrete element approach," *Soft Matter*, vol. 15, no. 34, p. 6867, 2019.

[73] J. Kadaksham, P. Singh, and N. Aubry, "Dielectrophoresis induced clustering regimes of viable yeast cells," *Electrophoresis*, vol. 26, no. 19, p. 3738, 2005.

[74] D. J. Klingenberg, F. v. Swol, and C. F. Zukoski, "Dynamic simulation of electrorheological suspensions," *The Journal of Chemical Physics*, vol. 91, no. 12, p. 7888, 1989.

[75] A. T. J. Kadaksham, P. Singh, and N. Aubry, "Dielectrophoresis of nanoparticles," *Electrophoresis*, vol. 25, no. 21-22, p. 3625, 2004.

[76] M. Chen, H.-Y. Ko, R. C. Remsing, M. F. C. Andrade, B. Santra, Z. Sun, A. Selloni, R. Car, M. L. Klein, J. P. Perdew, and X. Wu, "Ab initio theory and modeling of water," *Proceedings of the National Academy of Sciences of the United States of America*, vol. 114, no. 41, p. 10846, 2017.

[77] J. Kadaksham, P. Singh, and N. Aubry, "Dynamics of electrorheological suspensions subjected to spatially nonuniform electric fields," *Journal of Fluids Engineering*, vol. 126, no. 2, p. 170, 2004.

[78] J. Kadaksham, P. Singh, and N. Aubry, "Manipulation of particles using dielectrophoresis," *Mechanics Research Communications*, vol. 33, no. 1, p. 108, 2006.

[79] T. B. Jones, *Electromechanics of Particles*. Cambridge, New York, NY: Cambridge University Press, 1995.

[80] A. T. J. Kadaksham, P. Singh, and N. Aubry, "Dielectrophoresis of nanoparticles," *Electrophoresis*, vol. 25, no. 21-22, p. 3625, 2004.

[81] S. G.Bossis, O.Volkova and A.Meunier, *Ferrofluids: Magnetically Controllable Fluids and Their Applications*. Springer, 2002.

[82] G. Bossis, P. Khuzir, S. Lacis, and O. Volkova, "Yield behavior of magnetorheological suspensions," *Journal of Magnetism and Magnetic Materials*, vol. 258-259, p. 456, 2003.

[83] M. Shliomis, "Effective viscosity of magnetic suspensions," *The Journal of Experimental and Theoretical Physics*, vol. 34, no. 6, p. 1291, 1972.

[84] S. Odenbach and S. Thurm, *Magnetoviscous Effects in Ferrofluids*, p. 185. Berlin, Heidelberg: Springer Berlin Heidelberg, 2002.

[85] F. R. Cunha, A. P. Rosa, and N. J. Dias, "Rheology of a very dilute magnetic suspension with micro-structures of nanoparticles," *Journal of Magnetism and Magnetic Materials*, vol. 397, p. 266, 2016.

[86] D. Borin, A. Zubarev, D. Chirikov, R. Müller, and S. Odenbach, "Ferrofluid with clustered iron nanoparticles: Slow relaxation of rheological properties under joint action of shear flow and magnetic field," *Journal of Magnetism and Magnetic Materials*, vol. 323, no. 10, p. 1273, 2011.

[87] H. Shahnazian, D. Gräf, D. Y. Borin, and S. Odenbach, "Rheology of a ferrofluid based on nanodisc cobalt particles," *Journal of Physics D: Applied Physics*, vol. 42, no. 20, p. 205004, 2009.

[88] R. Gu, X. Gong, W. Jiang, L. Hao, S. Xuan, and Z. Zhang, "Synthesis and rheological investigation of a magnetic fluid using olivary silica-coated iron particles as a precursor," *Journal of Magnetism and Magnetic Materials*, vol. 320, no. 21, p. 2788, 2008.

[89] A. Ray and T. M. Fischer, "Magnetic field controlled composite paramagnetic–diamagnetic colloidal phases," *The Journal of Physical Chemistry B*, vol. 116, no. 28, p. 8233, 2012.

[90] L. Rodríguez-Arco, M. T. López-López, A. Y. Zubarev, K. Gdula, and J. D. G. Durán, "Inverse magnetorheological fluids," *Soft Matter*, vol. 10, no. 33, p. 6256, 2014.

[91] D. Susan-Resiga and L. Vekas, "Ferrofluid-based magnetorheological fluids: tuning the properties by varying the composition at two hierarchical levels," *Rheologica Acta*, vol. 55, no. 7, p. 581, 2016.

[92] M. T. López-López, J. de Vicente, G. Bossis, F. González-Caballero, and J. D. G. Durán, "Preparation of stable magnetorheological fluids based on extremely bimodal iron–magnetite suspensions," *Journal of Materials Research*, vol. 20, no. 4, p. 874, 2005.

[93] V. Liljeström, C. Chen, P. Dommersnes, J. O. Fossum, and A. H. Gröschel, "Active structuring of colloids through field-driven self-assembly," *Current Opinion in Colloid and Interface Science*, vol. 40, p. 25, 2019.

[94] S. Nudurupati, M. Janjua, P. Singh, and N. Aubry, "Effect of parameters on redistribution and removal of particles from drop surfaces," *Soft Matter*, vol. 6, no. 6, p. 1157, 2010.

[95] P. A. Cox and R. B. Knox, "Two-dimensional pollination in hydrophilous plants: Convergent evolution in the genera halodule (cymodoceaceae), halophila (hydrocharitaceae), ruppia (ruppiaceae), and lepilaena (zannichelliaceae)," *American Journal of Botany*, vol. 76, no. 2, p. 164, 1989.

[96] P. Singh, D. D. Joseph, S. K. Gurupatham, B. Dalal, and S. Nudurupati, "Spontaneous dispersion of particles on liquid surfaces," *Proceedings of the National Academy of Sciences*, vol. 106, no. 47, p. 19761, 2009.

[97] B. Sharma, R. R. Frontiera, A.-I. Henry, E. Ringe, and R. P. Van Duyne, "Sers: Materials, applications, and the future," *Materials Today*, vol. 15, no. 1, p. 16, 2012.

[98] W. E. Doering and S. Nie, "Single-molecule and single-nanoparticle sers:examining the roles of surface active sites and chemical enhancement," *The Journal of Physical Chemistry B*, vol. 106, no. 2, p. 311, 2002.

[99] P. G. Etchegoin and E. C. Le Ru, "A perspective on single molecule sers: current status and future challenges," *Physical Chemistry Chemical Physics*, vol. 10, no. 40, p. 6079, 2008.

[100] J. B. Jackson, N. J. Halas, and L. K. James, "Surface-enhanced raman scattering on tunable plasmonic nanoparticle substrates," *Proceedings of the National Academy of Sciences of the United States of America*, vol. 101, no. 52, p. 17930, 2004.

[101] S. Bhaskar, F. Tian, T. Stoeger, W. Kreyling, J. M. de la Fuente, V. Grazú, P. Borm, G. Estrada, V. Ntziachristos, and D. Razansky, "Multifunctional nanocarriers for diagnostics, drug delivery and targeted treatment across blood-brain barrier: perspectives on tracking and neuroimaging," *Particle and Fibre Toxicology*, vol. 7, no. 1, p. 3, 2010.

[102] C. Bao, N. Beziere, P. del Pino, B. Pelaz, G. Estrada, F. Tian, V. Ntziachristos, J. M. de la Fuente, and D. Cui, "Gold nanoprisms as optoacoustic signal nanoamplifiers for in vivo bioimaging of gastrointestinal cancers," *Small*, vol. 9, no. 1, p. 68, 2013.

[103] P. L. Stiles, J. A. Dieringer, N. C. Shah, and R. P. V. Duyne, "Surface-enhanced raman spectroscopy," *Annual Review of Analytical Chemistry*, vol. 1, no. 1, p. 601, 2008.

[104] J. P. Camden, J. A. Dieringer, Y. Wang, D. J. Masiello, L. D. Marks, G. C. Schatz, and R. P. Van Duyne, "Probing the structure of single-molecule surface-enhanced raman scattering hot spots," *Journal of the American Chemical Society*, vol. 130, no. 38, p. 12616, 2008.

[105] L. Jensen, C. M. Aikens, and G. C. Schatz, "Electronic structure methods for studying surface-enhanced raman scattering," *Chemical Society Reviews*, vol. 37, no. 5, p. 1061, 2008.

[106] A. D. McFarland, M. A. Young, J. A. Dieringer, and R. P. Van Duyne, "Wavelength-scanned surface-enhanced raman excitation spectroscopy," *The Journal of Physical Chemistry B*, vol. 109, no. 22, p. 11279, 2005.

[107] M. Moskovits, "Persistent misconceptions regarding sers," *Physical Chemistry Chemical Physics*, vol. 15, no. 15, p. 5301, 2013.

[108] P. K. Aravind and H. Metiu, "The enhancement of raman and fluorescent intensity by small surface roughness. changes in dipole emission," *Chemical Physics Letters*, vol. 74, no. 2, p. 301, 1980.

[109] K. Kneipp, H. Kneipp, I. Itzkan, R. R. Dasari, and M. S. Feld, "Surface-enhanced raman scattering and biophysics," *Journal of Physics: Condensed Matter*, vol. 14, no. 18, p. R597, 2002.

[110] C. S. Seney, B. M. Gutzman, and R. H. Goddard, "Correlation of size and surface-enhanced raman scattering activity of optical and spectroscopic properties for silver nanoparticles," *The Journal of Physical Chemistry C*, vol. 113, no. 1, p. 74, 2009.

[111] K. G. Stamplecoskie, J. C. Scaiano, V. S. Tiwari, and H. Anis, "Optimal size of silver nanoparticles for surface-enhanced raman spectroscopy," *The Journal of Physical Chemistry C*, vol. 115, no. 5, p. 1403, 2011.

[112] V. S. Tiwari, T. Oleg, G. K. Darbha, W. Hardy, J. P. Singh, and P. C. Ray, "Non-resonance sers effects of silver colloids with different shapes," *Chemical Physics Letters*, vol. 446, no. 1, p. 77, 2007.

[113] F. Tian, F. Bonnier, A. Casey, A. E. Shanahan, and H. J. Byrne, "Surface enhanced raman scattering with gold nanoparticles: effect of particle shape," *Analytical Methods*, vol. 6, no. 22, p. 9116, 2014.

[114] X. Liu, L. Zhao, H. Shen, H. Xu, and L. Lu, "Ordered gold nanoparticle arrays as surface-enhanced raman spectroscopy substrates for label-free detection of nitroexplosives," *Talanta*, vol. 83, no. 3, p. 1023, 2011.

[115] A. R. Tao, D. P. Ceperley, P. Sinsermsuksakul, A. R. Neureuther, and P. Yang, "Self-organized silver nanoparticles for three-dimensional plasmonic crystals," *Nano Letters*, vol. 8, no. 11, p. 4033, 2008.